Barium isotope cycling in the marine environment: Pathways of fractionation and implications for paleoceanographic applications

by

Julien Thomas Middleton
B.A, Colby College (2015)

Submitted to the Department of Earth, Atmospheric, and Planetary Sciences in partial fulfillment of the requirements for the degree of
Doctor of Philosophy
at the
MASSACHUSETTS INSTITUTE OF TECHNOLOGY
and the
WOODS HOLE OCEANOGRAPHIC INSTITUTION

May 2022

Author.....
Joint Program in Oceanography/Applied Ocean Science & Engineering Massachusetts Institute of Technology & Woods Hole Oceanographic Institution April 25, 2022

Certified by.....
Dr. Tristan J. Horner
Associate Scientist in Marine Chemistry & Geochemistry
Woods Hole Oceanographic Institution
Thesis Supervisor

Accepted by.....
Dr. Colleen Hansel
Senior Scientist in Marine Chemistry & Geochemistry
Woods Hole Oceanographic Institution
Chair, Joint Committee for Chemical Oceanography

Barium isotope cycling in the marine environment: Pathways of fractionation and implications for paleoceanographic applications

by

Julien Thomas Middleton

Submitted to the Department of Earth, Atmospheric, and Planetary Sciences on April 25, 2022, in Partial Fulfillment of the Requirements for the degree of Doctor of Philosophy in Chemical Oceanography.

Abstract

Removal of particulate organic carbon (POC) from sunlit surface waters into the deep ocean represents a climatically important sink of atmospheric carbon dioxide (CO_2), linking the biogeochemical cycling of POC to CO_2-driven climate change. As POC is not well preserved in the sediment record, other proxies, including the chemistry of barium (Ba) in the ocean and through the sedimentary record, offer an avenue to investigate oceanic carbon export through Earth's history. This thesis seeks to constrain the controls on the formation, cycling, and isotopic signature of the main particulate phase of marine barium, the mineral barite ($BaSO_4$) through its inception in the water column, during deposition, and ultimately into the rock record. To that end, I characterize the depth, spatial region, and general controls on particulate Ba formation in the South Pacific Ocean through shipboard experimentation and find that particulate Ba forms mainly in the surface of the Polar Frontal Zone in the presence of large particles and microbial activity. Next, I characterize the effect of ion exchange on $BaSO_4$, a process previously unstudied under marine conditions, in a laboratory setting. Ion exchange occurs rapidly between dissolved Ba and $BaSO_4$ and imparts a characteristic net offset between the Ba isotope composition of the dissolved and solid phase, which arises through a combination of Ba isotope fractionation during both precipitation and dissolution. Finally, I investigate the role of ion exchange in marine settings using co-located pore fluids and sedimented $BaSO_4$. Modeling constrained by data from natural samples produce results that are consistent with the laboratory study, suggesting that this mode of isotopic fractionation impacts Ba isotopes in the environment and must be accounted for when applying Ba based climate proxies.

Thesis Supervisor: Dr. Tristan J. Horner
Title: Associate Scientist (Woods Hole Oceanographic Institution)

Acknowledgements

First, thanks must be given to my lab and the members of the WHOI ICP Facility, without whom I could not have carried out this work. Thanks to Dr. Tristan Horner for taking me on in my second year, when I realized that this isotope stuff was much more interesting than I'd first thought. To Logan Tegler and Maureen Auro: you'll forever be my favorite clean lab partners, I can't imagine hours of columns without all the fun and ridiculousness we shared in lab. Thanks to Sune Nielsen and Ann Dunlea for their mentorship and support throughout the years, and to Peter Crockford for his herculean support reading endless drafts in my final year. To Gretchen Swarr thank you for teaching me so much about mass specs, and to Jurek Blusztajn, thank you for teaching me to work through every hiccup the Neptune threw my way. There is no science without my collaborators, and I'm forever grateful for the support of so many.

There is no world in which I finished this thesis without the support, kindness, and love of my community in Woods Hole. My time in the Joint Program has been highlighted by getting to build friendships with some of the best and brightest folks I've ever had the good fortune to meet, and I can't imagine going through graduate school without them. Thanks to Mallory Ringham, Sheron Luk, Jen Karolewski, Becca Chmiel, Riss Kellogg, Caitlyn Kelleher, Danny Lowenstein, Emmanuel Codillo, Guiliana Viglione, Rachel Housego, Danielle Freeman, Chloe Smith, Rose Palermo, Ben Granzow, Peter Crockford, Net Chareonpong, and Gabriela Farfan. Special thanks to everyone in the GLOW community for creating such a lovely atmosphere for queer scientists to connect and to everyone on the Committee for Diversity, Equity, and Inclusion for fighting the good fight.

Thanks to my family for being endlessly interested and supportive of my work, even as it has verged into the esoteric. It's a delight to share photos from adventures at sea and be met with genuine interest in what I was up to out there!

Finally, to Lydia and Logan: You have been a source of such love and support and I'm so grateful to know you and get to carry on in life with you! What a joy to find some of my best friends while slogging through the endless hours of classes, data collection, writing, re-writing, and *re*-writing, and to experience the lovely transition of lab mates and colleagues into dear friends. I look forward to our future adventures!

Financial Support

Funding for this work was provided by the National Science Foundation (OCE-2023456 & OCE-1827401), the Woods Hole Oceanographic Institution Ocean Ventures Fund, a National Science Foundation Graduate Research Fellowship (2017250048), and Woods Hole Oceanographic Institution.

TABLE OF CONTENTS

LIST OF FIGURES AND TABLES

Chapter 1

Chapter 2

Chapter 3

Chapter 4

Chapter 1: Introduction

Primary production in the sunlit surface waters of the ocean drives sequestration of carbon dioxide (CO_2) through the production and subsequent sinking of particulate organic carbon (POC). The export of POC out of the surface ocean represents a climactically important sink of carbon dioxide (Buesseler et al., 2007), linking the biogeochemical cycling of POC with CO_2-driven climate change on timescales of hundreds to thousands of years (Falkowski et al., 1998; Sabine et al., 2004; Sigman et al., 2010). As I show throughout this thesis, the abundance and isotopic chemistry of barium (Ba) in seawater, suspended particles, and sediments are intimately connected to these cycles. Indeed, Ba is widely used as a paleoproxy for export production based on two noteworthy correlations. First, the concentration of dissolved Ba ([Ba]) is positively linearly correlated with that of silica ([Si]; Fig. 1a). This correlation connects the otherwise biochemically inactive Ba cycle to the major nutrients required for marine life (Church and Wolgemuth, 1972; Chan et al., 1977). Second, the accumulation rate of particulate Ba in marine sediments, principally as the mineral barite ($BaSO_4$; barium sulfate), is also positively linearly correlated to flux of carbon out of the euphotic zone (i.e. carbon export; Eagle et al., 2003; Paytan and Griffith, 2007; Yao et al., 2021; Fig. 1b). This correlation connects the particulate Ba cycle to that of POC across vast swathes of Earth's oceans. These proxy applications offer detailed insight into processes critical to the regulation of the climate. However, there remain several open questions as to controls on the formation of $BaSO_4$ in the upper water column, the reactivity of $BaSO_4$ (i.e., mineral–fluid exchange), and the role of post-depositional processes on the fidelity of certain records encoded in sedimented $BaSO_4$. Additional constraints on each area are needed to fully take advantage of Ba-based paleoproxies.

In this thesis, I leverage recent developments in Ba isotope geochemistry to: describe controls on the formation and spatial distribution of $BaSO_4$ in the water column; constrain post-depositional processes affecting Ba-based paleoproxies; and, elucidate the conditions under which these proxies offer unaltered records of climatically relevant processes. Application of Ba isotopes represents a new and burgeoning sub-field of marine geochemistry, made possible by recent analytical developments (e.g., Horner et al., 2015; von Allmen et al., 2010).

1.1 The modern marine barium cycle

Dissolved barium in the oceanic water column has a nutrient-like distribution with depletion in the sunlit surface and enrichment at depth with Pacific deep water having higher concentrations than Atlantic deep water (Monnin et al., 1999). The mineral $BaSO_4$ represents the main carrier phase of particulate barium (pBa) in the water column settings, with $BaSO_4$ comprising upwards of 90 % of total suspended pBa (Jacquet et al., 2008, 2011). Barite is ubiquitous in the world's oceans and marine sediments (Yao et al., 2021) and the cycling of $BaSO_4$ in the water column, overlaid with global circulation dynamics, accounts for the large-scale features of the global distribution of d[Ba] (Horner et al., 2015; Bates et al., 2017; Horner and Crockford, 2021). The omnipresence of $BaSO_4$ is paradoxical, as vast swathes of the world's ocean are undersaturated with respect to the mineral, particularly the upper 1,000 m, where most pelagic $BaSO_4$ is thought to form (Monnin et al., 1999; Rushdi et al., 2000; Monnin and Cividini, 2006). Moreover, the occurrence of organisms known to actively precipitate $BaSO_4$ are too sparse to account for the observed distribution of Ba (Esser and Volpe, 2002). The most widely recognized solution to the barite paradox was first proposed by Chow and Goldberg (1960): the microenvironment model of $BaSO_4$ formation. Under this schema, an accumulation mechanism pre-concentrates dissolved Ba into microenvironments encapsulated within sinking particulate organic matter, thereby achieving $BaSO_4$ supersaturation and allowing mineral formation. Barite formed by this mechanism, and therefore associated with carbon export, is referred to as pelagic $BaSO_4$ (Horner et al., 2021). A number of accumulation mechanisms for Ba in microenvironments have been suggested, including the input of labile Ba during the heterotrophic oxidation of sinking organic matter (Chow and Goldberg, 1960), complexation of Ba by microbially produced extra polymeric substances (Deng et al., 2019; Martinez-Ruiz et al., 2020; 2019), and direct biomineralization of $BaSO_4$ by bacteria (Gonzalez-Muñoz et al., 2012). No consensus on the relative contributions of these processes in the environment has been reached. The microenvironment model is compatible with observed correlations between the peak in p[Ba] and particulate organic matter regeneration in the upper mesopelagic zone, as suggested by the concurrence of the p[Ba] maxima and the oxygen minimum (Sternberg et al., 2008). Despite this correlation, the depth of pelagic $BaSO_4$ formation is not well defined with evidence for formation in the upper 500 m (Chow and Goldberg, 1960; Dehairs et al., 1980, 1991, 1992; Legeleux and

Reyss, 1996) and formation throughout the mesopelagic zone as deep as 2000 m (Collier and Edmond, 1984; Dymond et al., 1992; McManus et al., 2002; van Beek et al., 2007, 2009). The expansion of our understanding of the controls on and depth of pelagic $BaSO_4$ formation can aid in accurately interpreting pelagic Ba accumulation rates in marine sediments (BaAR), thereby improving the accuracy of carbon export reconstructions. In this thesis, I present experimental data focused on constraining the controls on pBa formation, the depths at which pBa forms, and latitudinal trends in Ba uptake into the particulate phase.

1.2 Diagenesis and marine $BaSO_4$

Regardless of the controls on formation, the export of pelagic $BaSO_4$ does not depend on phytoplankton ecology (e.g., Ganeshram et al., 2003; Jacquet et al., 2007) and is instead related to integrated carbon export out of the euphotic zone (Eagle et al., 2003). This has led to the use of BaAR in marine sediments as a proxy for past export production and other changes to biogeochemical cycling (Dymond et al., 1992; Paytan and Kastner, 1996; Eagle et al., 2003; Paytan and Griffith, 2007). BaAR is an appealing proxy, as $BaSO_4$ preservation in oxic deep-sea sediments generally exceeds that of other commonly used indicators of productivity (e.g., POC, biogenic Si; Dehairs et al., 1980; Paytan and Kastner, 1996). That said, careful site selection is necessary to identify study sites which avoid other sources of $BaSO_4$, including hydrothermal, cold-seep, lithogenic, and diagenetic inputs. The first three of these are largely circumvented by choosing sites far from hydrothermal vents, cold seeps, and continental margins (Yao et al., 2021). Diagenetic $BaSO_4$, which forms in pore fluids beneath the sediment water interface, typically occurs in sediment columns which reach sulfidic conditions. Under such conditions, $BaSO_4$ dissolves and the newly dissolved Ba diffuses through the pore fluids, eventually reaching a sulfate-replete front and re-precipitating (Torres et al., 1996a, 1996b; Paytan and Griffith, 2007). Such diagenesis is well studied (Rutsch et al., 1995; Paytan and Kastner, 1996; Dean et al., 1997; Nürnberg et al., 1997; McManus et al., 1998; Gingele et al., 1999), locations with low pore fluid sulfate can be avoided, and morphological criteria exist to screen samples for diagenetic $BaSO_4$ type (e.g. Griffith and Paytan, 2012; Paytan et al., 1993).

Although $BaSO_4$ diagenesis under conditions of low sulfate is relatively well studied, far less attention has been given to studying chemical alteration of $BaSO_4$ under oxic, sulfate-replete

conditions. Alteration under these conditions may occur without visible changes to the crystal morphology (Klinkenberg et al., 2014; Gorski and Fantle, 2017), leaving the typically elliptical or euhedral pelagic $BaSO_4$ crystals visually unaltered (Fig. 2). In these cases, alteration occurs through surface-mediated processes which allow ions to exchange between the mineral and a surrounding fluid without affecting the morphology of the mineral (Bosbach et al., 2010; Curti et al., 2010; Vinograd et al., 2013; Torapava et al., 2014; Klinkenberg et al., 2014; Brandt et al., 2015). Such alteration is not observable through morphological changes to $BaSO_4$ crystals, nor through observation of d[Ba] fluxes, as ions enter and depart from the mineral surface in equal-and-opposite magnitudes. Ion exchange is known to alter the composition of calcium isotopes in carbonates (Fantle and DePaolo, 2007; Chanda et al., 2019; Oelkers et al., 2019), calcium isotopes in gypsum (Harouaka et al., 2019), potassium isotopes in a variety of potassium-salts (Li et al., 2017), magnesium isotopes in magnesite and hydromagnesite (Pearce et al., 2012; Oelkers et al., 2018), and Ba isotopes in witherite and gypsum (Mavromatis et al., 2016; Böttcher et al., 2018). These mineral phases are susceptible to post-depositional alteration, as isotopic signatures in the mineral evolve towards isotopic equilibrium with a surrounding fluid. While ion exchange has been described for the Ba(II)–$BaSO_4$ system under non-marine conditions, few constraints exist as to the impact of this process on the isotope composition of Ba in $BaSO_4$ in the marine sedimentary record.

1.3 A new dimension of analysis: barium isotopes

Barium isotopes offer a means to constrain the aforementioned issues by clarifying the source of $BaSO_4$ to the sediment and revealing post-depositional processes, such as ion exchange, and their effect on the chemistry of sedimented $BaSO_4$ (Griffith et al., 2018). To use Ba isotopes in this manner, thorough definition of isotopically fractionating processes is needed. The first measurement of the Ba isotope system in the oceans in 2015 revealed systematic relationships between [Ba] and Ba isotopes (Fig. 3; Chapter 2). Variations in Ba isotopes are conventionally reported as deviations in the $^{138}Ba/^{134}Ba$ ratio in a sample relative to a standard (NIST SRM 3104a):

$$\delta^{138}Ba = [(^{138}Ba/^{134}Ba)_{sample} /(^{138}Ba/^{134}Ba)_{NIST\ SRM\ 3104a} - 1], \quad (1)$$

expressed in ‰ (per mille). Profiles of these properties in seawater show an inverse correlation between $\delta^{138}Ba$ and [Ba], with the isotopically "heavy" Ba remaining in the dissolved phase while the isotopically "light" Ba is preferentially removed to pelagic $BaSO_4$ (Horner et al., 2015; Hsieh and Henderson, 2017). Dissolution of sinking pelagic $BaSO_4$ leads to the release of light isotopes back to the dissolved phase and imparts the characteristic increase in [Ba] and concurrent decrease in $\delta^{138}Ba$ at depth. The magnitude of the resultant difference between the dissolved and particulate phase is notated as

$$\Delta^{138}Ba_{barite-dBa} = \delta^{138}BaSO_4 - \delta^{138}Ba_{dissolved}. \quad (2)$$

Where $\delta^{138}BaSO_4$ refers to the isotopic composition of Ba in $BaSO_4$. This definition of $\Delta^{138}Ba_{barite-dBa}$ can be used to estimate $\alpha_{barite-dBa}$, where

$$\alpha_{barite-dBa} = {}^{138/134}BaSO_4/{}^{138/134}Ba_{dissolved} \quad (3)$$

through the approximation

$$\Delta^{138}Ba_{barite-dBa} \approx 1000 \times \ln(\alpha_{barite-dBa}). \quad (4)$$

when $\alpha_{barite-dBa}$ is near 1. As Ba is a heavy element—the derivation of the element name from the Greek *barys* meaning 'heavy'—the magnitude of this value is generally close to one and the approximation is valid. As in other isotope systems, these values, interchangeably referred to as the fractionation factor or the magnitude of fractionation, are characteristic of processes impacting Ba. As with BaAR, $\delta^{138}BaSO_4$ itself has been suggested as a paleoproxy for carbon export, as the formation of pelagic $BaSO_4$ in the upper mesopelagic zone is strongly tied to sinking particulate organic matter and imparts a characteristic magnitude of isotopic fractionation (i.e. the degree of preferential incorporation of certain isotopes based on their relative masses; Bridgestock et al., 2019). Therefore, changes in $\delta^{138}BaSO_4$ in the sediments give insight into the productivity of the biological pump throughout Earth history (Bridgestock et al., 2019). In a system with rigorously defined fractionation factors for all processes, $\delta^{138}Ba$ may be interpreted as a cumulative signature of those processes and their relative contributions could be quantified. Naturally, rigorous

definition of the fractionation factor for a singular process is challenging, particularly in the dynamic marine environment.

To date, only two studies have experimentally investigated $\Delta^{138}Ba_{barite\text{-}dBa}$ related to $BaSO_4$ precipitation or formation. The seminal study of von Allmen et al. (2010) found an average $\Delta^{138}Ba_{barite\text{-}dBa}$ = -0.32 ± 0.03 ‰ based on the result of two experiments, one conducted at 21 °C and the other at 80 °C. Böttcher et al. (2018) found $\Delta^{138}Ba_{barite\text{-}dBa}$ = -0.25 ‰ during $BaSO_4$ precipitation in a solution containing methanol, and between -0.28 and -0.35 ‰ for $BaSO_4$ formation during transformation from gypsum ($CaSO_4 \cdot 2H_2O$). In the ocean, the comparisons of seawater and co-located particulates (Horner et al., 2017; Cao et al., 2020), regression of dissolved seawater data (Horner et al., 2015; Bates et al., 2017; Hsieh and Henderson, 2017), and the isotopic analysis of Ba in seawater and barite in marine sediments (Bridgestock et al., 2018; Crockford et al., 2019) imply a larger magnitude of $\Delta^{138}Ba_{barite\text{-}dBa}$ near -0.5 ‰. The magnitude of fractionation observed in field data likely represents an amalgam of multiple processes and/or differences in the dominant controls on fractionation when compared to laboratory experiments.

The magnitude of $\Delta^{138}Ba_{barite\text{-}dBa}$ related to $BaSO_4$ dissolution has not been investigated directly, though some studies have suggested that $BaSO_4$ dissolution is non-fractionating (i.e. $\Delta^{138}Ba_{barite\text{-}dBa} = 0$ ‰). Von Allmen et al. (2010) found that under highly alkaline conditions, partial dissolution does not significantly affect Ba isotopes of a fluid if at least 10% of the solid dissolves. Mavromatis et al. (2016) specifically state that their data cannot definitively rule out isotopic fractionation during dissolution, as their data could not be used to constrain potential re-equilibration of the fluid with the solid phase. Bridgestock et al. (2019) suggest that dissolution is non-fractionating based on $\delta^{138}Ba$ measured in particulates by Horner et al. (2017), which showed constant $\delta^{138}Ba$ in the particulates with depth. There is mainly inferred evidence for $\Delta^{138}Ba_{barite\text{-}dBa}$ = 0 ‰, though no direct study has confirmed the magnitude of fractionation during $BaSO_4$ dissolution. Further constraining this value will significantly improve the interpretation of $\delta^{138}Ba$ in environmental records.

1.4 Goals of this thesis

Hemingway famously wrote, “The sea is the same as it has been since before men ever went on it in boats.” In many ways, Hemingway was right: looking from shore, the sea can appear

vastly unchanging in its sameness, stretching away to the horizon. However, when men eventually *did* get around to building boats, we began to understand that the wine-dark sea held dynamic, ever-changing mysteries that I, as an isotope geochemist, will continue unravelling through the course of this dissertation. Proxy development, validation, and application reveals the story of the sea and allows modern humanity to enjoy both scientific and poetic descriptions of Earth's ocean. In pursuit of this goal, this work delves into three open questions regarding Ba isotope geochemistry, namely: (1) How does the process of ion exchange impact the isotopic signature of Ba in the dissolved phase and in $BaSO_4$? (2) Does ion exchange impart significant post-depositional changes in $\delta^{138}BaSO_4$? (3) What are the controls of pBa formation and spatial occurrence in the water column of the South Pacific Ocean?

Chapter 2 aims to understand the role of ion exchange between dissolved Ba and synthetic $BaSO_4$ under conditions relevant to the marine environment (Fig. 4, bubble 2). The goals of this chapter were to:

1) *Constrain rates of ion exchange near chemical equilibrium.*
2) *Evaluate the magnitude of isotopic fractionation associated with this process, particularly the interplay between the forward reaction (precipitation) and the back reaction (dissolution).*

Chapter 3 expands the findings of Chapter 2 into an environmental context to characterize the influence of ion exchange on pore fluid and co-located sedimentary barite in the Equatorial Pacific (Fig. 4, bubble 3). The goals of this chapter were to

2 *Provide secondary analysis of the rates of ion exchange and associated magnitudes of Ba isotopic fractionation using methods dissimilar to Chapter 2 to improve robustness.*
3 *Constrain the conditions under which this process may complicate paleoproxy reconstructions reliant on $\delta^{138}BaSO_4$.*

Chapter 4 offers the first measurements of pBa formation, associated controls, and Ba uptake rate carried out in the field, in the water column of the South Pacific Ocean over the Polar Frontal Zone (Fig. 4, bubble 1). The goals of this chapter were to:

1. *Assess the controls of particulate size and microbial activity on the rate of pBa formation.*
2. *Quantify the depth at which the majority of pBa forms.*
3. *Constrain the spatial distribution of pBa formation in order to clarify controls on the global distribution of Ba in the ocean.*

Chapter 5 presents a summary of the results within this thesis. This research encompasses the fieldwork, experimental implementation, lab analysis, and modelling necessary to measure environmentally needed to provide a unified assessment of the impacts of ion exchange on the use of Ba-based paleoproxies.

Figures

Fig. 1 Observational underpinnings of barium based paleoproxies: a) the correlation of dissolved Ba and Si in the ocean (GEOSECS data; modified from (Horner et al., 2015) and b) the correlation between BaAR and carbon export, as estimated by the application of an appropriate f ratio to primary productivity estimates, in the sediments (modified from Eagle et al., 2003).

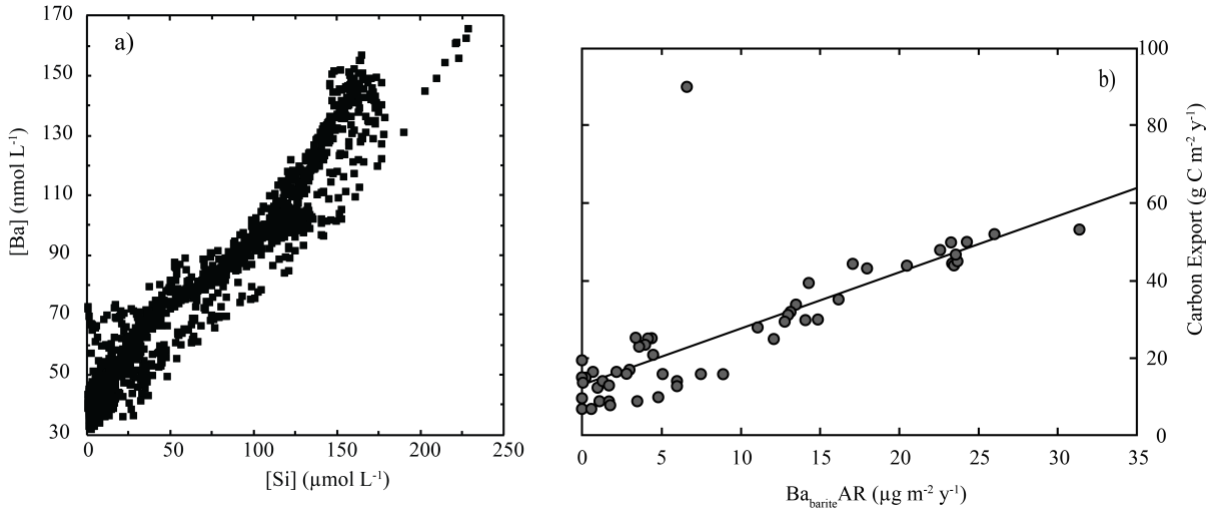

Fig. 2 Pelagic barite, Deep Sea Drilling Project Site 366 (modified from Griffith and Paytan, 2012).

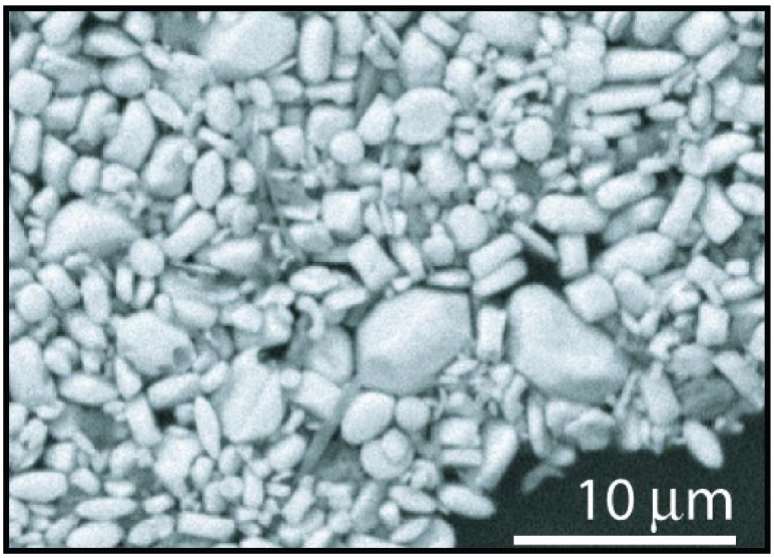

Fig. 3 Representative profiles of [Ba] and δ^{138}Ba from the Equatorial Pacific (reproduced from Chapter 2).

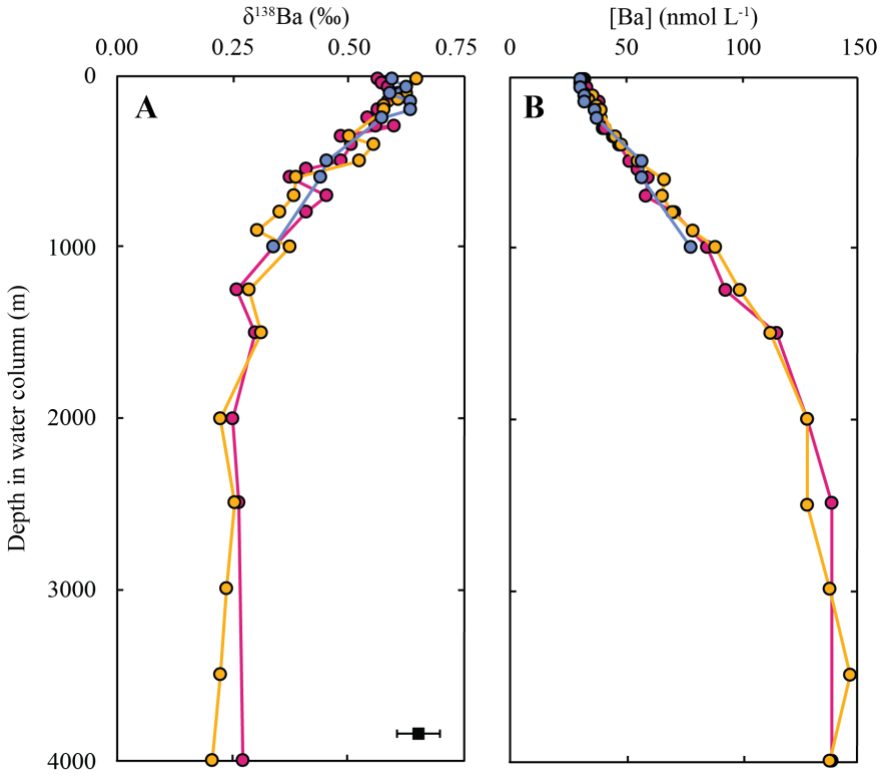

Fig. 4 Schematic of the three major themes explored in this thesis: controls on pBa formation (1), the effects of ion exchange in Ba-$BaSO_4$ systems (2), and the role of ion exchange in environmental settings (3). Graphic modified from work by Ichiko Sugiyama.

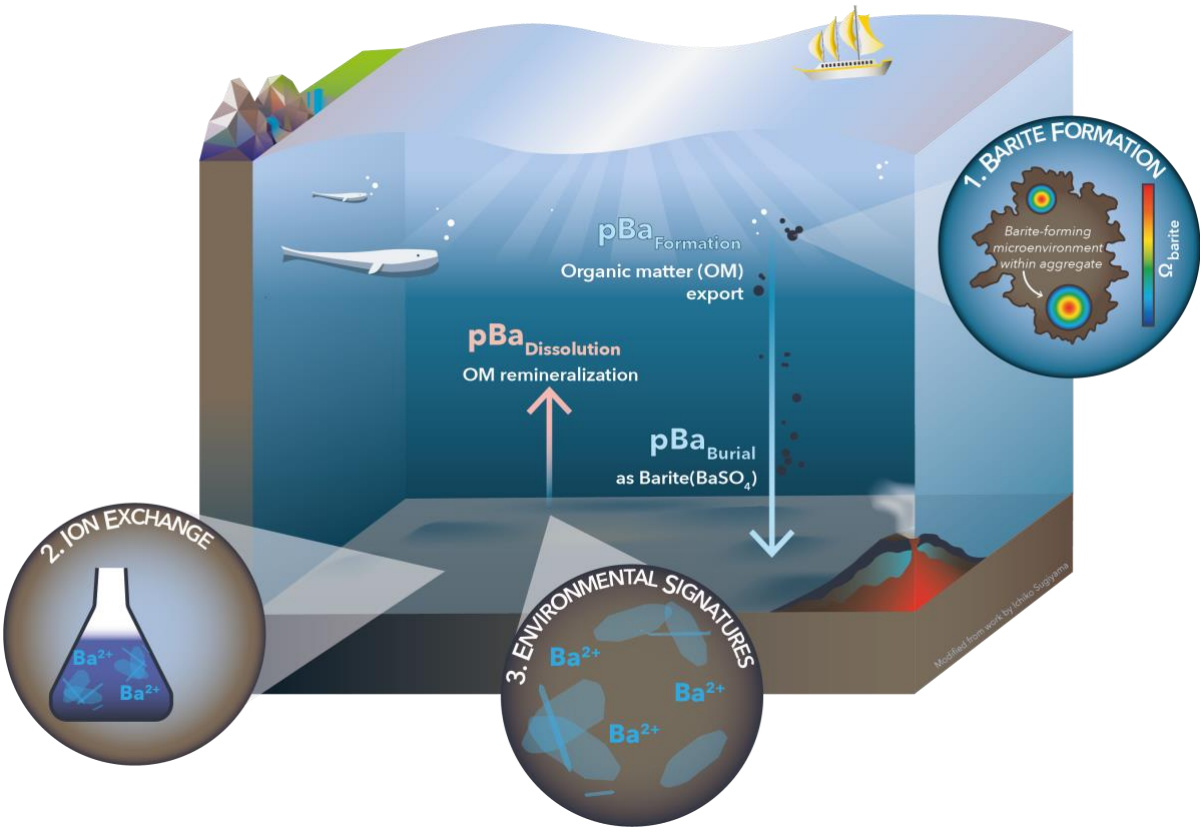

Chapter 2: Temporal evolution of barium isotopes during precipitation and at equilibrium in barite-fluid systems

Abstract

Pelagic barite is the dominant vector of particulate Ba in the modern ocean. Thus, the barium (Ba) isotopic composition of sedimentary barite ($BaSO_4$) offers a potential window into the sources and cycling of Ba in past marine environments. To reliably use Ba isotopes to interrogate the marine Ba-isotopic cycle, it is important to constrain the magnitude of processes fractionating Ba isotopes in pelagic $BaSO_4$ throughout the mineral's formation in surface waters, during sinking, and when buried in the sediments. However, while the greater magnitude of fractionation found by field measurements (-0.5 ‰) compared to laboratory $BaSO_4$ precipitation experiments (-0.32 ‰) suggests other factors influencing Ba isotopic, the identification and quantification of the governing processes have not been achieved to date. In this chapter, we interpret experimental observations using a reactor model to define the rate and isotopic effects of ion exchange in Ba-$BaSO_4$ systems under marine-relevant conditions. We find that Ba ion exchange progresses at a rate between 4 and 38 pmol m^{-2} s^{-1} and leads to a characteristic isotopic offset of $\Delta^{138}Ba_{barite–dBa}$ = -0.10 ± 0.05 ‰. This observed fractionation arises through the combined effects of micro-scale dissolution and precipitation at the mineral surface and can occur without any clear visual evidence of mineral alteration. Using the previously defined magnitude of fractionation for $BaSO_4$ precipitation, isotopic fractionation during $BaSO_4$ dissolution is found to fractionate Ba isotopes with $\Delta^{138}Ba_{barite–dBa}$ = +0.22 ‰. Such observations suggest that the isotopic composition of Ba in geologic $BaSO_4$ records should not be assumed to be fixed following their original precipitation.

2.1 Introduction

Barite ($BaSO_4$) formation and preservation in the world's ocean potentially offers a window into past ocean processes on timescales spanning the Precambrian to present. The dominant vector of particulate Ba transport in the ocean is via pelagic barite formation, which occurs in microenvironments within sinking particulate organic matter in an otherwise barite-undersaturated water column (Bishop, 1988; Carter et al., 2020). Pelagic $BaSO_4$ accumulation rates correlate with particulate organic matter export and remineralization, and have thus been used to reconstruct changes in past export productivity (e.g., Bridgestock et al., 2019; Dymond et al., 1992; Eagle et al., 2003; Paytan et al., 1996b). More recently, the Ba-isotopic composition of $BaSO_4$ has been used to clarify the environmental conditions under which barite precipitation can occur (Horner et al., 2017) and has been developed as a tracer for deep water mass circulation (Bates et al., 2017). These advances are contributing to our understanding of the controls on the global marine Ba cycle (Bridgestock et al., 2018; Crockford et al., 2019; Gou et al., 2020; Horner and Crockford, 2021), which in turn aids in further constraining past and present variations in the marine carbon cycle (Charbonnier et al., 2018; Bridgestock et al., 2019; Hodgskiss et al., 2019). Critical to many of these applications is the fidelity of the Ba isotopic ratio recorded in pelagic $BaSO_4$ and a mechanistic understanding of what governs Ba isotopic distributions within natural environments.

Barite precipitation is known to fractionate Ba isotopes. Profiles of dissolved Ba isotope compositions in seawater indicate that pelagic barite precipitation favors incorporation of isotopically "light" Ba, leaving the residual fluid correspondingly enriched in "heavy" Ba (e.g., Horner et al., 2015; Hsieh and Henderson, 2017). Variations in Ba-isotopic compositions are conventionally reported as deviations in the $^{138}Ba/^{134}Ba$ ratio in a sample relative to a standard (NIST SRM 3104a, hereafter 'NIST'):

$$\delta^{138}Ba = [(^{138}Ba/^{134}Ba)_{sample} /(^{138}Ba/^{134}Ba)_{NIST} - 1], \quad (1)$$

expressed in ‰. The magnitude of isotopic fractionation associated with a process, hereafter $\Delta^{138}Ba_{product-reactant}$, describes the isotopic offset between products and reactants, where

$$\Delta^{138}Ba_{product\text{-}reactant} = \delta^{138}Ba_{product} - \delta^{138}Ba_{reactant}. \quad (2)$$

In $BaSO_4$–dissolved Ba systems, $\Delta^{138}Ba_{barite-dBa} < 0$ indicates preferential incorporation of the lighter Ba isotopes into the solid phase and leaving the residual fluid isotopically heavy. Laboratory experiments conducted over short time periods (<1 d) at highly supersaturated conditions focused solely on barite precipitation and found the magnitude of isotopic fractionation to be $\Delta^{138}Ba_{barite-dBa}$ = -0.32 ‰ (von Allmen et al., 2010). However, the apparent fractionation factor measured in several independent field studies is nearer to a $\Delta^{138}Ba_{barite-dBa}$ value of -0.5 ‰. Field based $\Delta^{138}Ba_{barite-dBa}$ calculated by the comparisons of seawater and co-located particulates (Horner et al., 2017; Cao et al., 2020), regression of dissolved seawater data (Bates et al., 2017; Hsieh and Henderson, 2017), and the isotopic analysis of Ba in seawater and barite in marine sediments (Bridgestock et al., 2018; Crockford et al., 2019) are largely in agreement with one-another. To reliably use Ba isotopes to interrogate the marine Ba-isotopic cycle, it is important to constrain the magnitude of processes fractionating Ba isotopes in pelagic $BaSO_4$ throughout the mineral's formation in surface waters, during sinking, and when buried in the sediments. However, while the magnitude of fractionation found by field measurements suggests that other potential effects, in addition to precipitation, affect Ba isotopic distributions in $BaSO_4$, the governing processes have yet to be identified and quantified.

One mechanism known to impact the chemical composition of barite is ion exchange; however, the stable isotopic fractionation associated with this mechanism has not been studied. In the context of barite formation and preservation, ion exchange refers to surface mediated micro-scale dissolution and reprecipitation reactions (e.g. Heberling et al., 2018; Vital et al., 2020; Zhen-Wu et al., 2016), which allow barite to exchange a portion of its atoms with ions in the surrounding fluid while at apparent chemical equilibrium. Importantly, this exchange can occur with no observable changes in mineral structure, morphology, or grain size (e.g., Gorski and Fantle, 2017). Such processes are a potential route to alter the isotopic composition of barite precipitates in certain settings. Indeed, Ba radioisotope studies have shown that ion exchange occurs rapidly across a range of environmental conditions (Bosbach et al., 2010; Curti et al., 2010; Vinograd et al., 2013) and in some cases leads to complete re-equilibration of ions in the mineral lattice over only a few thousand years (Heberling et al., 2018). Such studies have focused on $BaSO_4$–fluid systems where the majority of Ba of resides in the dissolved phase and therefore has a high leverage to alter the

solid, unlike marine systems in which the vast majority of Ba is contained within $BaSO_4$. While informative, these previous studies offer constraints on the rate of ion exchange in $BaSO_4$–fluid systems in non-marine conditions, but do not quantify the impact of these processes on the stable isotopic composition of the endmembers. It is critical to know if these chemical alterations extend to the isotopic signature of Ba stored in pelagic barite to properly assess δ^{138}Ba of $BaSO_4$ (hereafter, $\delta^{138}BaSO_4$) as a carbon export and circulation proxy.

The experimental conditions highlighted above are not representative of the marine environment and thus offer limited constraints on the role of Ba ion exchange under marine-relevant conditions. This knowledge gap prevents a complete understanding of the isotopic information encoded via stable Ba-isotopic signatures in pelagic barite. Accordingly, the questions driving this work are: (1) Is there evidence of ion exchange in systems with extended contact between synthetic barite and seawater-like fluids? and (2) If ion exchange occurs, is there an associated mass-dependent isotopic fractionation impacting the isotopic composition of Ba in the dissolved and particulate phases? To begin addressing these questions, we investigated the existence of ion exchange using isotope tracer experiments. We also assessed the mass-dependent fractionation of Ba isotopes during barite precipitation and continuous interactions at bulk mineral-fluid equilibrium. Using a time-dependent multi-phase reactor model, we quantify the net rate of ion exchange into and out of barite using ^{135}Ba isotope tracer data and calculate the magnitude of associated mass-dependent Ba isotope fractionation. These new results identify a mechanism previously unknown to fractionate Ba isotopes and offer new insights into the fidelity of Ba-based proxies.

2.2 Materials & Methods

2.2.1 Experimental methods

All sampling materials, reagents, and sample handling were conducted in accordance with GEOTRACES protocols (Cutter et al., 2017). Specifically, this entailed acid cleaning of all labware, use of ultra-pure reagents (e.g., double-distilled mineral acids, high-purity reagents, 18.2 MΩ-grade H_2O), and conducting all critical sample handling within laminar flow

workbenches in the NIRVANA Labs metal-free workspace at the Woods Hole Oceanographic Institution (WHOI).

Experiments were seeded with 99.998 wt. % pure $BaSO_4$ (Puratronic, Alfa Aesar Lot #24177), with a nominal grain diameter of 3 μm. Strontium (Sr) accounted for the majority of impurities (0.002 wt. %), which is less than the [Sr] observed in pelagic marine barite (0.007 to 0.015 wt. %; (Monnin and Cividini, 2006). The synthetic $BaSO_4$ used has some differences in Sr content, morphology, and size distribution compared to pelagic $BaSO_4$, the latter having higher [Sr], being more anhedral, and slightly smaller (Fig. 1).

A 25 L stock of artificial seawater (ASW) was prepared following (Smith and Chanley, 1975) and brought to pH ≈ 8.1 by the addition of concentrated potassium hydroxide (KOH) solution. All reactions were carried out at near surface ocean conditions with a temperature (*T*) and salinity (*S*) of 17 ± 2 ℃ and 35 ± 0.5 respectively. A summary of experimental conditions for each reactor is shown in Table 1.

2.2.2 Isotope-tracer experiments for the identification of ion exchange in marine-like systems

The rate of exchange between barite and an artificial seawater solution was quantified through a series of incubations using ^{135}Ba (Oak Ridge National Laboratory, Lot #142890). Any ion exchange between $BaSO_4$, possessing natural Ba isotope abundances (i.e., ^{137}Ba:$^{135}Ba \approx 1.7$; (de Laeter et al., 2003), and dissolved Ba, with a measured initial $(^{137}Ba:^{135}Ba)_{fluid} = 0.022 \pm 0.0002$ (± 2SE, n = 6), would drive changes in $(^{137}Ba:^{135}Ba)_{fluid}$. In the isotope tracer experiments, the amount of ^{135}Ba spike added was adjusted based on *T*, *S*, and preexisting Ba in the ASW to achieve an initial Ω_{barite} of 1.3 —calculated using the aqueous geochemical modelling program PHREEQC (Parkhurst and Appelo, 2013). Tracer experiments were initiated at slightly super-saturated conditions of Ω_{barite} of 1.3 to prevent initial dissolution of barite and enable detection of ion exchange only.

Experiments were carried out in 1 L acid-washed HDPE (high-density polyethylene) bottles with continuous agitation (hereafter termed 'reactors'). Temperature was maintained at 20 ± 2 ℃ throughout the experimental period. Oxygen was not monitored, as reactors were fully abiotic and therefore oxygen drawdown is not expected. Ion exchange is evidenced to be a surface-mediated process (Bosbach et al., 2010; Zhen-Wu et al., 2016; Heberling et al., 2018; Oelkers et

al., 2019; Vital et al., 2020), therefore, I used a range of solid:fluid ratios (L_{barite}) to better define the net rates of Ba exchange between the mineral and the reactive fluid. The L_{barite} refers to the proportion of Ba in the solid phase. Here, the L_{barite} ranges between 0.999995 to 0.9995, to encompass the range in marine sediments corresponding to barite in the sediment and dissolved Ba in the pore waters as reported in the literature (Paytan et al., 1996a; Paytan & Kastner 1996). The equilibration solution (ASW) contained 26 ± 0.8 nM Ba (± 2SE, n = 5), derived from the salts used to prepare the artificial seawater. Following the addition of the isotope spike, initial $(^{137}Ba:^{135}Ba)_{fluid}$ equaled 0.02 ± 0.05 (± 2SE, *n* = 6) for all reactors (Table 2). The volume of the reactors (1 L) was sufficiently large to allow for the collection of multiple sub-samples over the experimental duration without decreasing the volume of solution by more than 5 %.

A blank reactor was used to assess any Ba adsorption onto reactor walls. This reactor was run under the same conditions as the ^{135}Ba-tracer experimental reactors, with two slight differences: the dissolved Ba came from a synthetic $BaCl_2 \cdot H_2O$ solution (Mallinckrodt Pharmaceuticals, ACS high purity grade, Lot #96847-1) and no barite was added so that [Ba] could be calculated for the blank reactor. The blank reactor was sampled at the initiation of the experiment and left undisturbed until the completion of the experiment at 180 days, after which it was sampled again.

2.2.3 Assessing changes in δ^{138}Ba related to Ba ion exchange

Experiments addressing potential changes in Ba isotopes related to ion exchange were conducted under the same conditions described above (Section 2.1.2.) with one key difference from the ^{135}Ba-tracer experiments: rather than initiating at a slightly supersaturated state with respect to $BaSO_4$, these reactors were initiated at significantly undersaturated conditions with [Ba] = 26.0 ± 0.6 nM (± 2SE, *n* =3) corresponding to an Ω_{barite} of 0.1 ± 0.04 (± 2SE, *n* =3) to allow an initial dissolution interval during which isotope changes arising from dissolution could be assessed (Oelkers et al., 2019). Experiments were sampled periodically until the concentration in the systems stabilized. Small contributions of Ba from the nominally Ba-free salts used to prepare the ASW rendered the initial isotope composition of the experiments at δ^{138}Ba = +0.10 ± 0.03 ‰ (±2SD, *n* = 7; exact values reported in Table 3). The reactors were incubated for 2 to 134 days under constant agitation. Each experimental condition was performed in duplicate, with one

replicate sacrificed at a midpoint in the experiment to allow quantification of the solid phase. At the conclusion of the experiments, reacted fluids were filtered through a 0.22 µm polyethersulfone (PES) membrane disc filter, acidified with HCl to 0.024 M (pH ≤ 2), and stored for several weeks before any further analysis.

2.2.4 Barite dissolution

Barite samples were dissolved through an alkaline dissolution in PFA vials, whereby a 1 M Na_2CO_3 solution (Puratronic, Alfa Aesar) was added to $BaSO_4$, forming $(Ba,Ca)CO_3$ (as in (Breit et al., 1985). Briefly, the amount of Na_2CO_3 added to each sample was adjusted to maintain a $BaSO_4$:Na_2CO_3 mass ratio of 1:10 and 18.2 MΩ water was added to the vials such that each sample contained 10 mg of $BaSO_4$ per 2 mL of solution. Following reagent addition, samples were sonicated for 60 minutes at room temperature and were then heated at 80 ℃ for ≥16 h. After cooling, the liquid containing Na and SO_4 was decanted. To ensure the complete conversion of $BaSO_4$ to $BaCO_3$, two further rounds of Na_2CO_3 addition, sonication, heating, and decantation were carried out for all samples. Following the third decanting, samples were rinsed with 18.2 MΩ water and the remaining solid, $BaCO_3$, was dissolved using 2 M HCl.

2.2.5 A modified time-dependent multi-phase reactor model for barium ion exchange

To model the laboratory experiments, we modified a time-dependent multi-phase reactor model that was developed previously (hereafter the 'Reactor model'; Sauer et al., 2021). A full description of the Reactor model assumptions, equations, implementation, and parameterization is found in the Supplement. Briefly, the Reactor model includes only two processes, $BaSO_4$ precipitation and dissolution, to effect the concentration of the four Ba isotopes of interest (^{134}Ba, ^{135}Ba, ^{137}Ba, and ^{138}Ba). Unlike previous studies, which assumed that $BaSO_4$ dissolution and precipitation are mutually exclusive (i.e. only one direction can occur at a time) and determined by $BaSO_4$ saturation, the Reactor model presented here allows simultaneous dissolution and precipitation as long as there is dissolved Ba (for precipitation) and $BaSO_4$ (for dissolution). Such a setup is consistent with ion exchange (Zhen-Wu et al., 2016; Heberling et al., 2018; Vital et al., 2020). Barite precipitation is formulated as follow:

$$^{135,137,138}R_{BP} = [^{135,137,138}Ba] \times \varphi \times L_{barite,ini} \times {}^{135,137,138}k_{precip} \quad (3)$$

$$^{134}R_{BP} = [^{134}Ba] \times \varphi \times L_{barite,ini} \times {}^{134}k_{precip} \times {}^{134/138}\beta_{BP} \quad (4)$$

where $^{13x}k_{precip}$ is the kinetic constant for precipitation of $^{13x}BaSO_4$. The dependency of $L_{barite,ini}$ suggests the kinetics of $BaSO_4$ precipitation also depends on the presence of $BaSO_4$ seed initially in the experiments. In order to account for the isotopic fractionation during $BaSO_4$ precipitation, an additional adjusting parameter, $^{134/138}\beta_{BP}$, is assigned to the rate expression of $BaSO_4$ precipitation for ^{134}Ba (Fig. S3). The ratios between $^{134}k_{prec}$ and $^{138}k_{prec}$ is constrained by the changes of the $\delta^{138}Ba$ from the solution in the laboratory experiments. As such, modelled rates are consistent with both the change in [Ba] and the change in $\delta^{138}Ba$ observed in experimental data.

As for $BaSO_4$ dissolution, the following rate expression is used:

$$^{135,137,138}R_{BD} = \left(\frac{[^{135,137,138}BaSO_4]}{MW_{135,137,138}}\right) \times (1-\varphi) \times \left(\frac{L_{barite}}{L_{barite,ini}}\right)^{(mrd)} \times \left(\frac{[Ba]_{eq}}{[Ba]_{ini}}\right)^{(1+mrd)} \times {}^{135,137,138}k_{diss} \quad (5)$$

$$^{134}R_{BD} = \left(\frac{[^{134}BaSO_4]}{MW_{134}}\right) \times (1-\varphi) \times \left(\frac{L_{barite}}{L_{barite,ini}}\right)^{(mrd)} \times \left(\frac{[Ba]_{eq}}{[Ba]_{ini}}\right)^{(1+mrd)} \times {}^{134}k_{diss} \times {}^{134/138}\beta_{BD} \quad (6)$$

where $^{x}k_{diss}$ is the kinetic constant for the dissolution of $^{x}BaSO_4$. The rates depend on both the changes in leverage with respect to its initial value ($L_{barite}/L_{barite,ini}$) and the degree of oversaturation (or undersaturation) as measured by the dissolved Ba concentration ratios between initial and equilibrium states ($[Ba]_{eq}/[Ba]_{ini}$ where $[Ba]_{eq}$ = 130 nM based on experimental results; Table S1). The factor is included for $^{134}BaSO_4$ dissolution to account for the potential isotopic fractionation during $BaSO_4$ dissolution.

2.3 Analytical methods

2.3.1 Measurement of ^{137}Ba:^{135}Ba in isotope tracer experiments

Isotope tracer samples were subsampled by removing an aliquot of 2 mL solution from the

reaction vessels, immediately filtering to a cutoff of 0.22 μm, and collecting the resultant solution. A second aliquot was subsampled from each of the filtered samples, diluted to 1900 μL with 2 % HNO_3, and spiked with indium (In)—an internal standard added to all standards samples, and blanks—to achieve a final [In] of 1 ng mL^{-1}. All samples were diluted and measured at a salinity of 1.75 to minimize non-spectral matrix effects. Filtered samples were analyzed for ^{137}Ba:^{135}Ba on a reverse quadrupole ICP-MS (iCAP-RQ, Thermo Fisher Scientific) at the WHOI Plasma Facility.

2.3.2 Barium isotope measurements

Non-tracer samples were prepared for Ba-isotopic analysis following the procedure outlined in Bates et al., 2017). Briefly, dissolved samples were equilibrated with a ^{135}Ba–^{136}Ba double spike of known concentration to achieve a spike- to sample-derived Ba concentration ratio between 1–2. Barium was pre-concentrated from 5 mL of seawater matrix through (Ba,Ca)CO_3 co-precipitation by drop-wise addition of 1 M Na_2CO_3 solution (Puratronic, Alfa Aesar). Samples were then dissolved in 250 μL of 2 M HCl in preparation for liquid ion-exchange chromatography. Ba was isolated by passing samples twice through 500 μL of AG 50W-X8 (200–400 mesh) cation-exchange resin (Bio-Rad), following the purification protocol described by Horner et al. (2015). Purified Ba was analyzed for Ba isotopes using a ThermoFinnigan Neptune multi-collector inductively coupled plasma mass spectrometer (MC-ICP-MS) at the WHOI Plasma Facility. Samples were aspirated using a PFA micro-concentric nebulizer at ≈ 140 μL min^{-1}, desolvated with a CETAC Aridus II, admixed with 3–5 mL min^{-1} of N_2, and introduced into the MC-ICP-MS. Ion currents corresponding to *m/z* 131 (Xe), 135 (Ba), 136 (Xe, Ba, Ce), 137 (Ba), 138 (Ba, La, Ce), 139 (La), and 140 (Ce) were simultaneously monitored in 30 × 4.19 s background-corrected integrations. All samples were analyzed at least of two times. Sample isotopic compositions were calculated using the three-dimensional geometric interpretation of the double-spike problem (Siebert et al., 2001) with additional processing for isobaric corrections (^{136}Xe and ^{136}Ce on ^{136}Ba, ^{138}Ce and ^{138}La on ^{138}Ba; Bates et al. (2017). Concentration- and spike-matched aliquots of NIST were measured every four samples and sample Ba isotope compositions were calculated relative to the average of the nearest four measurements of the NIST standard (i.e., two ahead, two behind). Contributions from non-experiment-derived Ba were assessed using nine ‘blanks’ in place of samples. Six procedural blanks constrain Ba contributions associated with sample preparation for

isotope analysis and were found to range from 1168 to 2123 pg. Three instrument blanks were found to range from 13 to 436 pg. Though higher than the long-term average procedural blank for co-precipitation of seawater samples (median = 1223 pg), the contribution of the highest blank to the sample with the lowest [Ba] was < 4 %. Given the low blank contribution and poor constraints on the true Ba-isotopic blank value, no blank correction was applied to the Ba-isotopic data. Sample uncertainties are reported as either a long-term measurement of uncertainty (±2 SD about the mean; ± 0.03 ‰, Horner et al. 2015) or pooled 2 SE (standard error) from the replicate analyses, whichever was found to be greater. Samples were analyzed with two, three, or four replicates depending on the concentration of Ba in the sample. Any uncertainties from the blank contribution were fully propagated into the final concentration and isotope data.

Accuracy of $BaSO_4$ and artificial seawater measurements was monitored by processing two internal reference materials alongside samples: NBS-127 ($BaSO_4$ powder) and GEOTRACES SAFe D1 (northeast Pacific seawater, 1,000 m). We found that NBS-127 and SAFe D1 possessed a δ^{138}Ba value of –0.29 ± 0.03 ‰ and +0.30 ± 0.04 ‰, in agreement with previous measurements of –0.29 ± 0.01 ‰ (Horner et al., 2017; Crockford et al., 2019; Tian et al., 2019) and +0.31 ± 0.03 ‰ (Hsieh and Henderson, 2017; Geyman et al., 2019; Cao et al., 2020), respectively.

2.3 Results

Representative SEM images of $BaSO_4$ prior to experimentation and those recovered from reactors harvested after 44.5 h (LB-ISO(2)) and 134 days (HB-ISO(1)) are shown in Fig. 1. Only $BaSO_4$ is evident in the images, as measured by SEM EDS, consistent with the stoichiometric dissolution of the mineral. There is no evidence of secondary $BaSO_4$ at this scale, as the size of individual crystals recovered from these experiments are similar to that of the initial $BaSO_4$ seed grains. The lack of secondary mineral precipitation is consistent with aqueous PHREEQC geochemical modelling results indicating that all other Ba containing minerals were undersaturated in the reactive fluid throughout the experiment (Parkhurst and Appelo, 2013).

2.3.1 Isotope-tracer experiments

The ^{135}Ba-tracer evolution of the reactive fluid during the experimental period is presented

in Table 2 and shown in Fig. 2. All reactors used to assess ion exchange were initiated with $(^{137}Ba:^{135}Ba)_{fluid}$ = 0.02 ± 0.05 (± 2SE, *n* = 6) and an initial $(^{137}Ba:^{135}Ba)_{solid}$ = 1.66 ± 0.07 (± 2SE, *n* = 3). The amount of Ba in the fluid was monitored by the blank-corrected counts per second (CPS) for the fluid at each timepoint. While this measurement cannot be converted into a true concentration because of the highly varying proportions of 135-Ba and 137-Ba, it is a useful tool to assess potential changes in $(^{137}Ba:^{135}Ba)_{fluid}$ due to any initial dissolution of $BaSO_4$ and to monitor the approach of the system to bulk mineral-fluid equilibrium. In all trials, Ba CPS relaxed from the initial value of 3.09E+05 ± 9E+03 (± 2SE, *n* = 6) toward a stable level of 3.6E+04 ± 5E+03 (± 2SE, *n* = 6) (Fig. S1). Equilibrium in ^{135}Ba-tracer experiments is taken to be when at least 3 consecutive measurements of CPS fall within uncertainty of each other. In the HB-135 and MB-135 reactors, equilibrium was reached within the first 44 h of the experimental period (Fig. S1). The LB-135(1) trial reached equilibrium after 144 h, while LB-135(2) was sacrificed after 44.5 h before equilibrium was attained. We attribute differences in equilibration times to the difference in available reactive surface area, with the LB-135 reactors containing the lowest mass of $BaSO_4$ and thus the lowest L_{barite}. As all experiments used the same $BaSO_4$ source, mass is taken to be directly correlated to surface area, therefore, the LB-135 reactors are assumed to have had the least amount of reactive surface area. The rapid approach to bulk mineral-fluid equilibrium and dependence on $BaSO_4$ surface area is consistent with the results reported by Zhen-Wu et al., (2016). Over the experimental time interval, the reactive fluid progressed from the initial $(^{137}Ba:^{135}Ba)_{fluid}$ toward $(^{137}Ba:^{135}Ba)_{solid}$ in all reactors (Fig. 2). The L_{barite} showed a strong control over this change, with the reactive fluid of HB-135 reactors reaching the $(^{137}Ba:^{135}Ba)_{solid}$ ratio in 1.6 h, MB-135(1) reaching the $(^{137}Ba:^{135}Ba)_{solid}$ ratio in 21.8 d, and LB-135(1) reaching the same value in 178 d, L_{barite} of 0.9995, 0.99995, and 0.999995, respectively. Solids were sampled from two reactors, MB-135(2) and LB-135(2) prior to the system reaching equilibrium. Consistent with the high leveraging by the solid $BaSO_4$ in the system (i.e., L_{barite} near 1), the $(^{137}Ba:^{135}Ba)_{barite}$ of the recovered solid was identical within uncertainty to that of the original $BaSO_4$ powder in all reactors.

2.3.2 Barium isotopic evolution

The chemical and isotopic evolution of a second set of reactors is presented in Table 3 and Figs. 3 - 5. These reactors were run in parallel to the ^{135}Ba-tracer experiments to quantify changes in the stable Ba isotope composition of the fluid over the course of the experimental period. Barium concentrations ($[Ba]_{fluid}$) varied significantly over the experimental period. In HB-ISO and MB-ISO reactors, initial dissolution of $BaSO_4$ lead to a significantly $BaSO_4$ oversaturated fluid phase with respect to $BaSO_4$ (Fig. 3). Concentrations increased to a maximum of 735 nM (Ω_{barite} = 5.2) before decreasing. In LB-ISO reactors, $[Ba]_{fluid}$ increased gradually to a maximum of 260 nM (Ω_{barite} = 1.9) after the first 33 minutes of the experiment before decreasing. Increases in dissolved Ba concentrations represent bulk mineral dissolution. Mass balance calculations indicate that as much as 0.06 % of $BaSO_4$ dissolved into the fluid phase to account for the increase in $[Ba]_{fluid}$ during the experimental period. After initial fluctuations, concentrations achieved a relatively stable value of $[Ba]_{final}$ = 130 ± 9 nM (± 2SE, n = 6, Table 3), which we assume represents an approach to Ω_{barite} = 1.0 in all reactors. Bulk mineral-fluid equilibrium in these reactors is taken to be when the saturation state is within 0.1 of Ω_{barite} = 1, which is a conservative estimate of the uncertainties in these saturation states. For these reactors, this encompasses fluids with [Ba] = 124 – 159 nM based on calculations using the aqueous geochemical modelling program PHREEQC.

Barium isotopes of the fluid in the reactors were measured throughout the course of the experiments. In reactors with high L_{barite}, $\delta^{138}Ba_{NIST}$ of the fluid decreased from an initial value of 0.50 ± 0.03 ‰ (HB-ISO(1)) and 0.32 ± 0.04 ‰ (HB-ISO(2)) to final values of 0.07 ± 0.04 ‰ and 0.09 ± 0.04 ‰, respectively (Fig. 4). MB-ISO reactors showed an initial enrichment of the fluid, followed by a subsequent decrease to 0.08 ± 0.05 ‰ (MB-ISO(1)) and 0.20 ± 0.03 ‰ (MB-ISO(2))). In both HB-ISO and MB-ISO reactors, enrichment of ^{134}Ba in the fluid led to δ^{138}Ba of the fluid approaching that of the $BaSO_4$, however the fluid remained offset from the solid. After the final sampling point for the reactor, HB-ISO(1) was offset from the solid by -0.09 ± 0.06 ‰ after 134 d and HB-ISO(1) by -0.12 ± 0.08 ‰ after 140 h. Similarly, MB-ISO(1) was offset from the solid by -0.10 ± 0.07 ‰ after 17.8 d and MB-ISO(2) by -0.25 ± 0.06 ‰ after 139 h. In LB-ISO reactors, the Ba isotopes exhibited complex behavior, with δ^{138}Ba of the fluid increasing or decreasing relative to the initial conditions at multiple time points (Fig. 4). After the final sampling point, LB-ISO(1) was offset from $BaSO_4$ by -0.11 ± 0.06 ‰ after 17.8 d and LB-ISO(2) was offset by -0.22 ± 0.06 ‰ after 46.5 h. The isotopic composition of $BaSO_4$ was measured at one point during the experimental period and again at the experiment's termination. All measurements found

$\delta^{138}BaSO_4$ within analytical uncertainty of the initial $BaSO_4$, as expected in these experimental systems due to the high L_{barite} (Table 3).

The Reactor model was fit to experimental data to determine the rate of ion exchange. Rates of ion exchange are shown in Table 4. Modelled rates of ion exchange were extremely consistent between experiments. While the exact value cannot be constrained measurement of the specific surface area of $BaSO_4$ in the experiments, estimates assuming spherical grains indicate that the value likely falls between 4 and 41 pmol m^{-2} s^{-1} (Table 4). Modelled rates of $BaSO_4$ precipitation were strongly dependent on [Ba] and largely independent from the amount of $BaSO_4$ precipitated. This suggests that near chemical equilibrium (i.e. $\Omega_{barite} = 1$), the degree of $BaSO_4$ saturation does not strongly control the kinetics of precipitation. The rate of $BaSO_4$ dissolution decreased with increasing L_{barite}, indicating that the bulk system characteristics had a degree of control over the rate at equilibrium.

2.4 Discussion

2.4.1 Evolution of $(^{137}Ba:^{135}Ba)_{fluid}$ over the experimental period

The $(^{137}Ba:^{135}Ba)_{solid}$ of $BaSO_4$ was measured at an intermediate and final timepoints, as the Ba isotopic composition of $BaSO_4$ was not expected to change significantly throughout the experiments. Similar to $BaSO_4$ within marine sediments previously used $BaSO_4$ for paleo-reconstructions (Paytan et al., 1996b), the vast majority of Ba in the experiments was present in the solid phase as the mineral $BaSO_4$. Mass-balance calculations for the LB-135 reactors (L_{barite} = 0.9995), shows that even in the event of complete ^{135}Ba-tracer uptake by solids in the reactors with the lowest amount of solid, the bulk $(^{137}Ba:^{135}Ba)_{solid}$ changed by only 0.0003, well below the range allowable by uncertainty in the measurement. Therefore, as expected from mass balance, $(^{137}Ba:^{135}Ba)_{solid}$ was found to be within analytical uncertainty of the initial solid at the termination of all reactors (Table 2).

Before interpreting $(^{137}Ba:^{135}Ba)_{fluid}$ data with respect to ion exchange, we first note (and rule out) two other processes unrelated to ion exchange which have the ability to contribute to changes in $(^{137}Ba:^{135}Ba)_{fluid}$, (1) Ba loss to adsorption to the reactor walls that could drive fluctuations in the amount of dissolved Ba, and (2) net $BaSO_4$ dissolution driving changes in

(^{137}Ba:^{135}Ba)$_{fluid}$. We assume that net precipitation during this relaxation has a negligible effect on (^{137}Ba:^{135}Ba)$_{fluid}$, as the magnitude of change in (^{137}Ba:^{135}Ba)$_{fluid}$ is well beyond what is possible by stable isotope fractionation for Ba during $BaSO_4$ formation. We assess the role of adsorption in the blank reactor with no solid $BaSO_4$ and find dissolved [Ba] remained within uncertainty of the initial value after 180 days. This implies that adsorption is not a major driver of fluctuations in dissolved [Ba] and agrees with previous findings of minimal adsorption of Ba in high-density polyethylene reactors (Fig. S2; Heberling et al., 2018). With respect to net $BaSO_4$ dissolution, an increase in counts per second (CPS), which represents the ion detection rate of the mass spectrometer and is directly correlated to concentration, occurred immediately following the addition of $BaSO_4$ to the reactor in some experiments. Net dissolution of $BaSO_4$ will increase (^{137}Ba:^{135}Ba)$_{fluid}$, as (^{137}Ba:^{135}Ba)$_{solid}$ $\gg$ (^{137}Ba:^{135}Ba)$_{fluid}$ at the initiation of each experiment. A conservative estimate of the contribution of net $BaSO_4$ dissolution to the progression of (^{137}Ba:^{135}Ba)$_{fluid}$ was calculated using a two-endmember isotope mixing equation. We use a mixing equation that accounts for reservoirs with unequal atomic masses, as our reservoirs have significantly different amounts of ^{135}Ba:

$$\left(\frac{^{137}\mathrm{Ba}}{^{135}\mathrm{Ba}}\right)_{fluid} = \left(\frac{^{137}\mathrm{Ba}_{initial\ solid} + {}^{137}\mathrm{Ba}_{initial\ fluid}}{^{135}\mathrm{Ba}_{initial\ solid} + {}^{135}\mathrm{Ba}_{initial\ fluid}}\right) \text{ , and} \quad (3)$$

$$^{m}\mathrm{Ba}_{A} = \left(\frac{f_A + {}^{m}F_A + \mathrm{Ba}_{total} + N_{Avogadro}}{{}^{m}AW}\right) \quad (4)$$

where f_A = ($CPS_{initial} - CPS_{post\ barite\ addition}$)/$CPS_{initial}$ is the fraction of dissolved Ba added to the fluid due to some initial dissolution of $BaSO_4$, ${}^{m}F_A$ is the fraction of Ba that is isotope *m* in pool *A*, Ba_{total} is the total grams of Ba in the reactor, $N_{Avogadro}$ is Avogadro's number, and ${}^{m}AW$ is the atomic weight of isotope *m*. Three reactors saw an increase in Ba CPS following the addition of $BaSO_4$: HB-135(1), LB-135(1), and LB-135(2). Based on the mixing calculation, $BaSO_4$ dissolution was expected to change the (^{137}Ba:^{135}Ba)$_{fluid}$ 0.18, 0.03, and 0.05, respectively. In all three cases, (^{137}Ba:^{135}Ba)$_{fluid}$ changed significantly more than these calculated values, implying processes other than net dissolution impacting the evolution of (^{137}Ba:^{135}Ba)$_{fluid}$. Having ruled out significant adsorption of Ba to reactor walls and constraining the influence of net $BaSO_4$ dissolution at the

initiation of the experiment, we interpret further changes in (^{137}Ba:^{135}Ba)$_{fluid}$ as resulting from ion exchange between the dissolved and solid phases in the system.

The chemical evolution of the fluid and $BaSO_4$ during all tracer experiments is presented in Table 2 and show in Fig. 2 and Fig. S1. In all reactors, (^{137}Ba:^{135}Ba)$_{fluid}$ increased monotonically from the initial ^{135}Ba-tracer dominated value toward (^{137}Ba:^{135}Ba)$_{barite}$. The L_{barite} in the system had a strong effect on the apparent rate of exchange, with the HB-135 reactors exhibiting a rapid increase in (^{137}Ba:^{135}Ba)$_{fluid}$ from 0.02 to 1.45 and 1.54 within the first four minutes for reactors 1 and 2, respectively. By comparison, the MB-135 trials and LB-135(1) with lower L_{barite} increased to a similar value after only 1.7 h and 41 d, respectively. Experiment LB-135(2), with similar L_{barite} as LB-135(1), never reached this value due to the slow progression of the fluid and termination of that reactor at the midpoint for the measurement of $BaSO_4$. While specific surface area was not measured for $BaSO_4$ in these experiments, the net rate of ion exchange is strongly dependent on the total mass of $BaSO_4$ in each reactor which we use anecdotally as a proxy for total surface area (Fig. 2). The dependence of ion exchange on available surface area agrees with models describing surface-mediated ion exchange of Ba and radium (Ra) into $BaSO_4$ (Curti et al., 2010; Heberling et al., 2018).

Notably, in HB-135 the approach of (^{137}Ba:^{135}Ba)$_{fluid}$ to the (^{137}Ba:^{135}Ba)$_{barite}$ value occurred within the initial period of CPS changes. In MB-135 and LB-135(1), (^{137}Ba:^{135}Ba)$_{fluid}$ continued to evolve toward (^{137}Ba:^{135}Ba)$_{barite}$ after the system had attained bulk mineral-fluid equilibrium. Having ruled out significant adsorption of Ba to reactor walls and constraining the influence of net $BaSO_4$ dissolution at the initiation of the experiment, we interpret the progression of (^{137}Ba:^{135}Ba)$_{fluid}$ toward (^{137}Ba:^{135}Ba)$_{solid}$ as representative of ion exchange between the dissolved and solid phases in the system. The continued evolution of (^{137}Ba:^{135}Ba)$_{fluid}$ in MB-135 and LB-135(1) while at a constant total dissolved Ba concentration (i.e. bulk mineral-fluid equilibrium) requires ^{135}Ba to be incorporated into and ^{137}Ba to be released from $BaSO_4$ in equal quantities but opposite directions (i.e. ion exchange). This behavior is consistent with the concept of dynamic equilibrium, which allows the $BaSO_4$-fluid system to evolve and change even after bulk mineral-fluid equilibrium has been reached.

2.4.2 Temporal variation of reactive fluid [Ba] and approach to $\Omega_{barite} = 1$

Changes in [Ba] produced by the Reactor model fit well to measured values and captures the overall trends in the fluid (Fig. 5). Modeled rates of ion exchange are dependent on the L_{barite} in each experiment (Table 4), consistent with ion exchange occurring as a surface-mediated process (e.g., Bracco et al., 2017; Heberling et al., 2018; Vital et al., 2020; Zhen-Wu et al., 2016). The final [Ba] in the HB-iso(1), MB-iso(1), and LB-iso(1) reactors, which is taken to be the bulk mineral-fluid equilibrium value (as discussed above), similarly depends on L_{barite} (Table 4). Although $[Ba]_{equilibrium}$ was relatively consistent between experiments, observation of a slight increase in $[Ba]_{equilibrium}$ with increasing L_{barite} may indicate local disequilibrium at the solid surface allowing greater barite dissolution (as in Chanda et al., 2019). Under this scenario, as L_{barite} increases, local disequilibria allow for a greater net rate of dissolution and a proportionate increase in net re-precipitation, leading to the observed dependence on the calculated rate of ion exchange on L_{barite}. Although there is some uncertainty in fitting these fast reaction rates, they are consistent with prior measurements of the rate of ion exchange (Curti et al., 2010; Torapava et al., 2014; Brandt et al., 2015; Heberling et al., 2018).

2.4.3 Temporal evolution of $\delta^{138}Ba$ during $BaSO_4$ precipitation, dissolution, and at equilibrium

The isotopic composition of the reactive fluid, particularly the progressive enrichment of the fluid in light isotopes despite a significant decrease in [Ba] followed by constant [Ba], indicates processes in addition to fractionation during $BaSO_4$ precipitation influenced $\delta^{138}Ba$ in the fluid. As previously discussed in Section 4.1, we find that adsorption to reactor walls does not significantly impact our experiments. Barite precipitation is known to fractionate Ba isotopes with $\Delta^{138}Ba_{barite-dBa}$ = -0.32 ± 0.02 ‰ following either closed-system Rayleigh distillation or steady state fractionation (von Allmen et al., 2010). As Rayleigh distillation occurs only during unidirectional reactions, it is not appropriate for the description of Ba isotope fractionation during ion exchange near chemical equilibrium, which comprises Ba ion exchange both into and out of $BaSO_4$.

The chemical and isotopic composition of the fluid phase over the course of the experimental period may be described by two distinct processes. First, net $BaSO_4$ precipitation occurs and imparts the characteristic magnitude of fractionation described by von Allmen et al. (2010). Note that the reactors reach some degree of supersaturation during the initial stages of precipitation, such that mass transfer is dominated by the net removal of Ba from the aqueous to

solid phase (e.g. the forward reaction, precipitation, dominates over the reverse reaction, dissolution, as found by Schott and Oelkers, 1995; Oelkers and Schott, 2001; Schott et al., 2009; Oelkers et al., 2018). As such, the preferential uptake of the light isotope into $BaSO_4$ is evident in the enrichment of the fluid during the early stages of the MB-iso trials and LB-iso(1) and throughout LB-iso(2) as this is the dominant process occurring (Figs. 4, 5). As the system approaches bulk mineral-fluid equilibrium, the back reaction (dissolution) becomes evident as the isotopic composition of the fluid becomes progressively depleted in ^{138}Ba. The observed temporal evolution of $\delta^{138}Ba$ in the fluid most likely reflects initial kinetic fractionation of Ba isotopes as the system precipitates $BaSO_4$, followed by a longer period of ion-exchange-mediated isotopic equilibration that gradually overprints the initial precipitation-driven isotopic signature. These variations are consistent with the calculations of Druhan et al. 2013) and Steefel et al. (2014), which predict isotopic equilibration of a mineral-fluid system in the absence of bulk chemical disequilibrium based on Transition-State Theory. In HB-iso, where L_{barite} was highest amount of $BaSO_4$ precipitated (if any) is small and ion exchange dominates the isotopic composition of the fluid for the entirety of the experimental period (Fig. 4). Dependence on the availability of reactive surface area is congruous with other works examining the re-equilibration of fluids in solid-fluid systems undergoing ion exchange (e.g. Gorski and Fantle, (2017) and references therein).

2.4.4 Evaluation of $\Delta^{138}Ba_{barite-dBa}$ using the Reactor model

The relative rate of reaction of ^{138}Ba and ^{134}Ba are used to determine the fractionation factors associated with precipitation and dissolution, where

$$\alpha_{process} = {}^{138}k_{process} \Big/ {}_{134}k_{process}. \quad (7)$$

For $\alpha \approx 1$, the magnitude of isotopic fractionation ($\Delta^{138}Ba_{product\text{-}reactant}$), is accurately approximated as

$$\Delta^{138}Ba_{product\text{-}reactant} = 1000 \times \ln(\alpha_{process}). \quad (8)$$

The magnitude of isotopic fractionation is constrained by the final offset of the dissolved phase and $BaSO_4$ in HB(1), MB(1), and LB-Iso(1). As $\Delta^{138}Ba_{barite–dBa}$ in experimental reactors represents the net effect of the forward reaction (precipitation) and the back reaction (dissolution), the Reactor model offers a non-unique solution (Fig. 6). We constrain the forward rate constants of precipitation, $^{138}k_{precip}$ and $^{134}k_{precip}$, using the findings of von Allmen et al. (2010), who found $\alpha_{precip} = 0.99968 \pm 0.00002$ (±2SE, $n = 3$). As discussed in von Allmen et al. (2010), this fractionation factor arises from dehydration of the cation, reaction kinetics, and a surface entrapment of the lighter isotope. Given this constraint, the fractionation factor associated with $BaSO_4$ dissolution is found to be $\Delta^{138}Ba_{dBa\text{-}barite} = -0.22 \pm 0.05$ ‰. Notably, the convention of writing $\Delta^{138}Ba_{product\text{-}reactant}$ makes the sign of this value opposite that of the magnitude of fractionation for $BaSO_4$ for precipitation. For clarity, we report this value in barite-dBa space as $\Delta^{138}Ba_{barite–dBa} = +0.22 \pm 0.05$ ‰.

2.4.5 Implications for preservation of the primary signature in marine $BaSO_4$

Here, we show that ion exchange occurs in $BaSO_4$-fluid systems at salinity, temperature, Ba concentrations, $BaSO_4$ crystal size, and L_{barite} relevant to marine sediments and fractionates Ba isotopes. These results are consistent with similar findings under a broader range of conditions relevant to the nuclear energy industry (Bosbach et al., 2010; Curti et al., 2010; Vinograd et al., 2013; Torapava et al., 2014; Brandt et al., 2015; Heberling et al., 2018). Critically, our experiments illustrate that ion exchange allows the Ba isotopic composition of dissolved Ba to evolve towards isotopic equilibrium after bulk $BaSO_4$-fluid chemical equilibrium has been achieved. Given the high L_{barite} in our experimental system, changes in $\delta^{138}BaSO_4$ are within of analytical precision, as indicated by the lack of variability in $\delta^{138}BaSO_4$ measured throughout the experiment (Fig. 4, crosses). Despite this important caveat, the temporal evolution of $\delta^{138}Ba$ in the fluid implies concurrent evolution of the isotopic composition of the solid. Generally, this challenges the commonly held assumption that $BaSO_4$ preserves the primary isotopic signature of Ba over geological time scale. Such processes, if also valid in naturally occurring $BaSO_4$ in contact with a fluid, may influence the pristine isotopic composition of the precipitating mineral and complicate interpretations of $\delta^{138}BaSO_4$ in a carbon export context.

Careful site selection should ameliorate potential effects of ion exchange on the primary isotopic signature of Ba preserved in $BaSO_4$ and thereby allow continued use of $\delta^{138}BaSO_4$ as a proxy. In environmental settings, the ability of ion exchange to overprint primary $\delta^{138}BaSO_4$ likely depends on several factors, including the amount of reactive surface area, the ratio of Ba in $BaSO_4$ to that in the pore water (L_{barite}), and supply of new dissolved Ba to pore waters. The rate of ion exchange will also depend on the available reactive surface area of sedimentary pelagic $BaSO_4$. Organic coatings or coatings by iron-oxyhydroxides of sedimentary pelagic $BaSO_4$ can decrease the reactive surface area and thereby limit ion exchange. Mineral-associated organic coatings have previously been found to cover generally less than 15 % of mineral surfaces in marine sediments (Mayer, 1999; Arnarson and Keil, 2001), rendering this mechanism of likely low significance, however such data specific to $BaSO_4$ is not available. Similarly, the role of manganese and iron-oxides should be investigated further, as Ba is known to be complexed by these compounds (Gingele et al., 1999; Charette et al., 2005), however these data are not available for the cores reported on in this study. The reactivity of $BaSO_4$ surface may change over time. Prior studies indicate that the rate of ion exchange in $BaSO_4$ slows over time due to the mineral becoming more stable, and therefore less reactive (Bosbach et al., 2010; Gorski and Fantle, 2017). Slowing ion exchange would lead to a decreasing rate of isotopic alteration. Therefore, there may be an initial period of ion-exchange-mediated diagenesis, followed by a stable composition of $\delta^{138}BaSO_4$.

If ion exchange impacts $BaSO_4$ in the environment, the isotopic composition of $BaSO_4$ will depend strongly on whether a sediment core is $BaSO_4$-buffered (high L_{barite}) or fluid-buffered (low L_{barite}), as the phase containing the most Ba will dominate the ultimate $\delta^{138}BaSO_4$ set through long-term ion exchange. Barite collected from sediments with high L_{barite} will likely exhibit a $\delta^{138}BaSO_4$ within analytical uncertainty of the primary isotopic signature imparted during $BaSO_4$ formation. Sites of this type are idea for $BaSO_4$ collection and measurement of $\delta^{138}BaSO_4$, as the primary isotopic signature should be preserved. On the other end of the spectrum, pore-fluid-buffered systems will be more prone to erasure of primary $\delta^{138}BaSO_4$, as ambient fluids will have greater leverage over the $\delta^{138}Ba$ of the system. Although further study is needed, these pore-fluid-buffered systems represent a setting in which the isotopic composition of Ba in $BaSO_4$ may be used to assess early marine diagenesis. This may be especially true in sedimentary settings in which sedimentary pelagic $BaSO_4$ is in contact with pore fluids that experience some diffusive flux of dissolved Ba (McManus et al., 1998). Similarly, some sedimentary settings, including areas with hydrothermal

circulation and cold seep environments, may have significant pore fluid flow and elevated [Ba] (Snelgrove and Forster, 1996; Hu et al., 2019; Rooze et al., 2020). Both diffusive fluxes and active flows through pore fluids have the potential to supply 'new' dissolved Ba to $BaSO_4$ surfaces and therefore may impact $\delta^{138}BaSO_4$ *even* in systems with high L_{barite}. Further study is certainly needed to constrain the effect of pore fluid flow on the supply of dissolved Ba to pore fluids and how the resultant flux of dissolved Ba might impact $\delta^{138}BaSO_4$ of co-located $BaSO_4$.

Regardless of the value of L_{barite} in the environment, it is possible that ion exchange only affects the surface layer or $BaSO_4$ while the bulk mineral may be preserved. The amount of Ra in $BaSO_4$ has a strong control on the degree of crystal restructuring my ion exchange, with increasing Ra content leading to greater solid-solution behavior and propagation of Ra entering $BaSO_4$ into the interior of the crystal (Curti et al., 2010). Homogenization of the signatures imparted on $BaSO_4$ through ion exchange has been observed to affect anywhere between a small rind of the $BaSO_4$ crystal (Heberling et al., 2018) to full homogenization of the mineral grain (Curti et al., 2010; Brandt et al., 2015; Weber, 2017). In environmental records, Ra contained within $BaSO_4$ is used to reconstruct sediment age models (Paytan et al., 1996a). There is certainly a need for future studies addressing the interaction of Ra, $BaSO_4$, and the permeation of isotopic signatures imparted by ion exchange into the interior of $BaSO_4$ crystals.

Based on our findings, we suggest that oxygenated sites with high L_{barite} and minimal supply of new dissolved Ba to the pore fluids are ideal for use of $\delta^{138}BaSO_4$ as a proxy. Generally, areas with high export productivity impart sediments with significantly more $BaSO_4$ than other regions (Paytan and Kastner, 1996; Eagle et al., 2003; Bridgestock et al., 2018), aiding in the maintenance of a high L_{barite}. However, care must be taken in areas of very high organic matter export, which may create sulfidic sediments in which $BaSO_4$ will undergo net dissolution, thereby decreasing L_{barite}. More work is needed to assess whether sedimentary pelagic $BaSO_4$ in these regions exhibit post-depositional alteration of the $\delta^{138}BaSO_4$ due to ion exchange. Studies examining $BaSO_4$ and co-located pore waters will be critical for interrogating this process and establishing what conditions preserve the primary $\delta^{138}BaSO_4$ over geological timescales.

2.5 Conclusions

The results summarized above provide evidence of ion exchange and the co-evolution of mineral isotopic signatures towards isotopic equilibrium in $BaSO_4$-fluid systems at bulk mineral-fluid equilibrium under marine-like conditions. This alteration is thought to progress through micro-scale dissolution and reprecipitation reactions (e.g. (von Allmen et al., 2010; Zhen-Wu et al., 2016; Heberling et al., 2018; Vital et al., 2020). We find the rate of ion exchange to be consistent between trials. While the true value cannot be constrained because a lack of knowledge about the reactive surface area, estimates assuming spherical grains indicate that the value likely falls between 4 and 41 pmol m^{-2} s^{-1} (Table 4). The combined effect of $BaSO_4$ dissolution and precipitation, with $\Delta^{138}Ba_{barite–dBa}$ of +0.22 ‰ (this study) and -0.32 ‰ , leads to an ion-exchange mediated the observed $\Delta^{138}Ba_{barite–dBa}$ = -0.10 ± 0.05 ‰. This alteration of isotopic signatures can occur without any clear visual evidence of mineral alteration. Such observations suggest that the isotopic composition of Ba in geologic $BaSO_4$ records should not be assumed to be fixed following their original precipitation. The degree to which the primary isotopic signature is overprinted in $BaSO_4$ will depend on L_{barite}, the degree to which these phases are out of isotopic equilibrium, the reactivity of environmental $BaSO_4$, and the supply of new dissolved Ba to pore fluids. Similarly, as the isotopic composition of the fluid phase is strongly influenced by interactions with coexisting $BaSO_4$ over relatively short time periods, it seems unlikely that flowing pore fluids preserve pristine records of $\delta^{138}BaSO_4$.

Acknowledgements

Thanks to Peter Crockford (WHOI) and Sune Nielsen (WHOI) for illuminating discussions, and Gretchen Swarr and Jerzy Blusztajn for assistance in the WHOI Plasma Facility. Thanks to Christopher Kinsley for providing a SEM image of pelagic barite. We acknowledge financial support from the National Science Foundation: a Graduate Research Fellowship (J.T.M.), OCE-1827401 (T.J.H. & A.P.), and EAR-1053312 (to E.M.G.).

Figures and Tables

Fig. 1 SEM images of (a) Alfa Aesar reagent barite used in ^{135}Ba-tracer and stable isotope experiments and (b) pelagic barite in association with diatoms. The pelagic barites are seen in bright white. SEM images of the synthetic barite were taken (a) pre-experimentation and after the termination of (c) LB-iso(1) and (d) HB-iso(1).

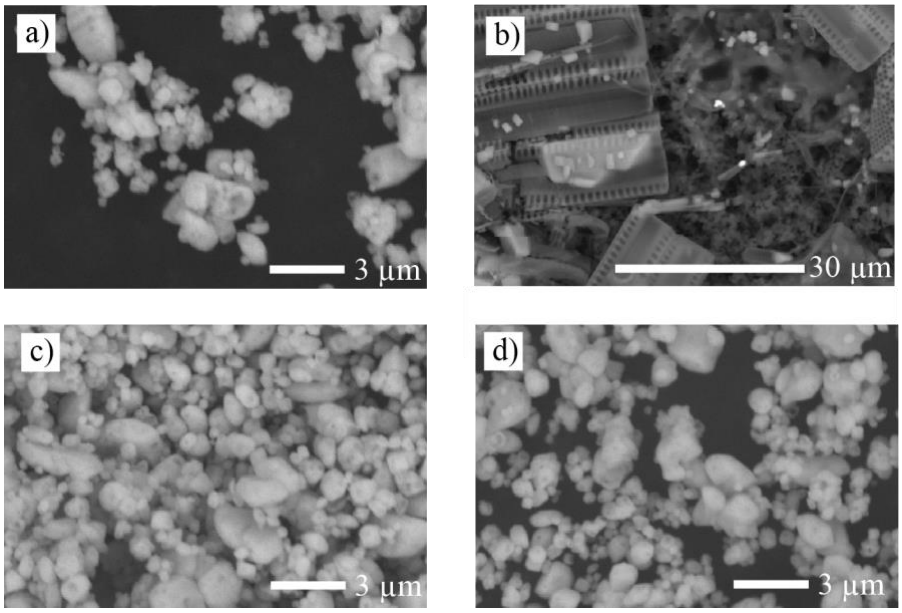

Fig. 2 Temporal evolution of ^{135}Ba-tracer experiments. Initial (^{137}Ba:^{135}Ba) of the fluid and barite are shown in grey lines, with the width of the line representing the uncertainty interval. HB-135 trials (squares), MB-135 trials (circles), and LB-135 trials (diamonds) are shown, with trial 1 shown in open symbols and trial 2 with filled symbols. All experiments evolve from the initial ^{135}Ba-dominated composition of the fluid toward (^{137}Ba:^{135}Ba) of the solid. Evolution of (^{137}Ba:^{135}Ba)$_{fluid}$ continues to progress following attainment of bulk mineral-fluid equilibrium. Bulk mineral-fluid equilibrium is reached after 44 h in HB-iso and MB-iso trials, and after 144 h in LB-iso(1). For clarity, (^{137}Ba:^{135}Ba)$_{solid}$ is plotted separately in the top panel. All solids fall within uncertainty of the initial barite.

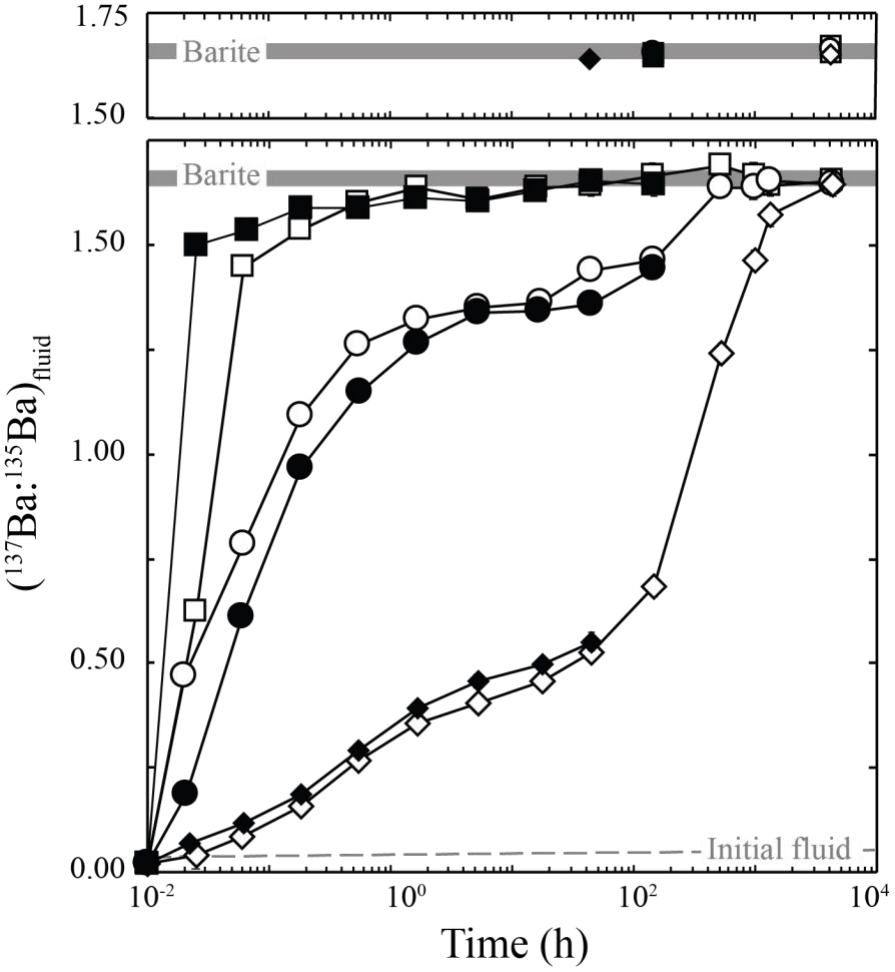

Fig. 3 Temporal evolution of [Ba] in experiments assessing stable Ba isotope fractionation, with trial 1 shown in open symbols and trial 2 with filled symbols for HB-ISO (squares), MB-ISO (circles), and LB-ISO (diamonds). The uncertainty of measured [Ba] fall within the points.

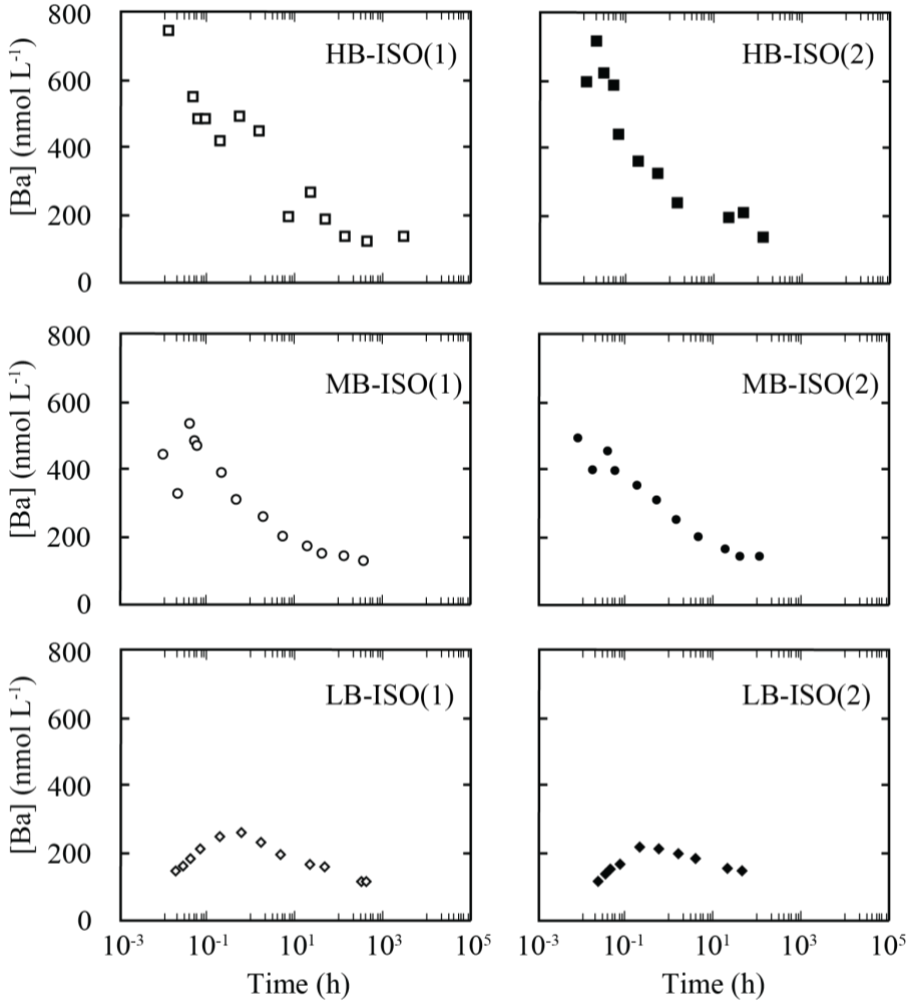

Fig. 4 Temporal evolution of δ^{138}Ba in in experiments assessing stable Ba isotope fractionation, with trial 1 shown in open symbols and trial 2 with filled symbols for HB-ISO (squares), MB-ISO (circles), and LB-ISO (diamonds). Rayleigh distillation and steady-state fractionation predict a progressing enrichment of the fluid in the heavy isotope (von Allmen et al., 2010), while the measured composition of the fluid became progressively enriched in the light isotope. Uncertainty for all points is represented by the grey error bar in the HB-ISO(1) panel.

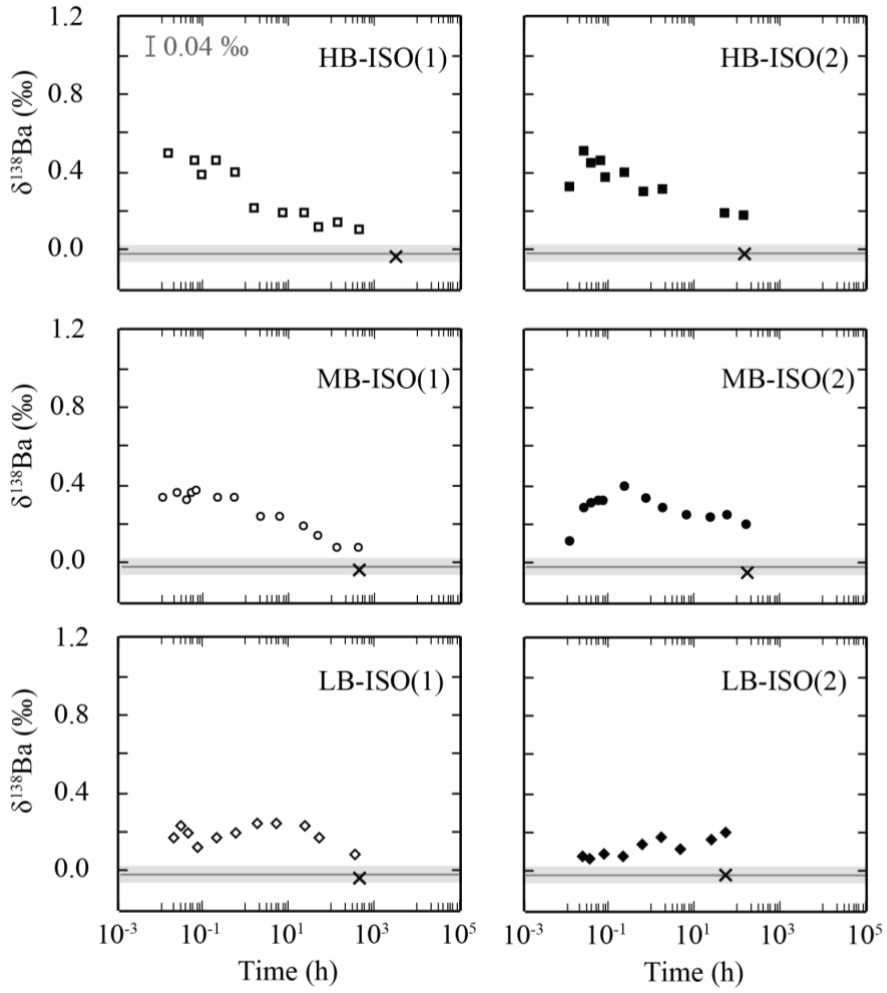

Fig. 5 Reaction-diffusion model results for the HB experiments (L_{barite} = 0. 999995). The unified model fits [Ba], $\delta^{138}Ba$, and $(^{135}Ba/^{137}Ba)_{fluid}$ simultaneously to calculate the rate of ion exchange. The model fit is shown in each panel by the solid black line. The composition of $BaSO_4$ (dashed line) is show in b) and c). The modeled rate of ion exchange are shown Table 4.

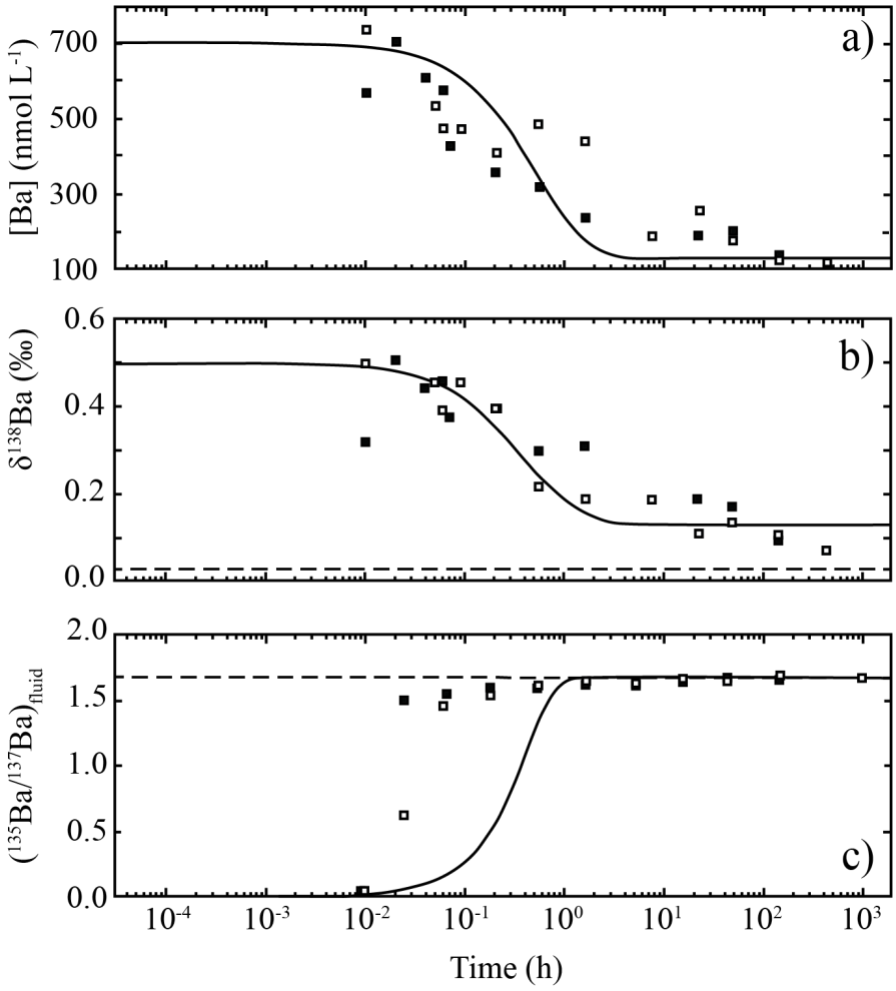

Fig. 6 Heat map of the magnitude of fractionation ($\Delta^{138}Ba_{barite–dBa}$) produced by different combinations of the fractionation factors for precipitation ($\alpha_{precipitation}$) and dissolution ($\alpha_{dissolution}$). Von Allmen et al. (2010) constrain the isotopic fractionation of Ba during $BaSO_4$ precipitation as $\alpha_{precipitation}$ = 0.99968. The start represents the point at which the average observed final offset between the fluid and $BaSO_4$ in HB-iso, MB-iso, and LB-iso (-0.1 ‰) and the criteria of Von Allmen et al. (2010) are both observed. The resultant $\alpha_{dissolution}$ = 0.99978.

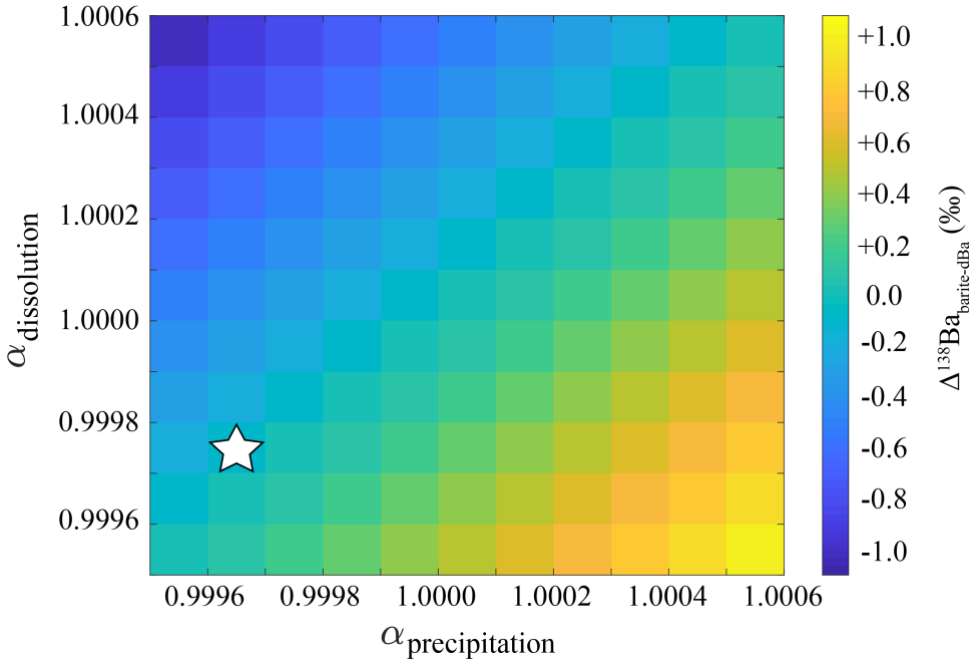

Table 1

Initial conditions for all experiments run in this study

Experiment	L_{barite}	Initial Ω_{barite}	Initial [Ba] (nM)	Initial $(^{137}Ba:^{135}Ba)_{fluid}$
HB-135(1)	0.999995	1.3	269.2	0.02
HB-135(2)	0.999995	1.3	250.8	0.02
MB-135(1)	0.99995	1.3	260.6	0.02
MB-135(2)	0.99995	1.3	260.2	0.02
LB-135(1)	0.9994	1.3	251.0	0.02
LB-135(2)	0.9994	1.3	269.3	0.02
HB-iso(1)	0.999995	0.1	26.0	
HB-iso(2)	0.999995	0.1	26.0	
MB-iso(1)	0.99995	0.1	26.0	
MB-iso(2)	0.99995	0.1	26.0	
LB-iso(1)	0.9995	0.1	26.0	
LB-iso(2)	0.9995	0.1	26.0	

Table 2

Experimental data from experiments evaluation the temporal evolution of $(^{137}Ba:^{135}Ba)_{fluid}$ over the course of experiments.

Experiment.sample	Time (h)	$(^{137}Ba:^{135}Ba)_{fluid}$	±2SE
HB-135(1) pre barite-addition	0.0	0.02	0.05
HB-135(1).1	0.0	0.62	0.01
HB-135(1).2	0.1	1.45	0.01
HB-135(1).3	0.2	1.54	0.01
HB-135(1).4	0.5	1.60	0.01
HB-135(1).5	1.7	1.64	0.01
HB-135(1).6	5.2	1.61	0.02
HB-135(1).7	15.9	1.64	0.02
HB-135(1).8	44.5	1.64	0.03
HB-135(1).9	144.8	1.67	0.03
HB-135(1).10	523.9	1.69	0.03
HB-135(1).11	980.6	1.67	0.03
HB-135(1).12	1315.6	1.64	0.03
HB-135(1).13	4272.0	1.66	0.02
HB-135(1) $BaSO_4$	4272.0	1.67	0.01
HB-135(2) pre barite-addition	0.0	0.02	0.05
HB-135(2).1	0.0	1.50	0.00
HB-135(2).2	0.1	1.54	0.00
HB-135(2).3	0.2	1.59	0.01
HB-135(2).4	0.5	1.59	0.01
HB-135(2).5	1.6	1.61	0.01
HB-135(2).6	5.2	1.60	0.02
HB-135(2).7	15.7	1.63	0.02
HB-135(2).8	44.5	1.65	0.02
HB-135(2).9	144.8	1.65	0.03
HB-135(2) $BaSO_4$	144.8	1.65	0.02
MB-135(1) pre barite-addition	0.0	0.02	0.05
MB-135(1).1	0.0	0.47	0.01
MB-135(1).2	0.1	0.79	0.01
MB-135(1).3	0.2	1.09	0.01
MB-135(1).4	0.5	1.26	0.01
MB-135(1).5	1.6	1.32	0.01
MB-135(1).6	5.2	1.35	0.02
MB-135(1).7	17.0	1.36	0.02
MB-135(1).8	44.5	1.44	0.02
MB-135(1).9	144.0	1.47	0.03
MB-135(1).10	524.6	1.64	0.03
MB-135(1).11	981.6	1.64	0.03
MB-135(1).12	1316.7	1.65	0.03
MB-135(1).13	4272.1	1.65	0.03
MB-135(1) $BaSO_4$	4272.1	1.67	0.02
MB-135(2) pre barite-addition	0.0	0.02	0.05
MB-135(2).1	0.0	0.18	0.01
MB-135(2).2	0.1	0.61	0.01
MB-135(2).3	0.2	0.97	0.01
MB-135(2).4	0.6	1.15	0.01
MB-135(2).5	1.7	1.27	0.01
MB-135(2).6	5.2	1.34	0.02
MB-135(2).7	16.7	1.34	0.02
MB-135(2).8	44.4	1.36	0.02
MB-135(2).9	143.8	1.44	0.03
MB-135(2) $BaSO_4$	143.8	1.66	0.01

Table 2 cont.

Experiment.sample	Time (h)	$(^{137}Ba:^{135}Ba)_{fluid}$	±2SE
LB-135(1) pre barite-addition	0.0	0.02	0.05
LB-135(1).1	0.0	0.04	0.03
LB-135(1).2	0.1	0.09	0.02
LB-135(1).3	0.2	0.16	0.01
LB-135(1).4	0.6	0.27	0.01
LB-135(1).5	1.6	0.35	0.01
LB-135(1).6	5.2	0.41	0.01
LB-135(1).7	17.9	0.46	0.02
LB-135(1).8	44.6	0.53	0.02
LB-135(1).9	144.7	0.68	0.02
LB-135(1).10	526.0	1.24	0.02
LB-135(1).11	982.6	1.47	0.02
LB-135(1).12	1317.7	1.57	0.03
LB-135(1).13	4272.3	1.65	0.03
LB-135(1) BaSO4	4272.3	1.65	0.02
LB-135(2) pre barite-addition	0.0	0.02	0.05
LB-135(2).1	0.0	0.07	0.02
LB-135(2).2	0.1	0.12	0.01
LB-135(2).3	0.2	0.19	0.01
LB-135(2).4	0.6	0.29	0.01
LB-135(2).5	1.6	0.39	0.01
LB-135(2).6	5.2	0.46	0.01
LB-135(2).7	17.6	0.50	0.02
LB-135(2).8	44.5	0.55	0.02
LB-135(2) BaSO4	44.5	1.64	0.02
Barite (Puratronic, Alfa Aesar Lot #24177)		1.66	0.04

Table 3
Experimental data from experiments evaluation the temporal evolution of $\delta^{138}Ba$ over the course of experiments.

Experiment.Sample	Time (h)	[Ba] (nM)	±2SE	$\delta^{138}Ba$ (‰)	±2SE
HB-iso(1).1	1.44E-02	735	15	0.50	0.03
HB-iso(1).2	4.69E-02	536	11	0.45	0.04
HB-iso(1).3	6.36E-02	473	10	0.39	0.03
HB-iso(1).4	8.83E-02	472	9	0.45	0.03
HB-iso(1).5	2.13E-01	412	8	0.39	0.04
HB-iso(1).6	5.50E-01	485	10	0.21	0.04
HB-iso(1).7	1.63E+00	439	9	0.19	0.03
HB-iso(1).8	7.58E+00	188	4	0.19	0.04
HB-iso(1).9	2.27E+01	258	5	0.11	0.04
HB-iso(1).10	4.89E+01	179	4	0.13	0.04
HB-iso(1).11	1.41E+02	128	3	0.11	0.04
HB-iso(1).12	4.29E+02	118	2	0.07	0.04
HB-iso(2).1	1.11E-02	565	11	0.32	0.04
HB-iso(2).2	2.36E-02	700	14	0.50	0.03
HB-iso(2).3	3.56E-02	607	12	0.44	0.04
HB-iso(2).4	5.50E-02	575	12	0.46	0.03
HB-iso(2).5	7.14E-02	431	9	0.37	0.04
HB-iso(2).6	2.08E-01	357	7	0.39	0.03
HB-iso(2).7	5.53E-01	316	6	0.30	0.04
HB-iso(2).8	1.61E+00	236	5	0.31	0.03
HB-iso(2).9	2.20E+01	188	4	0.19	0.03
HB-iso(2).10	4.82E+01	201	4	0.17	0.04
HB-iso(2).11	1.40E+02	130	3	0.09	0.04
HB-iso(2) BaSO4	1.40E+02			-0.02	0.04
MB-iso(1).1	1.11E-02	437	9	0.33	0.03
MB-iso(1).2	2.39E-02	316	6	0.36	0.04
MB-iso(1).3	4.31E-02	532	11	0.32	0.03
MB-iso(1).4	5.53E-02	475	10	0.36	0.04
MB-iso(1).5	7.08E-02	460	9	0.37	0.04
MB-iso(1).6	2.28E-01	386	8	0.33	0.04
MB-iso(1).7	5.53E-01	304	6	0.33	0.04
MB-iso(1).8	2.22E+00	253	5	0.24	0.04
MB-iso(1).9	6.25E+00	195	4	0.24	0.04
MB-iso(1).10	2.14E+01	162	3	0.19	0.04
MB-iso(1).11	4.76E+01	140	3	0.14	0.04
MB-iso(1).12	1.39E+02	136	3	0.08	0.04
MB-iso(1).13	4.28E+02	119	2	0.08	0.05
MB-iso(1) BaSO4	4.28E+02				
MB-iso(2).1	1.03E-02	498	10	0.11	0.04
MB-iso(2).2	2.19E-02	396	8	0.28	0.04
MB-iso(2).3	3.42E-02	422	9	0.30	0.04
MB-iso(2).4	4.72E-02	452	9	0.31	0.04
MB-iso(2).5	6.81E-02	394	8	0.32	0.03
MB-iso(2).6	2.06E-01	348	7	0.40	0.04
MB-iso(2).7	6.04E-01	305	6	0.33	0.04
MB-iso(2).8	1.60E+00	247	5	0.28	0.03
MB-iso(2).9	5.65E+00	194	4	0.25	0.04
MB-iso(2).10	2.08E+01	155	3	0.23	0.04
MB-iso(2).11	4.69E+01	136	3	0.24	0.05
MB-iso(2).12	1.39E+02	135	3	0.20	0.03
MB-iso(2) BaSO4	1.39E+02			-0.05	0.03

Table 3 cont.

Experiment.Sample	Time (h)	[Ba] (nM)	±2SE	δ^{138}Ba (‰)	±2SE
LB-iso(1).1	1.00E-02	86	2	0.15	0.04
LB-iso(1).2	1.86E-02	143	3	0.18	0.04
LB-iso(1).3	2.64E-02	161	3	0.24	0.03
LB-iso(1).4	4.06E-02	177	4	0.20	0.04
LB-iso(1).5	7.00E-02	212	4	0.14	0.03
LB-iso(1).6	1.83E-01	246	5	0.18	0.03
LB-iso(1).7	5.63E-01	261	5	0.20	0.03
LB-iso(1).8	1.74E+00	230	5	0.25	0.04
LB-iso(1).9	4.37E+00	193	4	0.25	0.05
LB-iso(1).10	2.19E+01	164	3	0.25	0.04
LB-iso(1).11	4.67E+01	158	3	0.19	0.06
LB-iso(1).12	3.35E+02	119	2	0.09	0.04
LB-iso(2).1	9.17E-03	100	2	0.05	0.04
LB-iso(2).2	2.14E-02	109	2	0.08	0.04
LB-iso(2).3	3.19E-02	129	3	0.07	0.04
LB-iso(2).4	4.28E-02	141	3	-0.01	0.04
LB-iso(2).5	6.92E-02	155	3	0.10	0.04
LB-iso(2).6	1.94E-01	208	4	0.09	0.03
LB-iso(2).7	5.50E-01	215	4	0.15	0.04
LB-iso(2).8	1.61E+00	197	4	0.18	0.04
LB-iso(2).9	4.16E+00	183	4	0.12	0.04
LB-iso(2).10	2.17E+01	150	3	0.17	0.04
LB-iso(2).11	4.65E+01	149	3	0.20	0.05
LB-iso(2) BaSO4	4.65E+01			-0.02	0.03
Barite (Puratronic, Alfa Aesar Lot #24177)				-0.02	0.03
Initial fluid (artificial seawater)		26	0.8	0.10	0.03

Table 4

Modelled rates of ion exchange in experimental reactors. The rate of ion exchange is strongly dependent on the reactive surface area. Therefore, rates were calculated for BaSO4 grains with diameters of 0.5 and 5 µm to encompass the size range of BaSO4 in the synthetic barite used in experiments.

Experiment	L_{barite}	Equilibrium [Ba] (nmol L^{-1})	Rate of ion exchange, 0.5 µm (pmols m^{-2} s^{-1})	Rate of ion exchange, 5 µm (pmols m^{-2} s^{-1})
HB-135	0.999995	130 ± 9	4	41
MB-135	0.999950	120 ± 8	4	41
LB-135	0.999503	115 ± 8	4	41
			Rate of ion exchange (pmols m^{-2} s^{-1})	
Curti et al (2010)	0.990000		28	
	0.997442		567	
Torapava et al (2014)	0.999978		174	
	0.999957		694	
Brandt et al (2015)	Not reported		5	
	Not reported		4630	
Heberling et al (2018)	Not reported		110	
	Not reported		1400	

2.6 Supplement

Fig. S1 Temporal evolution of the counts per second (CPS) of Ba in ^{135}Ba-tracer experiments. Bulk mineral-fluid equilibrium in ^{135}Ba-tracer experiments is taken to be when at least 3 consecutive measurements of CPS fall within uncertainty of each other. This occurs after 44 h in HB-iso and MB-iso trials, and after 144 h in LB-iso(1). Experiment LB-135(2) was sacrificed before equilibrium was attained. Difference in equilibration time period is attributed to the difference in available reactive surface area, with the LB-135 trials containing the lowest mass of barite and therefore the least amount of surface area.

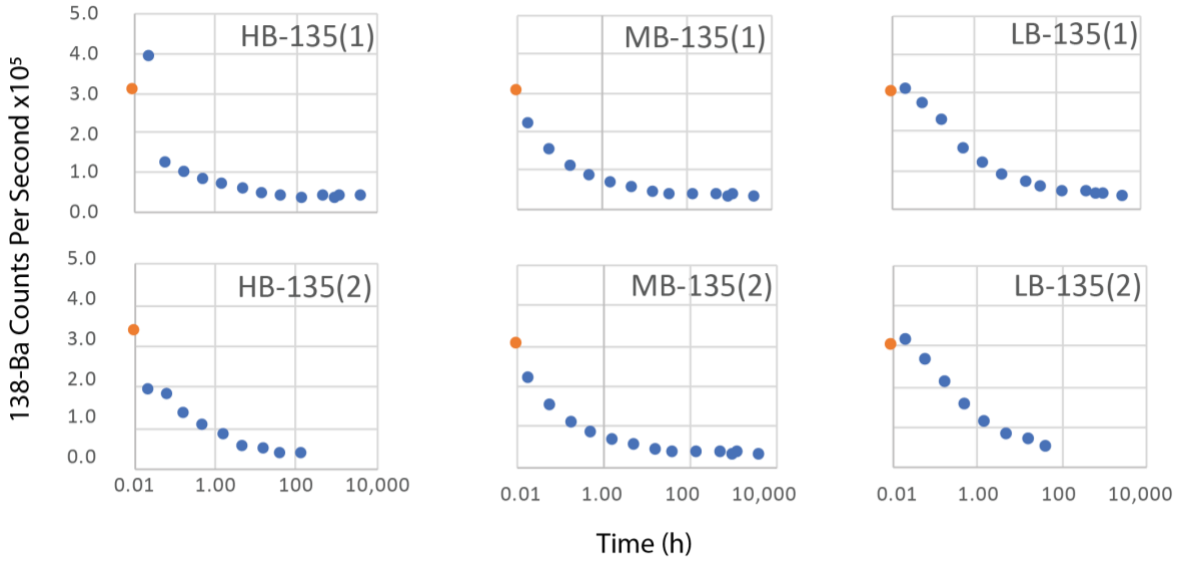

Fig. S2 Test to assess the degree of dissolved Ba adsorption to reactor walls. The reactor did not have any seed barite crystals and was sampled at the start and after 180 days. Initial and final dissolved [Ba] were found to be within uncertainty of each other, indicating that dissolved [Ba] was not significantly affected by bottle adsorption in these experiments.

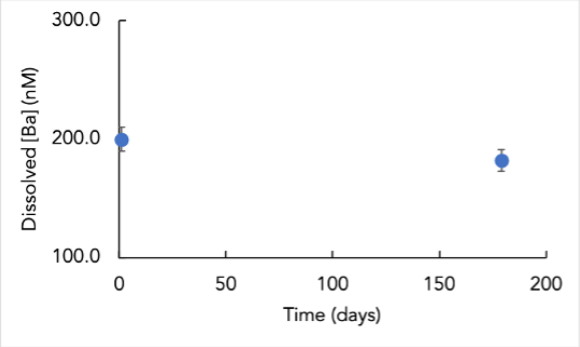

Time-dependent multi-phase reactor model describing ion exchange in Ba-$BaSO_4$ systems

Initial concentrations of barium of different isotopes

To model the laboratory experiments, we modified a time-dependent multi-phase reactor model that was developed previously (Sauer et al., 2021) but reduced the spatial domain to one grid. We included five dissolved species (^{134}Ba, ^{135}Ba, ^{137}Ba, ^{138}Ba and sulfate) as well as four solid species ($^{134}BaSO_4$, $^{135}BaSO_4$, $^{137}BaSO_4$ and $^{138}BaSO_4$) in the Reactor model. The parameters used in the Reactor model are given in Table 1. The two boundaries of the grid were set to prevent material exchange (i.e. Neumann boundary conditions with a zero flux). Such a setup represents a closed system and thus the processes that occur depend only on the initial conditions (Table 2).

Dissolved sulfate concentration ($[SO_4]$) was set to a constant value of 29 mM that does not change with time to conserve computing resources (i.e. $[SO_4]$ does not need to be calculated at each time step). The underlying assumption is that $BaSO_4$ dissolution/precipitation does not significantly affect $[SO_4]$, which is supported by the small changes in dissolved Ba concentration (up to ca. 600 nM, see below) and thus the corresponding insignificant decrease in $[SO_4]$ (ca. 0.002 %). The initial concentrations of the bulk dissolved Ba ($[Ba]=[^{134}Ba]+[^{135}Ba]+[^{137}Ba]+[^{138}Ba]$) were for each experiment according to measured laboratory conditions (Table 2). $[^{136}Ba]$ is excluded from the Reactor model assuming its concentration holds constant with time in all experiments. We used solar abundance for the different Ba isotopes when converting between isotopic ratios and bulk concentrations. Due to the exclusion of $[^{136}Ba]$, the solar abundances for the other Ba isotopes of interest are adjusted so that the sum equals to one. This is done as follow:

$$^{134,135,137,138}\chi = {}^{134,135,137,138}\chi \,/\, (^{134}\chi + {}^{135}\chi + {}^{137}\chi + {}^{138}\chi) \quad \text{(S1)}$$

The initial concentrations of the four different Ba isotopes were calculated based on their respective modified solar abundances ($^{134}\chi$, $^{135}\chi$, $^{137}\chi$, $^{138}\chi$) and the initial $^{134}Ba/^{138}Ba$ or $^{135}Ba/^{137}Ba$ molar ratios ($(^{138}Ba/^{134}Ba)_{f.ini}$ and $(^{137}Ba/^{135}Ba)_{f.ini}$) determined in the laboratory experiments as follow:

$$[^{134}Ba]_{f.ini} = [Ba]_{f.ini} \times (^{134}\chi + {}^{138}\chi) \,/\, [(^{138}Ba/^{134}Ba)_{f.ini} + 1] \quad \text{(S2)}$$

$$[^{135}Ba]_{f.ini} = [Ba]_{f.ini} \times (^{135}\chi + {}^{137}\chi) \,/\, [(^{135}Ba/^{137}Ba)_{f.ini} + 1] \quad \text{(S3)}$$

$$[^{137}Ba]_{f.ini} = [Ba]_{f.ini} \times (^{135}\chi + ^{137}\chi) - [^{135}Ba]_{f.ini} \quad \text{(S4)}$$

$$[^{138}Ba]_{f.ini} = [Ba]_{f.ini} \times (^{134}\chi + ^{138}\chi) - [^{134}Ba]_{f.ini} \quad \text{(S5)}$$

where $(^{137}Ba/^{135}Ba)_{f.ini}$ is measured for the laboratory experiment (0.02 mol/mol) and $(^{138}Ba/^{134}Ba)_{f.ini}$ is calculated as follow:

$$(^{138}Ba/^{134}Ba)_{f.ini} = (\delta^{138}Ba + 1) \times (^{138}\chi / ^{134}\chi) \quad \text{(S6)}$$

To account for the different leverages assigned to the laboratory experiments (i.e. molar ratios in $BaSO_4$ vs. solution, L_{barite}), the Reactor model calculates $BaSO_4$ seed content by considering [Ba], porosity (φ, or volume ratio between fluid and (fluid + barite)), and molecular weight (MW) of each Ba isotopes in bulk barite:

$$L_{barite} = \frac{\left(\left(\frac{[^{134}BaSO_4]}{MW_{134}}\right)+\left(\frac{[^{135}BaSO_4]}{MW_{135}}\right)+\left(\frac{[^{137}BaSO_4]}{MW_{137}}\right)+\left(\frac{[^{138}BaSO_4]}{MW_{138}}\right)\right)\times(1-\varphi)}{([^{134}Ba]+[^{135}Ba]+[^{137}Ba]+[^{138}Ba])\times\varphi} \quad \text{(S7)}$$

The initial $BaSO_4$ seed contents for the different isotopes are calculated by considering the density of $BaSO_4$ (ρ), the adjusted weight fraction for $BaSO_4$ of different isotopes (w_a), MW, and the isotopic ratios from the different laboratory experiments as follow:

$$[^{134}BaSO_4]_{ini} = \frac{\rho \times (^{134}w_a + ^{138}w_a)}{(MW_{138}/MW_{134}) \times (^{138}Ba/^{134}Ba)_{barite.ini} + 1} \quad \text{(S8)}$$

$$[^{135}BaSO_4]_{ini} = \frac{\rho \times (^{135}w_a + ^{137}w_a)}{(MW_{137}/MW_{135}) \times (^{137}Ba/^{135}Ba)_{barite.ini} + 1} \quad \text{(S9)}$$

$$[^{137}BaSO_4]_{ini} = \rho \times (^{135}w_a + ^{137}w_a) - [^{135}BaSO_4]_{ini} \quad \text{(S10)}$$

$$[^{138}BaSO_4]_{ini} = \rho \times (^{134}w_a + ^{138}w_a) - [^{134}BaSO_4]_{ini} \quad \text{(S11)}$$

The adjusted weight fraction, w_a, is calculated from the adjusted molar fraction of each isotope from the solar abundance:

$$^{134,135,137,138}W_a = \frac{MW_{134,135,137,138} \times {}^{134,135,137,138}\chi}{(MW_{134} \times {}^{134,}\chi)+(MW_{135} \times {}^{1345}\chi)+(MW_{137} \times {}^{137}\chi)+(MW_{138} \times {}^{138}\chi)} \quad \text{(S12)}$$

The initial isotopic ratio of $^{138}Ba/^{134}Ba$ is calculated with $\delta^{138}Ba$ and the solar molar ratio of the two isotopes. For $^{137}Ba/^{135}Ba$ ratio, the value was determined for the laboratory experiment to be 1.74 mol/mol.

Numerical scheme

Detailed formulation of the model has been introduced in Sauer et al. (2021). In the current Reactor model, we simulated this closed system for 0.01 years, or 87.6 hours. Such a short modelling duration, as compared to the time span for the laboratory experiments (ca. 1000 hours), is sufficient to capture most of the changes in the experiments. A total of four million discretization were assigned for the entire modelling time. During each temporal discretization, the reaction rates, saturation, solid-to-solution ratios (as represent by porosity) were calculated based on the concentrations from the previous time step. Such an explicit numerical scheme is known to be advantageous for Reactor model implementation but may suffer from numerical instability if the time discretization is not sufficiently small. Repetitive trials were made to find an optimal value for the current Reactor model setup. We observed that the reaction rates, and thus the choices of kinetic constants, are to some degree depends on the size of discretization, likely due to the close coupling and intense feedback between the dissolution and precipitation processes. In other words, the magnitude of the Reactor model-derived reaction rates (as well as the kinetic constants) are subject to changes if a different number of discretization is adopted. The four million discretization is determined based on the produced changes in the modelled Ba concentrations that show changes of at most 10 nM, or comparable to the analytical error. We argue that a finer discretization is not necessary as the Reactor model will produce unconstrained outcomes given the analytical uncertainties. Despite the issue, the general trend and changes in the Reactor model-derived $^{137}Ba/^{135}Ba$ ratios remain, as well as for the saturation and leverage calculated.

Table S1
Parameter descriptions and values for the Reactor model describing Ba ion exchange which are not constrained by experimental values.

Parameter	Abbreviation	Value	Unit	Reference/note
Molecular weight, $^{134}BaSO_4$	MW_{134}	229.9645	g/mol	
Molecular weight, $^{135}BaSO_4$	MW_{135}	230.9657	g/mol	
Molecular weight, $^{137}BaSO_4$	MW_{137}	232.9658	g/mol	
Molecular weight, $^{138}BaSO_4$	MW_{138}	233.9652	g/mol	
Barite density	ρ	4.48×10^6	g/m^3	
Porosity	$\varphi = V_f/(V_s+V_f)$	110.44	m^3/m^3	
Fluid [Ba] at equilibrium	$[Ba]_{eq}$	130	nmol L^{-1}	
Fluid [Ba]	[Ba]		nmol L^{-1}	
Fluid $[SO_4^{2-}]$	$[SO_4^{2-}]$	29	mmol L^{-1}	Constant for all trials and time
Barite solubility product	K_{sp}	$10^{-8.46}$	$(mol/L)^2$	
Barite saturation index	$\Omega = [Ba]\times[SO_4^{2-}]/K_{sp}$			
Molar ratio, ^{134}Ba	$^{134}\chi$	0.02417	mol/mol	Solar abundance
Molar ratio, ^{135}Ba	$^{135}\chi$	0.06592	mol/mol	Solar abundance
Molar ratio, ^{137}Ba	$^{137}\chi$	0.07854	mol/mol	Solar abundance
Molar ratio, ^{138}Ba	$^{138}\chi$	0.71698	mol/mol	Solar abundance
$^{138}Ba/^{134}Ba$	$^{138}\chi / {}^{134}\chi$	29.6640	mol/mol	Solar abundance
$^{137}Ba/^{135}Ba$	$^{137}\chi / {}^{135}\chi$	1.7039	mol/mol	Solar abundance
Weight fraction in bulk barite, $^{134}BaSO_4$	$^{134}w_a$	0.0259	g/g	Modified Solar abundance
Weight fraction in bulk barite, $^{135}BaSO_4$	$^{135}w_a$	0.0709	g/g	Modified Solar abundance
Weight fraction in bulk barite, $^{137}BaSO_4$	$^{137}w_a$	0.1219	g/g	Modified Solar abundance
Weight fraction in bulk barite, $^{138}BaSO_4$	$^{138}w_a$	0.7813	g/g	Solar abundance
Fluid $\delta^{138}Ba$	$\delta^{138}Ba_f$		‰	NIST SRM 3104a
Fluid $^{137}Ba/^{135}Ba$	$(^{137}Ba/^{135}Ba)_f$		mol/mol	
Fluid $[^{134}Ba]$	$[^{134}Ba]_f$		µM	
Fluid $[^{135}Ba]$	$[^{135}Ba]_f$		µM	
Fluid $[^{137}Ba]$	$[^{137}Ba]_f$		µM	
Fluid $[^{138}Ba]$	$[^{138}Ba]_f$		µM	
Barite seed $\delta^{138}Ba$	$\delta^{138}Ba_s$		‰	NIST
Barite content	$[BaSO_4]$		g/m^3	
Leverage	$L_{barite}=[BaSO_4]/([Ba]\times\varphi)$		mol $BaSO_4$/mol Ba	
Molar ratio dependency	mrd	-0.8	unitless	modelling
	$^{134/138}\beta_{BP}$	1.0007	yr/yr	modelling
	$^{134/138}\beta_{BD}$	1.0006	yr/yr	modelling
k_{BP}	0.25		1/yr	modelling
k_{BD}	0.25		1/yr	modelling

Table S2

Parameter descriptions and values for the Reactor model describing Ba ion exchange which are constrained by experimental values from ^{135}Ba-tracer and stable Ba isotope experiments.

Parameter	**abbreviation**	**Initial Value**	**Unit**	**Reference/note**
Initial fluid [Ba]	$[Ba]_{ini}$	760	nmol L^{-1}	
Initial fluid [SO_4^{2-}]	$[SO_4^{2-}]_{ini}$		nmol L^{-1}	A constant for all trials and time
Initial fluid δ^{138}Ba	$\delta^{138}Ba_{f.ini}$	0.495	‰	NIST SRM 3104a
Initial fluid ^{137}Ba/^{135}Ba	$(^{137}Ba/^{135}Ba)_{f.ini}$	0.0058	mol/mol	
Initial fluid [^{134}Ba]	$[^{134}Ba]_{f.ini}$	18.36	nmol L^{-1}	
Initial fluid [^{135}Ba]	$[^{135}Ba]_{f.ini}$	134.68	nmol L^{-1}	
Initial fluid [^{137}Ba]	$[^{137}Ba]_{f.ini}$	0.78608	nmol L^{-1}	
Initial fluid [^{138}Ba]	$[^{138}Ba]_{f.ini}$	544.91	nmol L^{-1}	
Initial $BaSO_4$ seed δ^{138}Ba	$\delta^{138}Ba_{s.ini}$	0.03	‰	NIST SRM 3104a
Initial $BaSO_4$ content	$[BaSO_4]_{ini}$	0	g/m^3	
Initial leverage	$L_{barite,ini}=[BaSO_4]_{ini}/([Ba]_{ini}\times\varphi)$		mol-$BaSO_4$/mol-Ba	

Fig. S3 Sensitivity test of the rate dissipation term ($^{134/138}\beta_{BP}$) in the correction function used in Eq. (4) in the main text. A higher value assigned results in a faster decay in rate (and thus shorter rapid exchange phase). A number of experimental studies observe slowing rates of ion exchange in mineral-fluid systems over time ((Mozeto et al., 1984; Rea et al., 1994; Curti et al., 2005; Bosbach et al., 2010; Avrahamov et al., 2013; Lestini et al., 2013)), with the findings of Bosbach et al., (2010) specifically observing this slowing in Ba-$BaSO_4$ systems. Based on this, the use of $^{134/138}\beta_{BP}$ is reasonable.

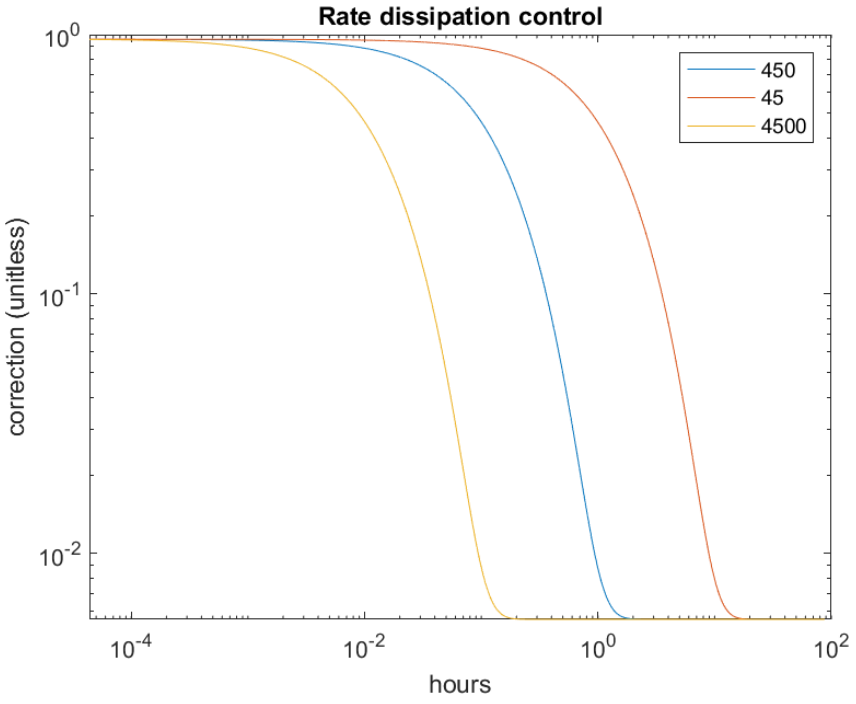

Chapter 3: Barium isotope signatures of diagenesis in barite and associated pore fluids in the Equatorial Pacific

Abstract

The isotopic composition of barium (Ba) in the mineral barite ($BaSO_4$) has recently been used to constrain Ba-based paleoproxies used to reconstruct seawater isotopic compositions, impacts of microbial sulfur cycling, and marine export productivity over interglacial timescales. Therefore, it is critical to constrain processes altering the chemical and isotopic signature of Ba in $BaSO_4$ in the environmental record. To that end, we analyze pore fluids and co-located $BaSO_4$ in sediments from the Equatorial Pacific to characterize and quantify the effects of ion exchange, a morphology-preserving process which occurs under oxic, sulfate-replete conditions, in natural environments. Our findings suggest that Ba isotopic compositions of sedimented pelagic $BaSO_4$ are not conservatively transferred to the fluid phase during $BaSO_4$ dissolution ($\Delta^{138}Ba_{barite\text{-}dBa}$ = +0.15 ‰) and evolve toward isotopic equilibrium in the presence of an aqueous phase, even when at bulk chemical equilibrium. The combined effect of $BaSO_4$ dissolution and precipitation leads to an observed $\Delta^{138}Ba_{barite\text{-}dBa}$ = -0.17 ‰ when the system achieves isotopic equilibrium. The degree to which the isotopic composition of $BaSO_4$ is altered depends on the proportion of Ba held in the solid phase compared to that in the fluid and the degree to which the fluid phase is out of isotopic equilibrium with respect to $BaSO_4$. In environmental records used for the reconstruction of carbon export, where the proportion of $BaSO_4$ in the sediments is high, the isotopic composition of $BaSO_4$ is not altered significantly. However, care must be taken in sediments with lower proportions of Ba held in the solid phase and regions where flowing natural fluids may significantly increase the effective leverage of Ba in the fluid phase. Generally, when interpreting the isotopic composition of Ba in $BaSO_4$ in sediments with poor constraints on the proportion of Ba in $BaSO_4$ and pore fluid or the magnitude of fluid flow, variations of < 0.17 ‰ should be interpreted with caution as they fall within the range of variation allowable solely by ion exchange.

3.3 Introduction

The chemistry of barite ($BaSO_4$) in pelagic sediments has long been used to reconstruct seawater isotopic compositions and impacts of microbial sulfur cycling (Paytan et al., 2004, 2002, 1993; Turchyn and Schrag, 2006; 2004). In addition to its chemistry, the accumulation rate of $BaSO_4$ in pelagic sediments offers a record of marine export productivity over centennial to millennial geological timescales (Dymond et al., 1992; Eagle et al., 2003; Paytan et al., 1996b). Recently, the analytical ability to measure barium isotopes ($\delta^{138}Ba$) in the marine water column and sediments has added a new dimension of geochemical interpretation: refinement of the global marine barium (Ba) cycle (Hsieh and Henderson, 2017; Crockford et al., 2019; Hsieh et al., 2021), tracing of deep water mass cycling (Bates et al., 2017; Horner et al., 2017; Hemsing et al., 2018; Geyman et al., 2019), and reconstructions of global carbon cycling over the past >50 million years (Bridgestock et al., 2019). These studies tacitly assume that the chemical composition, particularly the isotopic composition of Ba, of sedimented $BaSO_4$ accurately preserves the signature of the surrounding ancient ocean seawater at the time of formation. One of the primary ways in which this assumption may be violated is through diagenesis – the chemical changes which occur after deposition and burial of the mineral on the seafloor.

Barite diagenesis under anoxic, suboxic, and sulfidic conditions is well studied (Rutsch et al., 1995; Paytan and Kastner, 1996; Dean et al., 1997; Nürnberg et al., 1997; McManus et al., 1998; Gingele et al., 1999), and morphological and geochemical criteria exist to screen sedimentary $BaSO_4$ for diagenetic alteration of this type (e.g. Griffith and Paytan, 2012; Paytan et al., 1993). However, chemical alteration of $BaSO_4$ has also been observed under oxic, sulfate-replete conditions without visible changes to the crystal morphology (Gorski and Fantle, 2017; Klinkenberg et al., 2014) Chapter 2). In these cases, alteration occurs through surface-mediated processes which allow ions to exchange between the mineral and a surrounding fluid without affecting the morphology of the mineral (Bosbach et al., 2010; Curti et al., 2010; Vinograd et al., 2013; Torapava et al., 2014; Klinkenberg et al., 2014; Brandt et al., 2015). Furthermore, the isotopic composition of Ba in synthetic $BaSO_4$ has recently been shown to be susceptible to alteration through surface-mediated ion exchange under oxic, sulfate-replete conditions relevant to the marine environment (see Chapter 2). The effects of ion-exchange-mediated diagenesis on Ba isotopes in $BaSO_4$ in oxic, sulfate-replete pelagic sediments are currently unknown.

Here, we investigate ion-exchange-mediated diagenetic alteration of Ba isotopes in modern marine sediments using δ^{138}Ba values in the water column, sedimented pelagic $BaSO_4$, and associated pore fluids in samples from the Equatorial Pacific. These sediments offer an excellent opportunity to evaluate the role of ion-exchange-mediated diagenesis, as sedimentary pelagic $BaSO_4$ and pore fluids remain in contact over millennia (Murray et al., 1995). We first report experimental results which identify the presence and rate of ion exchange between sedimented pelagic $BaSO_4$ and seawater using an isotope tracer. The rates of ion exchange quantified from the experimental study were then used to interpret δ^{138}Ba of pore fluids and $BaSO_4$ in sediment cores from the Equatorial Pacific. A two-box model of pore fluid-$BaSO_4$ interactions in the sediments imply significant fluxes of Ba ions between the mineral and fluid, even in scenarios with pore fluids near $BaSO_4$ saturation. The rates of ion exchange and rate constants of $BaSO_4$ precipitation derived through the model agree well with prior literature. Taken together, these findings suggest that early diagenesis of marine $BaSO_4$ is ongoing in sediments of the Equatorial Pacific. Furthermore, variability in pore fluid δ^{138}Ba can be attributed largely to the effects of ion exchange with co-located pelagic $BaSO_4$. This work demonstrates the importance of internal cycling of Ba ions between pore fluids and $BaSO_4$, describes the associated magnitude of isotopic change, and provide constraints on the potential impact of these processes on the isotopic composition of Ba recorded by $BaSO_4$.

3.2 Methods

3.2.1 Sampling location and procedures

Sediment and pore fluids from the Joint Global Ocean Flux Study (JGOFS) Equatorial Pacific (EqPac) Leg TT013 were analyzed for Ba isotopes in this study. A full description of the sampling protocols may be found in Paytan and Kastner (1996). Briefly, sediments were collected using a multi-corer and all cores had a well-preserved sediment-water interface. Sub-cores were transferred to a 2 °C cold room immediately upon arrival on board and were sectioned in a nitrogen atmosphere glove box. Pore fluids were extracted by centrifugation and filtered to 0.45 μm through a pre-washed Nucleopore filter, then acidified to pH 2 with nitric acid. The cores are oxic and sulfate replete over the depth sampled (Paytan and Kastner, 1996). Water column samples come

from the ProteOMZ EqPac cruise (FK160115), full sampling procedures followed the GEOTRACES trace metal sampling protocol (Cutter et al., 2017). Briefly, samples were collected into pre-washed high-density polyethylene bottles in a clean glove box, filtered to 0.45 µm, and acidified to pH 2 using hydrochloric acid. Samples were stored for three years prior to analysis. Sample locations and identifiers are found in Table 1.

3.2.2 Isotope-tracer experiments for the identification of ion exchange

A matrix experiment was carried out to assess the role of ion exchange between seawater and $BaSO_4$. Artificial seawater (ASW) and filtered seawater (FSW) were used to assess if barium ion exchange occurred in filtered natural seawater, and if it differed from ion exchange observed in ASW. Differences in ion exchange related to $BaSO_4$ were interrogated using synthetic $BaSO_4$ and sedimented $BaSO_4$ from the Equatorial Pacific. Experimental setups, seawater characteristics, and $BaSO_4$ characteristics are given in Table 2.

Experiments using ^{136}Ba as a tracer of ion exchange were carried out following the protocol used in Chapter 2. The rate of exchange between $BaSO_4$ and a fluid was quantified using ^{136}Ba (Oak Ridge National Laboratory). Any ion exchange between $BaSO_4$, possessing natural Ba isotope abundances (i.e., ^{138}Ba:$^{136}Ba \approx 9.1$; de Laeter et al., 2003), and dissolved Ba, with $(^{138}Ba:^{136}Ba)_{fluid} = 0.35 \pm 0.03$ (± 2SE, n = 4), would drive changes in $(^{138}Ba:^{136}Ba)_{fluid}$. In the isotope tracer experiments, the amount of ^{136}Ba spike added was adjusted based on *T*, *S*, and preexisting Ba in the fluid to achieve an initial Ω_{barite} of 1.3 —calculated using the aqueous geochemical modelling program PHREEQC (Parkhurst and Appelo, 2013). Tracer experiments were initiated at slightly super-saturated conditions of Ω_{barite} of 1.3 to prevent dissolution of barite and enable detection of ion exchange only. Initial conditions for the isotope-tracer experiments are shown in Table 2. Aliquots of solution were sampled over the experimental period and filtered to 0.22 µm for analysis of $(^{138}Ba:^{136}Ba)_{fluid}$.

The blank reactor used to assess any Ba adsorption onto reactor walls is discussed in Chapter 2. This reactor was run under the same conditions as the isotope-tracer experiments, with two differences: the dissolved Ba came from a synthetic $BaCl_2 \cdot H_2O$ solution and no $BaSO_4$ was added so that changes in [Ba] could be determined for the blank reactor. The blank reactor was sampled at the initiation and end of the experimental period.

3.2.3 Measurement of ($^{138}Ba/^{136}Ba)_{fluid}$

For each timepoint, a 2mL aliquot was subsampled, immediately filtering to a cutoff of 0.22 μm, and the resultant solution collected. A second aliquot was subsampled from each of the filtered samples, diluted to 1900 μL with 2 % HNO_3, and spiked with indium (In)—an internal standard added to all samples—to achieve a final [In] of 1 ng mL^{-1}. All samples were diluted and measured at a salinity of 1.75 to minimize non-spectral matrix effects. Filtered samples were analyzed for ^{138}Ba:^{136}Ba on a reverse quadrupole ICP-MS (iCAP-RQ, Thermo Fisher Scientific).

3.2.4 Barite dissolution

Barite samples were dissolved through an alkaline dissolution in PFA vials by addition of 1 M Na_2CO_3 solution to form $(Ba,Ca)CO_3$ as in Breit et al. (1985) Briefly, Na_2CO_3 was added to achieve $BaSO_4$:Na_2CO_3 of 1:10 by mass, with 18.2 MΩ water was added such that there was 10 mg of $BaSO_4$ per 2 mL of solution. Following reagent addition, samples were sonicated for 60 minutes at room temperature and then heated at 80 ℃ for ≥16 h. After cooling, the fluid was decanted. Two further rounds of Na_2CO_3 addition, sonication, heating, and decantation were carried out. Following the third decanting, samples were rinsed with 18.2 MΩ water and the remaining solid, $BaCO_3$, was dissolved with 2 M HCl.

3.2.5 Ba isotope measurements

Pore fluid, sediment, and water column samples were prepared for Ba-isotopic analysis following the procedure outlined in Bates et al. (2017) and reported as deviations in the $^{138}Ba/^{134}Ba$ ratio in a sample relative to a standard (NIST SRM 3104a, hereafter 'NIST'):

$$\delta^{138}Ba = [(^{138}Ba/^{134}Ba)_{sample} /(^{138}Ba/^{134}Ba)_{NIST} - 1], \quad (1)$$

expressed in ‰. Briefly, dissolved samples were equilibrated with a ^{135}Ba–^{136}Ba double spike of known concentration to achieve a spike- to sample-derived [Ba] ratio between 1–2. Ba was pre-

concentrated through (Ba,Ca)CO_3 co-precipitation by drop-wise addition of 1 M Na_2CO_3. Samples were then dissolved in 250 µL of 2 M HCl in preparation for liquid ion-exchange chromatography. Ba was isolated by passing samples twice through 500 µL of AG 50W-X8 (200–400 mesh) cation-exchange resin (Bio-Rad), following the purification protocol described by Horner et al. (2015). Purified Ba was analyzed for Ba isotopes using a ThermoFinnigan Neptune multi-collector inductively coupled plasma mass spectrometer. All samples were analyzed at least of two times. Sample isotopic compositions were calculated using the three-dimensional geometric interpretation of the double-spike problem (Siebert et al., 2001) with additional processing for isobaric corrections (^{136}Xe and ^{136}Ce on ^{136}Ba, ^{138}Ce and ^{138}La on ^{138}Ba; Bates et al. (2017)). Ba isotope compositions were calculated relative NIST by standard-sample bracketing. Four procedural blanks constrain Ba contributions associated with sample preparation were found to range from 305 to 489 pg. Four instrument blanks were found to range from 14 to 301 pg. The procedural blanks are below the long-term average procedural blank (692 pg), the contribution of the highest blank to the sample with the lowest [Ba] was < 3 %. Given the low blank contribution and poor constraints on the true Ba-isotopic blank value, no blank correction was applied to the Ba-isotopic data. Sample uncertainties are reported as either a long-term measurement of uncertainty (±2 SD about the mean; ± 0.03 ‰, Horner et al. (2015) or pooled 2 SE (standard error) from the four sample analyses, whichever was found to be greater.

Accuracy of $BaSO_4$ and artificial seawater measurements was monitored by processing two internal reference materials alongside samples: an Alfa Aesar $BaSO_4$ powder and GEOTRACES SAFe D1 (northeast Pacific seawater, 1,000 m). We found that the $BaSO_4$ and SAFe D1 possessed a δ^{138}Ba value of –0.02 ± 0.03 ‰ and +0.33 ± 0.04 ‰, in agreement with previous measurements of –0.04 ± 0.07 ‰ (±2SE, n = 7; Tristan Horner pers. comm.) and +0.31 ± 0.03 ‰ (Cao et al., 2020; Geyman et al., 2019; Hsieh and Henderson, 2017) respectively.

3.3 Results

3.3.1 Isotope-tracer experiments to assess ion exchange

Initial (^{138}Ba:^{136}Ba)$_{fluid}$ in experiments using ^{136}Ba as a tracer to assess ion exchange was 0.32 ± 0.002 for trials with ASW (n = 3, ±2SE) and 0.36 ± 0.004 for trials with FSW (n = 3, ±2SE).

The $(^{138}Ba:^{136}Ba)_{solid}$ of the original synthetic $BaSO_4$ grains was 9.13 ± 0.3 (n = 3, ± 2SE). Similarly, the pelagic $BaSO_4$ have $(^{138}Ba:^{136}Ba)_{solid}$ = 9.13 ± 0.01 (n = 25, ± 2SE). Sorption of barium to vessel walls was assessed using a blank trial with no $BaSO_4$ in the reactor. The invariant concentration of barium in the blank trial over the course of 180 days indicates no significant sorption to vessel walls (Fig. S1; also discussed in Chapter 2). The $(^{138}Ba:^{136}Ba)_{fluid}$ data for the four trials are shown in Fig. 1. Barium in experimental fluids was monitored by measurement of the blank-corrected counts per second (CPS) at each timepoint. While [Ba] cannot be calculated using our method because of the highly varying proportions of 136-Ba and 138-Ba, CPS is a useful tool to assess potential changes in $(^{138}Ba:^{136}Ba)_{fluid}$ due to any initial dissolution of $BaSO_4$ and to monitor the approach of the system to chemical equilibrium. Chemical equilibrium is taken to occur when at least 3 consecutive measurements of CPS fall within analytical uncertainty of each other. In the ASW2, FSW1, and FSW3 trials, the system started and remained at chemical equilibrium for the duration of the experimental interval (Fig. S2). The ASW1 trial reached chemical equilibrium after 2.7 hours following an initial increase in CPS. After reaching chemical equilibrium, the $(^{138}Ba:^{136}Ba)_{fluid}$ of all trials continued to evolve toward $(^{138}Ba:^{136}Ba)_{solid}$ (Fig. 1). The reactive fluid of the ASW1 and ASW2 trials progressed significantly toward $(^{138}Ba:^{136}Ba)_{solid}$, reaching $(^{138}Ba:^{136}Ba)_{fluid}$ values of 6.34 and 8.44 after 174 days, respectively. Reactive fluids in the FSW1 and FSW2 trials showed significantly smaller changes in $(^{138}Ba:^{136}Ba)_{fluid}$ over the experimental period, reaching values of 1.89 and 1.34, respectively. Barium is largely held within the $BaSO_4$ pool in these trials. This is quantified as the L_{barite} of the system, where L_{barite} refers to the proportion of Ba in the solid phase. Due to the high L_{barite} of all trials, the fluid phase had little leverage to alter $(^{138}Ba:^{136}Ba)_{solid}$ (Table 2). Mass-balance calculations indicate that complete uptake of ^{136}Ba into $BaSO_4$ can impart a maximum possible change in $(^{138}Ba:^{136}Ba)_{solid}$ of 0.04. As this is the same magnitude as analytical uncertainty, $(^{138}Ba:^{136}Ba)_{solid}$ was not measured over the course of the experiment.

Environmental data

3.3.2 $\delta^{138}Ba$ in the water column of the Equatorial Pacific

New seawater profiles in the Central Equatorial Pacific show the characteristic vertical fractionation of $[Ba]_{SW}$, with low values in surface waters (~30 nM) and higher value at depth (~140 nM; Fig. 2A). Between depths of ~200 m to 4000 m at both 4 °N and the equator, $[Ba]_{SW}$ generally increases. The shallow cast at the 4 °S site exhibits the same increase to 1000 m depth. In all locations, $[Ba]_{SW}$ is constant in the surface waters above ~200 m, with $[Ba]_{SW}$ = 34 ± 1 nM (n = 17, ±2SE). The value of $\delta^{138}Ba$ in seawater generally reflect $[Ba]_{SW}$, becoming progressively lighter as $[Ba]_{SW}$ increases, in good agreement with previously published profiles (Fig. 2B; (Horner et al., 2015, 2017; Hsieh and Henderson, 2017; Bridgestock et al., 2018; Hemsing et al., 2018; Crockford et al., 2019; Geyman et al., 2019; Cao et al., 2020) and falling along the global mixing line. Importantly, the extremely oligotrophic gyres have some of the lowest surface $[Ba]_{SW}$ measured to date, extending the mixing line and potentially showing some curvature (Fig. 2C).

3.3.3 $\delta^{138}Ba$ in the sediments and pore fluids of the Equatorial Pacific

The $\delta^{138}Ba$ of $BaSO_4$ in Equatorial Pacific sediments ($\delta^{138}BaSO_4$) are found to be consistent between sites, with an average value of +0.09 ± 0.03 ‰ (n = 32, ±2SE; Fig. 3). These values are similar to those previously measured for particulate Ba in the water column (Horner et al., 2017; Cao et al., 2020) and those predicted for pelagic $BaSO_4$ in the sediments (Bridgestock et al., 2018). Barite in the Equatorial Pacific sediments are offset from surface waters (0 – 200 m) by $\Delta^{138}Ba_{barite\text{-}dBa}$ = –0.51 ± 0.03 ‰, where $\Delta^{138}Ba_{barite\text{-}dBa} = \delta^{138}BaSO_4 - \delta^{138}Ba_{dBa}$ (n = 32, ±2SE). This value is in line with the magnitude of fractionation previously observed between pelagic $BaSO_4$ and dissolved Ba in marine environments (Bates et al., 2017; Hsieh and Henderson, 2017; Horner et al., 2017; Bridgestock et al., 2018; Crockford et al., 2019; Cao et al., 2020).

In the sediments, pore fluid [Ba] ($[Ba]_{PW}$) exhibits a maximum (~300-400 nM) at the sediment surface before decreasing to a relatively constant value past 1.5 cm downcore (~240 nM; Fig. 4). $[Ba]_{PW}$ measured in these cores agree with previously measured $[Ba]_{PW}$ for the same samples (Paytan and Kastner, 1996). The $[Ba]_{PW}$ maxima observed at the sediment-water interface is the result of the dissolution of more soluble phases holding Ba, likely organic matter (Paytan and Kastner, 1996; McManus et al., 1998), before approaching the $BaSO_4$ saturation value at which the pore fluid is in chemical equilibrium with pelagic $BaSO_4$ (Paytan and Kastner, 1996). At the study sites, pore fluid $\delta^{138}Ba$ ($\delta^{138}Ba_{PW}$) ranges between +0.18 and +0.34 ‰ and does not

display consistent trends between cores (Fig. 5). $\delta^{138}Ba_{PW}$ at the 5 °S site varies greatly in the top 10 cm of sediment, while values are relatively consistent downcore at the 4 °N site. At the equator, $\delta^{138}Ba_{PW}$ is variable in the top 10 cm before decreasing to 20 cm. Bottom waters measured 0.5 to 5 m above the sediment surface range were found to be +0.25 ± 0.03 ‰, +0.19 ± 0.03 ‰, and +0.24 ± 0.03 ‰ for the 5 °S, equator, and 4 °N site, respectively (Fig. 5). These values were within range of the $\delta^{138}Ba_{PW}$ at 4 °N and slightly lower than $\delta^{138}Ba_{PW}$ at 5 °S and the equator.

3.4 Discussion

The barium isotope distribution in the oceanic water column is largely set by $BaSO_4$ formation in surface waters, non-fractionating $BaSO_4$ regeneration at depth, and conservative mixing of these signatures along the global overturning current (Fig. 2C; Horner and Crockford, 2021). Assuming the same processes govern the relationship between $[Ba]_{PW}$ and $\delta^{138}Ba_{PW}$ near chemical equilibrium, we would expect $BaSO_4$ dissolution in the sediments to create pore fluid Ba with $\delta^{138}Ba_{PW} \approx \delta^{138}BaSO_4$ across a range of $[Ba]_{PW}$ in the oxic sediments studied here (Murray and Grundmanis, 1980; Paytan and Kastner, 1996). However, pore fluid data from the Equatorial Pacific are offset from to the global mixing line for $\delta^{138}Ba$, indicating that processes affect $\delta^{138}Ba_{PW}$ that do not significantly impact $\delta^{138}Ba$ in the water column (Fig. 2C, inset). In addition to falling off the mixing line, $\delta^{138}Ba_{PW}$ appears to have a stochastic relationship with $1/[Ba]_{PW}$ and is more enriched in the heavy Ba isotopes than expected by non-fractionating $BaSO_4$ dissolution, with an average offset from co-located $BaSO_4$ by $\Delta^{138}Ba_{barite\text{-}dBa} = -0.16 \pm 0.04$ ‰ (n = 11, ±2SE). We investigated the possibility that bottom water intrusion might explain the observed trends. Bottom water (BW) collected with the cores indicate $\delta^{138}Ba_{BW}$ values are enriched in the light isotope compared to $\delta^{138}Ba_{PW}$ at the sediment water interface (Fig. 3). As pore fluids are more enriched in the heavy isotope than expected, a light isotopic source of Ba from BW cannot account for the observed trends. This observation, combined with benthic chamber data indicating net efflux of pore fluid from these sediments (McManus et al., 1998), suggests that bottom water intrusion cannot account for the observed variations in $\delta^{138}Ba_{PW}$. Having ruled out the influence of bottom water intrusion, it is evident that other processes affect pore fluids and produce the consistent offset observed between $\delta^{138}Ba_{PW}$ and $\delta^{138}BaSO_4$. It may be that organic matter dissolution at the sediment water interface contributes to the departure from the global mixing line.

Organic matter complexation of dissolved Ba^{2+} is known to occur, although any associated isotopic fractionation of Ba has not yet been quantified (Martinez-Ruiz et al., 2018, 2019, 2020). While I do not evaluate the contribution of organic matter due to a lack of sample material, I will evaluate the role of other processes potentially affecting the pore fluids. Chapter 2 showed that Ba ion exchange between synthetic $BaSO_4$ and dissolved Ba fractionates Ba isotopes with a observed magnitude of -0.10 ± 0.05 ‰, similar to the offset observed between pelagic $BaSO_4$ and pore fluids in the Equatorial Pacific. Given this, I characterize ion exchange between pelagic $BaSO_4$ and FSW, model the rate of ion exchange in experimental settings, and evaluate the role of this process in Equatorial marine sediments.

3.4.1 Identification of ion exchange

We assessed the impact of Ba ion exchange between $BaSO_4$ and dissolved Ba using stable isotope tracer experiments. To accurately interpret variations in $(^{138}Ba:^{136}Ba)_{fluid}$ with respect to ion exchange, we first evaluate two unrelated processes which may influence $(^{138}Ba:^{136}Ba)_{fluid}$: Ba loss to adsorption onto reactor walls and net barite dissolution. We assume that any net precipitation has a negligible effect on $(^{138}Ba:^{136}Ba)_{fluid}$, as the magnitude of change in $(^{138}Ba:^{136}Ba)_{fluid}$ is well beyond what is possible by stable isotope fractionation for Ba. Dissolved [Ba] remained constant over a 180 day interval in a blank reactor with no solid $BaSO_4$, implying that adsorption is not a major driver of fluid fluctuations (Fig. S1; discussed further in Chapter 2). Minimal adsorption of Ba to reactor walls agrees with the findings Heberling et al. (2018). Any initial dissolution of $BaSO_4$ would increase $(^{138}Ba:^{136}Ba)_{fluid}$, as $(^{138}Ba:^{136}Ba)_{barite} \gg (^{138}Ba:^{136}Ba)_{fluid}$ at the start of each experiment. In the ASW2, FSW1, and FSW2 trials, CPS remained within analytical uncertainty of the initial time point, indicating no initial dissolution of $BaSO_4$ (Fig. S2). In the ASW1 trial, CPS increased upon $BaSO_4$ addition, indicating net dissolution. We calculated a conservative estimate of the impact of this initial dissolution of $BaSO_4$ on $(^{138}Ba:^{136}Ba)_{fluid}$ using a two-endmember isotope mixing equation that accounts for reservoirs with unequal atomic masses, as our reservoirs are known to have significantly different amounts of ^{136}Ba (see Supplement for full formulation). In the ASW1 trial, initial dissolution of $BaSO_4$ increases $(^{138}Ba:^{136}Ba)_{fluid}$ from 0.32 to 0.59, well below the final measured value of 6.34. Having ruled out significant adsorption of Ba to reactor walls and

constraining the influence of net barite dissolution at the initiation of ASW1, we interpret further changes in $(^{138}Ba:^{136}Ba)_{fluid}$ as representative of ion exchange between the dissolved and solid phases in the system.

The chemical evolution of the fluid is presented in Fig. 1 and Fig. S2. For all $BaSO_4$ and fluid combinations, $(^{138}Ba:^{136}Ba)_{fluid}$ increased toward $(^{138}Ba:^{136}Ba)_{barite}$ over the experimental interval. The magnitude of increase was strongly dependent on the fluid source, with $BaSO_4$ in ASW approaching $(^{138}Ba:^{136}Ba)_{fluid}$ values of 6.34 and 8.44 after 174 d for the synthetic and modern pelagic $BaSO_4$, respectively. Comparatively, experiments with FSW had final $(^{138}Ba:^{136}Ba)_{fluid}$ values of 1.89 and 1.34, again for the synthetic and modern pelagic $BaSO_4$. For experiments with the same fluid source, differences in final $(^{138}Ba:^{136}Ba)_{fluid}$ closely track L_{barite}, consistent with previous findings (see Chapter 2). This relationship is consistent with ion exchange occurring as a surface-mediated process (e.g., (Zhen-Wu et al., 2016; Heberling et al., 2018; Vital et al., 2020). We use a simple model of ion exchange to assess the underlying rate associated with changes in $(^{138}Ba:^{136}Ba)_{fluid}$ (hereafter the "Tracer Model"; see Supplement for a full description). Briefly, we quantify the rate of ion exchange by fitting our experimental results to a time-dependent model of mineral-fluid exchange. Tracer Model initialization accounted for reactor-specific parameters, including initial [Ba], solution volume, and the mass of seed barite in the reactor. The rate of ion exchange was adjusted to minimize the residual sum of squares between experimental and model data. Ion exchange rates were calculated to encompass the range of barite crystal diameters observed in the ocean, 0.5 to 5 µm (Yao et al., 2021), and surface area-normalized assuming spherical grains. Surface area normalization allows comparison of rates between reactors containing differing quantities of seed barite. The tracer experiments using ASW produce modelled rates of ion exchange that agree well with previous studies, including the results of Chapter 2 (Table 3).

In comparison, experiments using FSW exhibited much slower rates of ion exchange. Artificial seawater and FSW experiments had similar concentrations of the major marine salts, trace metals, L_{barite}, pH, and estimated surface area. On key difference between ASW and FSW is the absence of dissolved organic matter in ASW trials. Particulate organic matter (POM), particularly polyphosphate chains, is capable of complexing Ba cations (Gonzalez-Muñoz et al., 2012; Martinez-Ruiz et al., 2020; 2019; 2018). While FSW was filtered to 0.4 µm and therefore did not contain polyphosphate chains that would be considered POM, polyphosphate chains are

known to persist in the dissolved organic matter fraction, nominally defined as organic matter passing through a 0.45 µm filter (DOM; Young and Ingall, 2010) and may contribute to the observed difference in ion exchange rate between the FSW and ASW experiments. While it is beyond the context of this study to characterize the mechanistic controls creating the difference in rate of ion exchange between ASW and FSW trials, isotope-tracer experiments presented here offer the first evidence of ion exchange between pelagic $BaSO_4$ and seawater and indicate that some characteristic of FSW, potentially dissolved Ba complexation by organic matter, slows ion exchange by an order of magnitude when compared rates observed for the same $BaSO_4$ in ASW (Table 3).

3.4.2 Ion exchange and the sediments of the Equatorial Pacific

Our experimental evidence indicates that pelagic $BaSO_4$ can exchange Ba ions with dissolved Ba in adjacent fluids. To evaluate the rate and isotopic impact of this process in the sediments of the Equatorial Pacific, a two-box (pore fluids and $BaSO_4$) mixing model of the sediments was constructed for both $[Ba]_{PW}$ and $\delta^{138}Ba_{PW}$ in the top 0.8 cm of sediment and Monte Carlo error propagation was carried out in in the MATLAB programming environment (CarstenRobens, 2022). Modelling was carried out for the top 0.8 cm of sediment to allow parametrization of Ba fluxes using the findings of Paytan & Kastner (1996), who used this depth range. A schematic representation of the model in Fig. 6 is based on the following assumptions and data: (1) the Ba distribution in the sediments is at steady state; (2) the rates of burial, export, and efflux may be parameterized as described by previous literature for this region (Paytan and Kastner, 1996; Table S1); and (3) Ba ion exchange is allowed between $BaSO_4$ and Ba_{PW}, as they are the only barium containing phases capable of ion exchange (see Supplement for full equations). As in the Tracer Model, ion exchange rates were calculated assuming barite crystal diameters of 0.5 and 5 µm and surface area-normalized assuming spherical grains. As in previous studies, the rate of ion exchange is taken from the forward rate of Ba exchange into $BaSO_4$ (Bosbach et al., 2010; Curti et al., 2010; Torapava et al., 2014; Brandt et al., 2015; Heberling et al., 2018).

For 0.5 µm grains, the resulting rate of ion exchange for the 5 °S, Equator, and 4 °N sediments are 0.05, 0.06, and 0.03 pmol m^{-2} s^{-1}, respectively (Table 3). These rates represent the upper bound on ion exchange in Equatorial sediments, as all cores are slightly oversaturated with

respect to $BaSO_4$. Using the aqueous geochemical modelling program PHREEQC with the pitzer database, Ω_{barite} of 5 °S, Equator, 4 °N = 1.17, 1.32, 1.02, respectively. Modelled rates agree well with the Tracer Model results for modern pelagic $BaSO_4$ in FSW (Table 3). The modelled rates of ion exchange for pelagic barite in FSW and the environment are one to three orders of magnitude lower than previously measured rates. This difference likely arises from significantly different fluid compositions, with prior studies largely focused on non-marine conditions (low pH, low ionic strength). In particular, the rate of ion exchange has been found to decrease with increasing pH (Heberling et al., 2018). In a single trial carried out near seawater pH, (Curti et al., 2010) found an ion exchange rate of 28 ± 16 pmol m^{-2} s^{-1}, within an order of magnitude of the modeled ion exchange rate in the most similar experimental trial (ASW with synthetic $BaSO_4$; 5 pmol m^{-2} s^{-1}). The forward rate constant (k_f) may be calculated following the formulation of Kang et al. (2022), where

$$r = k_f \left(\frac{1}{2\cdot[Ba]/[SO_4]\cdot 0.2} + \frac{[Ba]/[SO_4]\cdot 0.2}{2}\right)^{-0.25} \times \left(\left(\frac{[Ba]\cdot[SO_4]}{k_{sp,barite}}\right)^{0.5} - 1\right)^2 \times exp\left[\frac{-Ea}{R}\left(\frac{1}{T} - \frac{1}{298.15}\right)\right], \quad (2)$$

with the apparent activation energy Ea = 30 kJ mol^{-1} (Palandri and Kharaka, 2004), R is the gas constant, [Ba] = $[Ba]_{PW}$, $[SO_4]$ = 29 mM (Blake et al., 2006), and the temperature and pressure corrected pk_{sp} of -8.39 (Rushdi et al., 2000). Using this formulation, the bulk forward rate constant for the 5 °S, Equator, and 4 °N sites are 21.2, 8.8, and 7.8 pmol m^{-2} s^{-1} and fall between the k_f predicted for seawater and groundwater (Kang et al., 2022; Table 3). The agreement between modeled ion exchange rates in experimental trials and those calculated in sediment cores, combined with the agreement between calculated and predicted k_f, suggests that Ba ion exchange occurs between pore fluids and $BaSO_4$ in the Equatorial Pacific. Barite crystal morphology does not change significantly over the depth studied (Paytan et al., 1996a). These findings suggest that Ba ions exchange between pore fluids and sedimented pelagic $BaSO_4$ and that this ion exchange process is morphology preserving, as observed previously (Bosbach et al., 2010; Vinograd et al., 2013; Klinkenberg et al., 2014; Torapava et al., 2014; Brandt et al. 2015).

3.4.3 Effect of ion exchange on $\delta^{138}BaSO_4$

Calculated fluxes of Ba in the sediments were used to assess the impact of ion exchange on $\delta^{138}Ba_{PW}$ and $\delta^{138}BaSO_4$. The isotopic calculation assumes that (1) the isotopic compositions of the pore fluids and $BaSO_4$ are at steady state, (2) the forward reaction, $BaSO_4$ precipitation, fractionates Ba isotopes with $\Delta^{138}Ba_{barite\text{-}dBa}$ = -0.32 ± 0.03 ‰ (Von Allmen et al., 2010), and (3) pelagic $BaSO_4$ has a Ba isotopic composition of 0.10 ‰ (Horner et al., 2017; Cao et al., 2020). Using the rate of Ba ion exchange calculated in Section 4.3, we find that micro-scale dissolution of $BaSO_4$ related to ion exchange fractionates Ba isotopes with an average magnitude of $\Delta^{138}Ba_{barite\text{-}dBa}$ = +0.15 ± 0.8 ‰ (*n* = 3, ± 2SE; Table 3). This value is consistent with the findings of Chapter 2, where $BaSO_4$ dissolution was found to have $\Delta^{138}Ba_{barite\text{-}dBa}$ = +0.22 ± 0.05 ‰. However, a prior study found $BaSO_4$ dissolution mediated by Na_2CO_3 to be non-fractionating when >10 % of the mineral dissolved (Von Allmen et al., 2010). However, witherite ($BaCO_3$) is well below saturation in these cores (modelled in PHREEQC with the phreeqc database, $\Omega_{witherite} \ll 0.001$). As such, $BaSO_4$ dissolution in the Equatorial Pacific sediments is unlikely to undergo the carbonate mediated dissolution seen in the laboratory experiments of Von Allmen et al. (2010). As dissolution mechanism strongly impacts observed patterns in isotopic fractionation (Wiederhold et al., 2006; Kiczka et al., 2010; Wetzel et al., 2014), this may account for the observation of no Ba isotope fractionation by Von Allmen et al. (2010). Further study is needed to directly constrain the magnitude of $BaSO_4$ dissolution under marine conditions. Our findings indicate that Ba ion exchange occurs between the pore fluids and sedimented $BaSO_4$ of the Equatorial Pacific and imparts an apparent $\Delta^{138}Ba_{barite\text{-}dBa}$ = -0.17 ‰, which results through the combined processes of $BaSO_4$ precipitation ($\Delta^{138}Ba_{barite\text{-}dBa}$ = -0.32 ‰, Von Allmen et al., 2010) and dissolution ($\Delta^{138}Ba_{barite\text{-}dBa}$ = +0.15 ‰) during ion exchange at chemical equilibrium.

3.4.4 Implications for records of $\delta^{138}BaSO_4$

Current use of $\delta^{138}BaSO_4$ as a paleoproxy relies strongly on the fidelity of the primary signature through time (Bridgestock et al., 2018; 2019). While ion exchange certainly affects the measured pore fluid signature, as discussed in Sections 4.2 and 4.3, the high leverage of the solid

in the sediments of the Equatorial Pacific allows $\delta^{138}BaSO_4$ to be viable for proxy applications. Specifically, mass balance calculations indicate that in systems with a degree of isotopic disequilibrium similar to that observed in the present study, sediments with $L_{barite} > 0.78$ are protected from measurable changes to $\delta^{138}BaSO_4$, as the isotopic signature of the system is strongly controlled by the solid (Fig. 7). Assuming no advection of pore fluids, cores in this study have $L_{barite} > 0.99$ (Table 3). However, should dissolved Ba in pore fluids undergo some amount of turnover, the true leverage in the system may be lower, as new input of $[Ba]_{PW}$ effectively increases the leverage of the fluid phase in the system (thereby, decreasing L_{barite}). To create an $L_{barite} = 0.78$ in these cores, $[Ba]_{PW}$ must overturn between ~3,000 – 16,000 times. Based on the Ba efflux rate for these sediments, overturning of the dissolved Ba pool may occur over a timespan of 40 – 250 years (Paytan & Kastner, 1996; McManus et al., 1998). Accounting for overturning of dissolved Ba in these cores can shift the mean $\Delta^{138}Ba_{barite\text{-}dBa}$ from +0.15 to +0.17 ‰. These time spans represent the most rapid overturning of the dissolved Ba pool possible in the system, as large diffusive fluxes are not expected down core, where $[Ba]_{PW}$ is relatively constant. The constancy of $\delta^{138}BaSO_4$ suggests that overturning of the dissolved Ba pool does not significantly overturn $[Ba]_{PW}$ in these cores. Over timescales relevant to Quaternary paleoceanography, effective leveraging of $L_{barite} > 0.78$ allows sedimented pelagic $BaSO_4$ to act as a viable record of ancient open-ocean seawater. In addition to L_{barite}, measurement of strontium (Sr) isotopes in sedimented $BaSO_4$ offers a direct measure of ion-exchange-mediated diagenesis. In samples unaffected by this process, $^{87}Sr/^{86}Sr$ should reflect seawater values at the time of mineral formation, as suggested by Paytan et al. (2002, 1993). In most sediments the age of the pore fluid and that of associated sediment differ, hence their respective Sr isotope ratios also differ and offer an observable signature of ion exchange in $BaSO_4$.

3.4.5 Implications for other isotope systems measured in $BaSO_4$

The finding of Ba ion exchange between dissolved Ba in pore fluids and sedimented pelagic $BaSO_4$ suggests that other isotope systems measured in $BaSO_4$ may bear revisiting, particularly those that are chemically similar to Ba. Radium (Ra) is one such element, with ^{226}Ra commonly measured in $BaSO_4$ to construct sediment age models by calculating the amount of ^{226}Ra decay compared to depth in the sediment. Measurement of this chronometer assumes that

$BaSO_4$ acts as a closed system with respect to Ra (i.e. Ra ion exchange does not occur). Based on the data available at the time, previous studies have suggested that $BaSO_4$ in the cores investigated within the present study act as a closed system with respect to Ra (Paytan et al., 1996a). Such a finding is at odds with the findings of this study, as Ba and Ra ion exchange with $BaSO_4$ are concurrent processes (Heberling et al., 2018). In the original study, Paytan et al. (1996a) suggested closed system behavior due to sedimented $BaSO_4$ exhibiting surface water $^{230}Th/^{232}Th$ values, $^{226}Ra/Ba$ ratios in $BaSO_4$ remaining lower than expected if a partition coefficient (D_{Ra}) of 1 is assumed, and the Ra decay product radon (^{222}Rn) appearing anomalously low despite no known escape mechanism. Since then, further work has challenged the underlying assumptions necessary to support that conclusion: Ra ion exchange with $BaSO_4$ is known to occur (Bosbach et al., 2010; Curti et al., 2010; Vinograd et al., 2013; Klinkenberg et al., 2014; Torapava et al., 2014; Brandt et al. 2015), Ra partitioning into $BaSO_4$ during ion exchange has D_{Ra} as low as 0.08 (Curti et al., 2010), and ^{222}Rn is known to preferentially escape $BaSO_4$ during ^{226}Ra decay (i.e. Rn exhalation; Hosoda et al., 2016). Given that down core $BaSO_4$ show exponential decay of ^{226}Ra, interpreted by Paytan et al. (1996a) to reflect closed-system behavior with no ion exchange, an alternative explanation is that the aforementioned processes were occurring within a reactive system with ^{226}Ra dominated by the $BaSO_4$ signature. Such a $BaSO_4$-leveraged system would produce the same decay trends as the case where $BaSO_4$ acts as a closed system, even if rapid exchange of Ra were occurring between pore fluids and $BaSO_4$ as suggested by Church and Bernat (1972). Under these conditions, measurement of Ra in $BaSO_4$ still offers an accurate method for constructing an age model and associated sedimentation rates: although Ra exchanges between the pore fluid and $BaSO_4$, the Ra signature of the sediment is dominated by the signature of the Ra in $BaSO_4$ (i.e. the leverage of the solid is extremely high for Ra). Further study is needed to determine the impact of ion exchange on ^{226}Ra measurements in sedimented pelagic $BaSO_4$ across a range of $BaSO_4$ leverages.

3.5 Conclusion

The results reported in this study suggest that $BaSO_4$ dissolution involves a degree of isotopic fractionation ($\Delta^{138}Ba_{barite\text{-}dBa} = +0.15$ ‰) and the dissolved Ba-$BaSO_4$ can evolve toward isotopic equilibrium in the presence of an aqueous phase at bulk chemical equilibrium conditions.

The combined effect of $BaSO_4$ dissolution and precipitation, with $\Delta^{138}Ba_{barite\text{-}dBa}$ of +0.15 (this study) and -0.32 (Von Allmen et al., 2010), leads to an observed $\Delta^{138}Ba_{barite\text{-}dBa}$ of -0.17 ‰ when the system achieves isotopic equilibrium. The constancy of down core crystal morphology of $BaSO_4$, as documented previously by Paytan et al. (1996a), suggests that Ba ion exchange in these settings follows the same morphology preserving mechanism as observed in prior studies (Bosbach et al., 2010; Vinograd et al., 2013; Klinkenberg et al., 2014; Torapava et al., 2014; Brandt et al. 2015). Such observations suggest that $\delta^{138}BaSO_4$ recorded in the geologic samples should not be assumed to be constant through time and may reflect some resetting during deposition and burial. The degree to which $\delta^{138}BaSO_4$ is reset will depend on the leverage of the solid in the system (i.e., L_{barite}) and the degree to which the fluid phase is out of isotopic equilibrium with $BaSO_4$. Such constraints are available for recent cores, but must be assumed when characterizing much older sediments. For applications of $\delta^{138}BaSO_4$ as a paleo-proxy, careful site selection will mitigate the impact of ion exchange and preserve the primary signature of ancient open-ocean seawater. For sites with a similar degree of isotopic disequilibrium between pore fluids and sedimented $BaSO_4$, $L_{barite} > 0.78$ satisfy this criterion. Similarly, as $\delta^{138}Ba_{PW}$ is influenced by ion exchange with co-located $BaSO_4$ over relatively short time periods, it seems unlikely that systems with the dissolved Ba pool rapidly overturned by flowing natural fluids preserve unaltered records of the origin of these fluids. When interpreting $\delta^{138}BaSO_4$ in sediments with poor constraints on L_{barite} and dissolved Ba overturning, variations of < 0.17 ‰ should be interpreted with caution as they fall within the range of variation allowable solely by ion exchange.

Figures and Tables

Table 1

Sites of pore fluid, sedimentary BaSO4, and water column data. In some cases, geographically near sites are considered together. This is indicated by the sample group.

Sample group name	Water column				Pore Fluid				$BaSO_4$		
	Cruise	**Stn**	**Lat**	**Long**	**Cruise**	**Core**	**Lat**	**Long**	**Core**	**Lat**	**Long**
4 °N	FK 160115	11	4.00	-140.00	JGOFS	4N-07-A	4.04	-139.85	MC113	4.04	-139.85
Equator		12	0.00	-139.80	EqPac	0-02-A	0.12	-139.74	MC48	0.12	-139.74
5 °S		13	-4.23	-142.23	TT013	5S-07-A	-4.97	-139.74	MC34	-2.89	-139.83

Table 2

Initial conditions for isotope-tracer experiments.

Experiment	Fluid[a]	Barite[b]	Mass $BaSO_4$ (mg)	Initial [Ba] (nM)	±2SE	L_{barite}[c]	Initial $(^{138}Ba/^{136}Ba)_{fluid}$
ASW1	Artificial SW	Synthetic	13	282	14	0.9950	0.32
ASW2	Artificial SW	Pelagic	15	283	14	0.9956	0.33
FSW1	Filtered SW	Synthetic	17	272	14	0.9963	0.38
FSW2	Filtered SW	Pelagic	13	273	14	0.9951	0.37

(a) Artificial seawater was prepared following Smith et al. (1975) and brought to pH ≈ 8.1 by the addition of concentrated potassium hydroxide (KOH) solution. Filtered seawater was collected 400ft offshore from 4.5 m and filtered to 0.4 µm using a Supor polyether sulfone filter.

(b) Synthetic BaSO4 (Puratronic, Alfa Aesar Lot #24177) and marine pelagic BaSO4 from 4 °N site (JGOFS TT013 Stn117 MC7 at 15 cm downcore)

(c) Fraction of Ba_{total} in $BaSO_4$, where $Ba_{total} = Ba_{dissovled} + Ba_{barite}$

Table 3: Modelled rates of Ba ion exchange ($R_{exchange}$) into barite from experimental and field data. High and low estimates for the modelled rate of ion exchange represent the rate assuming a $BaSO_4$ crystal diameter of 5 and 0.5 µm, respectively, spanning the size range of pelagic $BaSO_4$. For previous works, the maximum and minimum rates of ion exchange are provided for comparison. However, we note that prior studies investigated Ba ion exchange in far-from-marine conditions. The one exception comes from Curti et al. (2010), whose slowest rate of ion exchange occurring in a trial investigating ion exchange at near neutral pH in highly ionic fluids. The rate constant of the forward reaction (k_f) was calculated follow Eq (2) for the 5 µm grain size and represents the upper estimate for this value. Predicated k_f for marine and aquatic environments are provided for comparison.

Study type	Sample type	L_{barite}	$R_{exchange}$, 0.5 µm grains (pmols m^{-2} s^{-1})	± 2SE	$R_{exchange}$, 5 µm grains (pmols m^{-2} s^{-1})	± 2SE	[Ba]/[SO_4] (nM/mM)	k_f (pmols m^{-2} s^{-1})	$\Delta^{138}Ba_{barite-dBa}$ (‰)	± 2SE
Experimental	ASW, synthetic $BaSO_4$	0.9949	0.53		0.53					
			5.3		5.3					
	ASW, modern pelagic $BaSO_4$	0.9956	1.0		1.0					
			9.7		9.7					
	FSW, synthetic $BaSO_4$	0.9963	0.10		0.10					
			1.0		1.0					
	FSW, modern pelagic $BaSO_4$	0.9951	0.08		0.08					
			0.8		0.8					
Field	5 °S	0.9993	0.05	0.001	0.51	0.01	1.20E-05	21.2	-0.14	0.20
	Equator	0.9998	0.06	0.001	0.57	0.01	1.20E-05	8.8	-0.12	0.60
	4 °N	0.9998	0.03	0.001	0.34	0.01	1.20E-05	7.8	-0.18	0.50
Prior literature	Curti et al (2010)	0.9900	28	16	28	16				
		0.9974	567	255	567	255				
	Toranava et al (2014)	0.99998	174		174					
		0.99996	694		694					
	Brandt et al (2015)		5		5					
			4630		4630					
	Heberling et al (2018)		110	6	110	6				
			1400	200	1400	200				
	Kang et al. (2022)					Seawater	3.87E-06	0.8		
						Groundwater	4.66E-04	46.0		
						River water	3.78E-03	175.0		

Fig. 1 Temporal evolution of (^{138}Ba:^{136}Ba)$_{fluid}$ during Tracer Experiments with aqueous phases at bulk chemical equilibrium conditions. The grey line corresponds to the (^{138}Ba:^{136}Ba) of the original $BaSO_4$. Uncertainty of (^{138}Ba:^{136}Ba)$_{fluid}$ fall within the points.

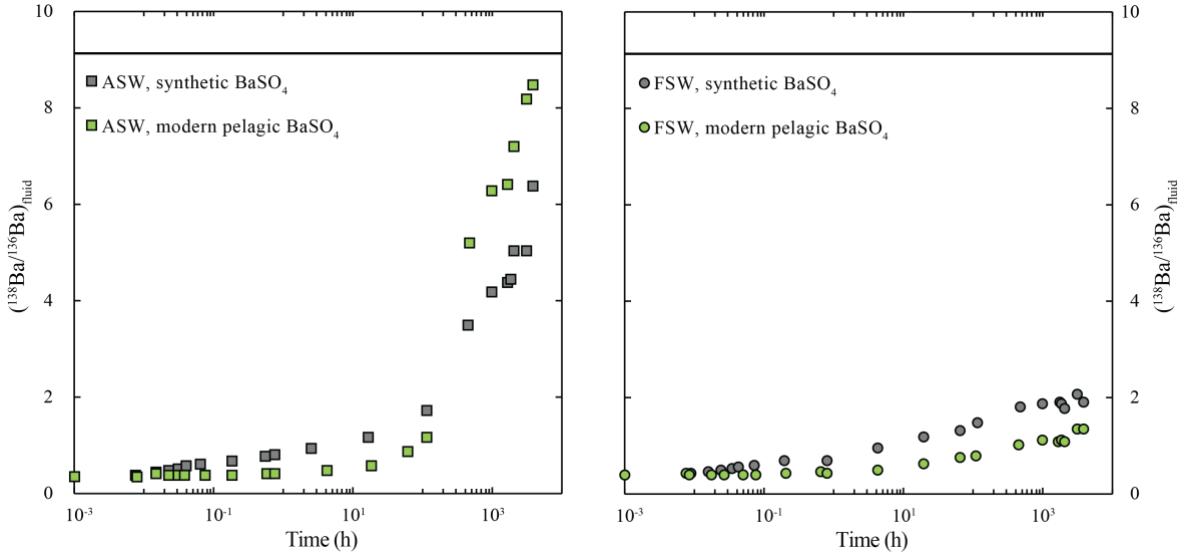

Fig. 2 Ba concentration at isotopic data from the Equatorial Pacific. **A** Complete Ba isotopic and **B** [Ba] depth profiles from Stations 11 (4 °N), 12 (equator), and 13 (4.23 °S) of the ProteOMZ cruise. Uncertainty for isotopic measurements is represented by the black square in the bottom right of panel A and uncertainty for [Ba] is 7 % of the measured value. The mixing line of δ^{138}Ba in the water column (circles) and bottom water (diamonds) is shown in **C.** Pore fluids (triangles) are also plotted. Previously measured δ^{138}Ba are in grey. Newly produced water column data and bottom water fall along the global mixing line. Inset shows pore fluids only, highlight the lack of correlation with $1/[Ba]_{PW}$.

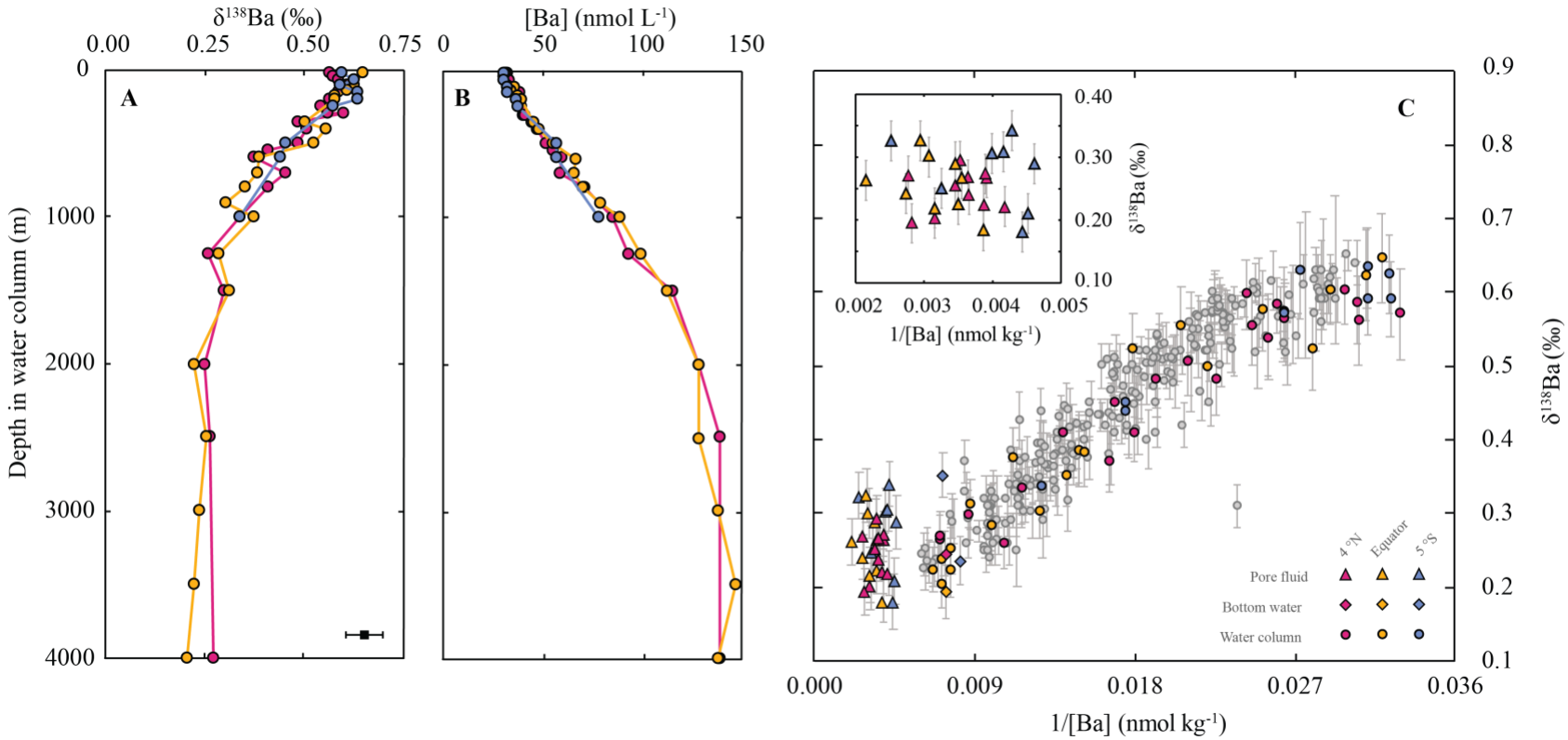

Fig. 3 Ba isotopic composition of sedimented $BaSO_4$ versus depth in the sediment from three sites crossing the Equator along the 140 °W line. Uncertainty for measurements from each core are shown in the bottom right of each panel. Dotted lines indicate the sediment water interface.

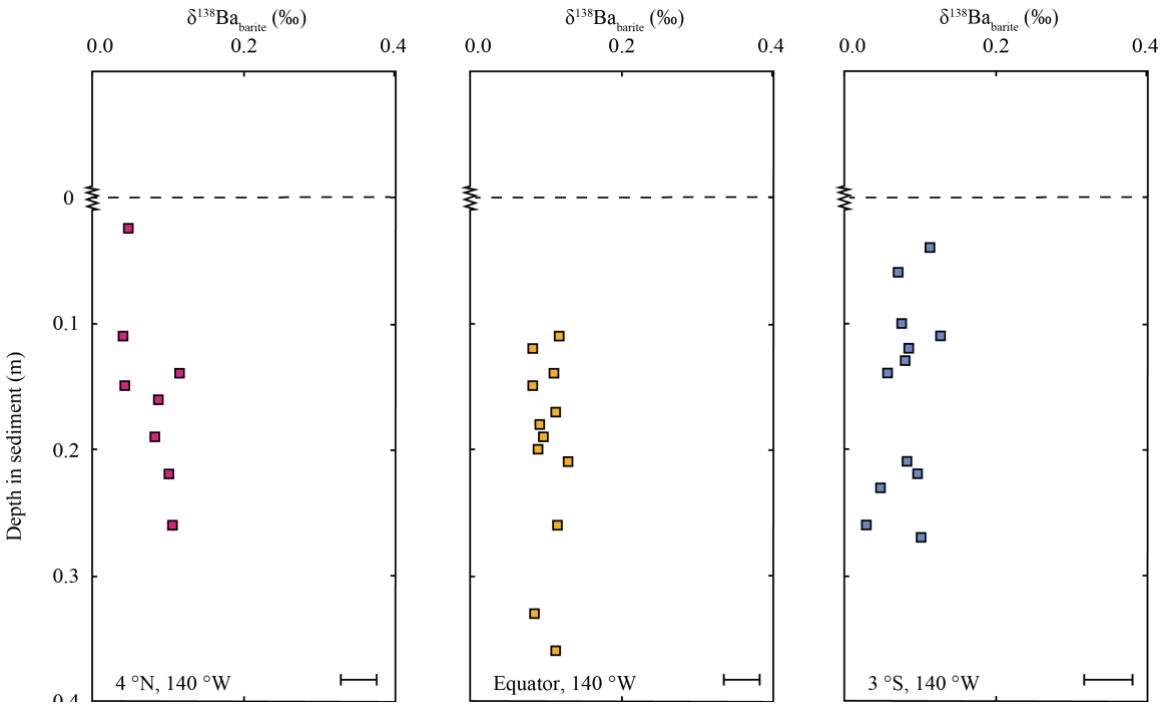

Fig. 4 Concentration of Ba in pore fluids (triangles) versus depth in the sediment from three sites crossing the Equator along the 140 °W line. Barium concentration of bottom water values (diamonds) versus meters above seafloor (mab) are also shown. Uncertainty for these measurements is ± 5 nM.

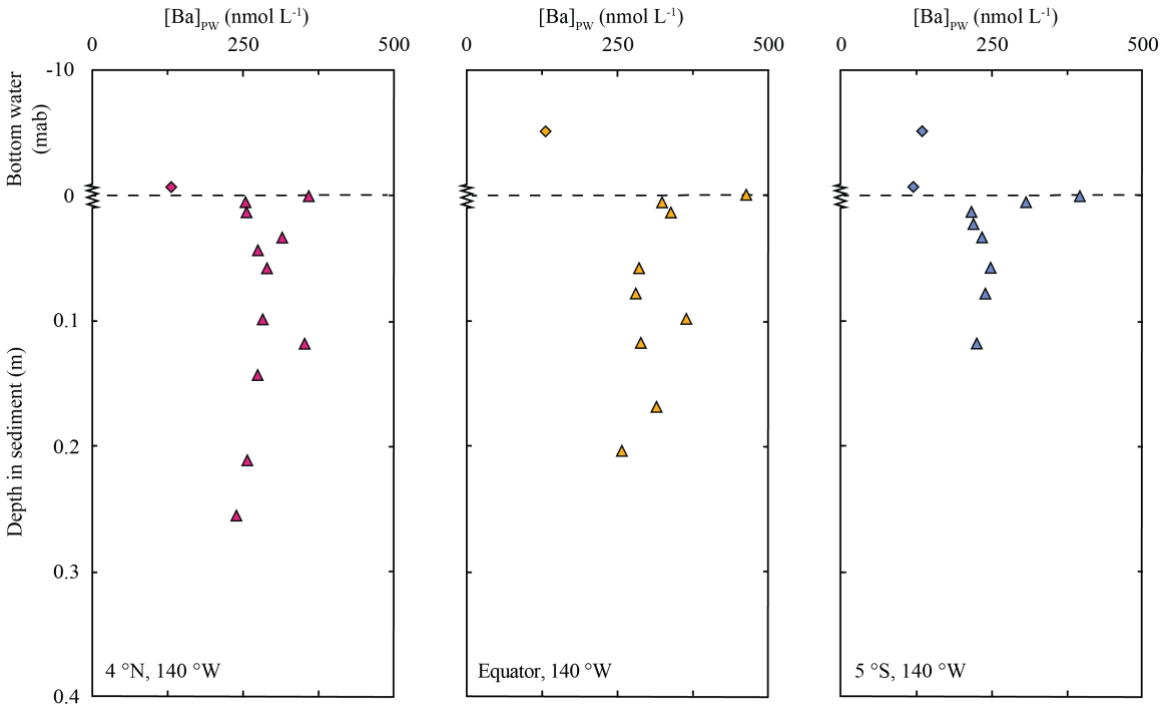

Fig. 5 Isotopic composition of dissolved Ba in pore fluids (triangles) versus depth in the sediment from three sites crossing the Equator along the 140 °W line. Isotopic composition of bottom water values (diamonds) versus meters above seafloor (mab) are also shown. Uncertainty for measurements from each core are represented in the bottom right of each panel. Dotted lines indicate the sediment water interface.

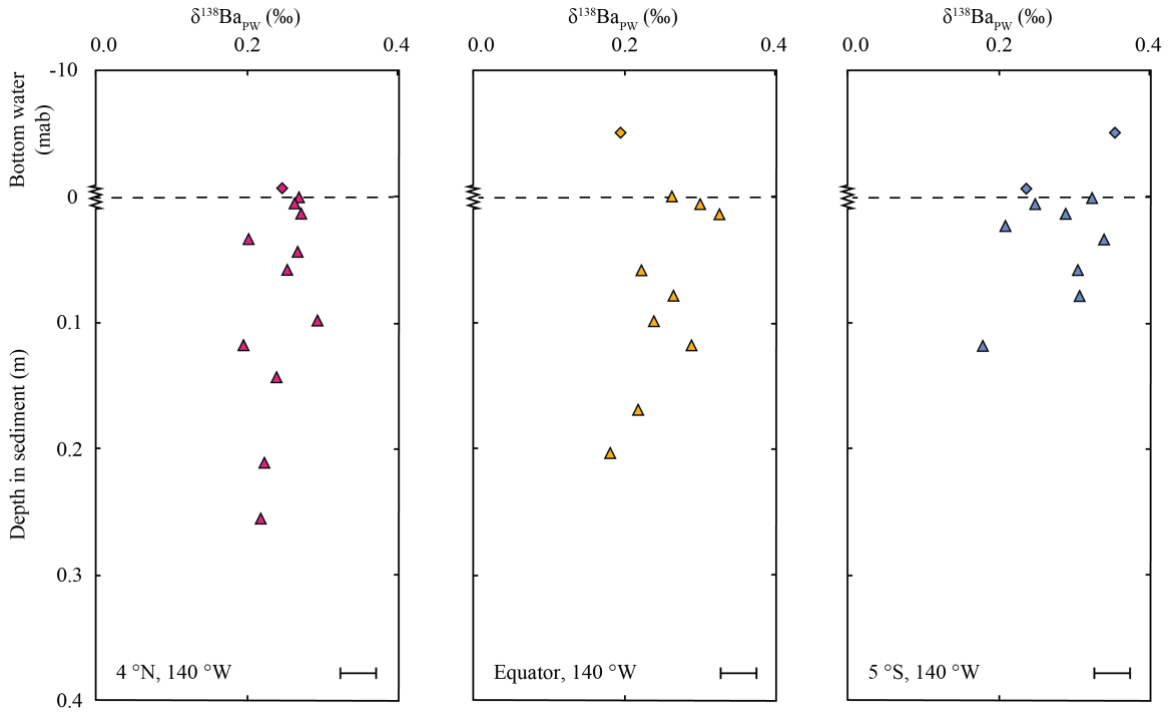

Fig. 6 Box model of Ba cycling in marine sediments. The export of $BaSO_4$ to marine sediments (F_{export}), diffusion of dissolved Ba out of pore fluids into bottom water (F_{efflux}), burial of $BaSO_4$ in the sediments (F_{burial}), and dissolution of $BaSO_4$ ($F_{dissolution}$) are parameterized using prior measurements (Table 4). The flux of Ba by precipitation of $BaSO_4$ ($F_{precipitation}$) is used as the fit parameter.

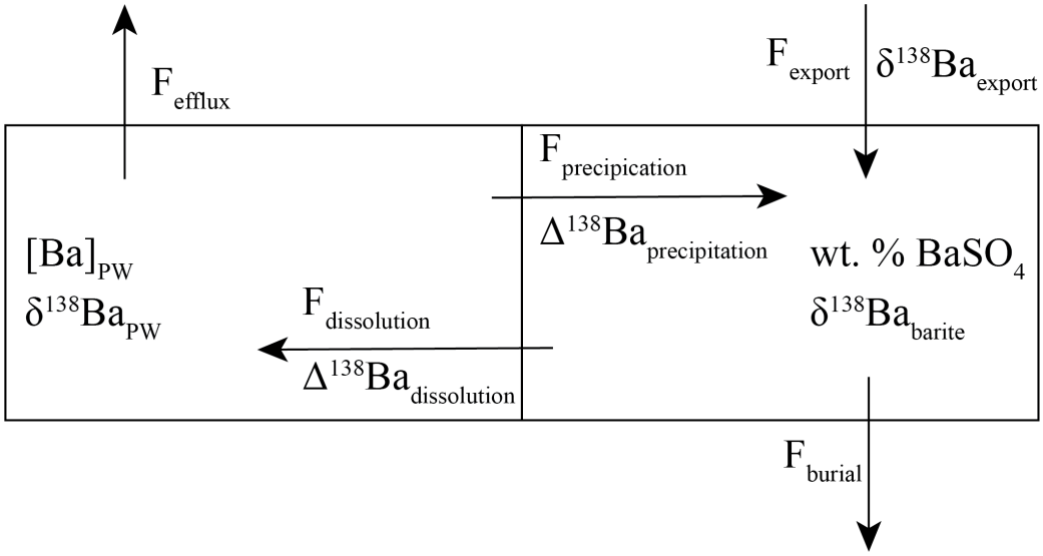

Fig. 7 Isotopic mass balance calculation constraining the Ba isotopic composition ($\delta^{138}Ba$) of a reactive sediment system as a function of the leverage of $BaSO_4$ in the system (i.e. L_{barite}). The purple shaded region represents $L_{barite} \geq 0.78$. The orange shaded region represents the range of L_{barite} for the Equatorial Pacific cores investigated in this study, with $L_{barite} = 0.9993 – 0.9998$.

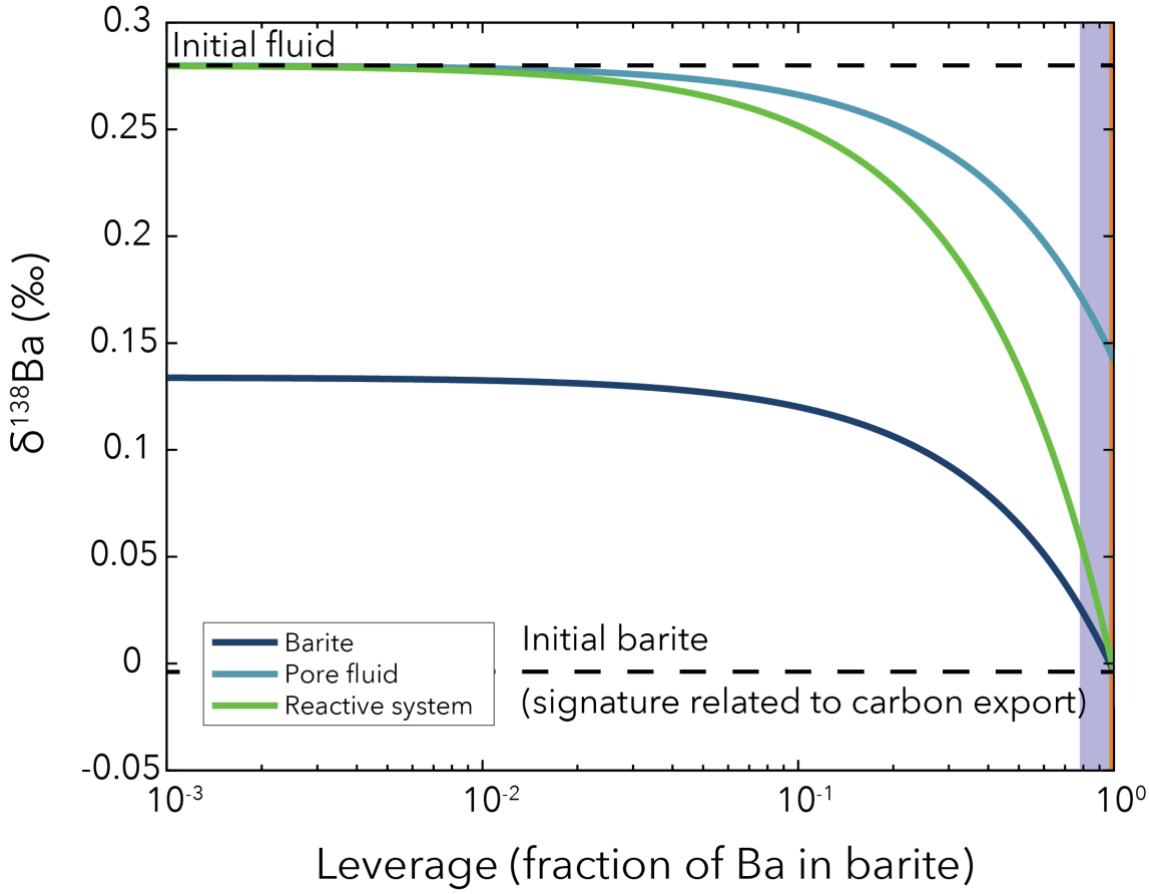

3.6 Supplementary information

Fig. S1 Adapted from Chapter 2. A reactor with no seed $BaSO_4$ crystals was sampled at the start and after 180 days to assess Ba adsorption to HDPE reactor walls. Initial and final [Ba] were found to be within uncertainty of each other, indicating that [Ba] was not significantly affected by bottle adsorption in these experiments.

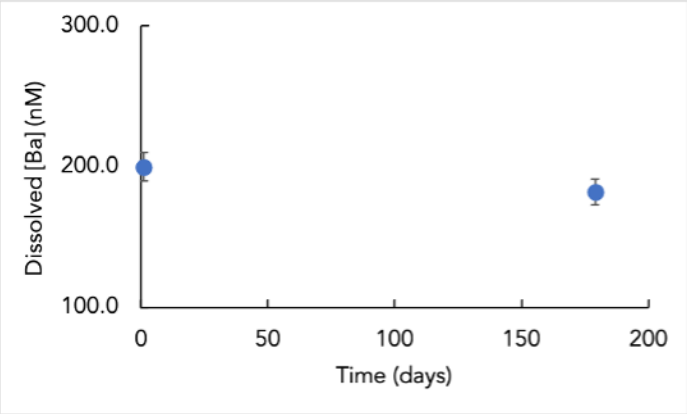

Fig. S2 Counts per second (CPS) for barium over the duration of the Tracer Experiments. Grey shaded areas indicate the uncertainty of the initial measurement. Points falling within the shaded area are considered equivalent to the original solution value (i.e. aqueous phase at bulk chemical equilibrium). Colors represent three separate sessions on the mass spectrometer during which samples from the Tracer Experiments were run. CPS are comparable within measurement session, but not between measurement sessions.

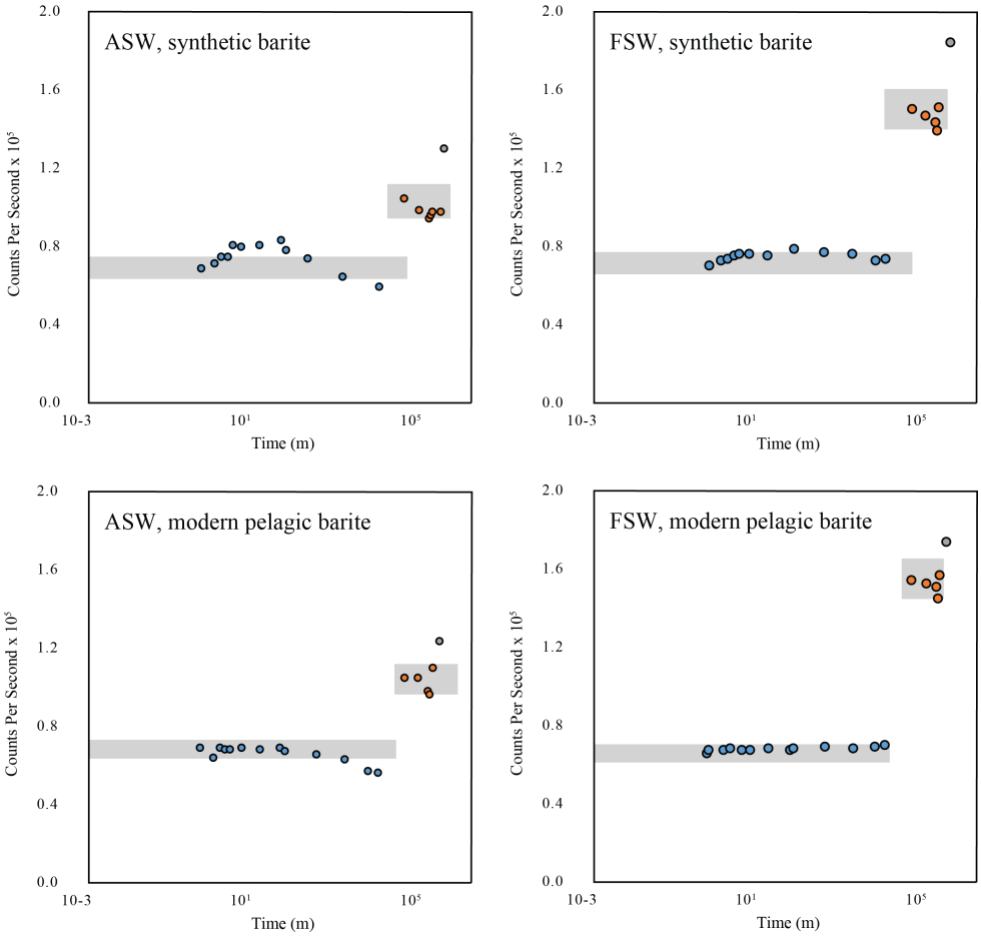

Assessing impact of initial $BaSO_4$ dissolution on progression of (^{138}Ba:^{136}Ba)$_{fluid}$

We calculated a conservative estimate of the impact of this initial dissolution of $BaSO_4$ on (^{138}Ba:^{136}Ba)$_{fluid}$ using a two-endmember isotope mixing equation that accounts for reservoirs with unequal atomic masses, as our reservoirs are known to have significantly different amounts of ^{136}Ba:

$$\left(\frac{^{138}\mathrm{Ba}}{^{136}\mathrm{Ba}}\right)_{fluid} = \left(\frac{^{138}\mathrm{Ba}_{initial\ solid} + {}^{138}\mathrm{Ba}_{initial\ fluid}}{^{136}\mathrm{Ba}_{initial\ solid} + {}^{136}\mathrm{Ba}_{initial\ fluid}}\right) \text{ , and} \quad (1)$$

$$^{m}\mathrm{Ba}_{A} = \left(\frac{f_A + {}^{m}F_A + \mathrm{Ba}_{total} + N_{Avogadro}}{^{m}AW}\right) \quad (2)$$

where f_A = ($CPS_{initial} - CPS_{post\ barite\ addition}$)/$CPS_{initial}$ is the fraction of dissolved Ba added to the fluid due to some initial dissolution of barite, $^{m}F_A$ is the fraction of Ba that is isotope *m* in pool *A*, Ba_{total} is the total grams of Ba in the reactor, $N_{Avogadro}$ is Avogadro's number, and ^{m}AW is the atomic weight of isotope *m*. In the ASW1 trial, initial dissolution of $BaSO_4$ produces a fluid with (^{138}Ba:^{136}Ba)$_{fluid}$ = 0.59, well below the final (^{138}Ba:^{136}Ba)$_{fluid}$ of 6.34 measured in the trial.

Tracer Model: A time-dependent phenomenological recrystallization Tracer Model

Fig. S3 Schematic of the ion exchange model used to assess evolution of (^{138}Ba:^{136}Ba)$_{fluid}$ in Tracer Experiments.

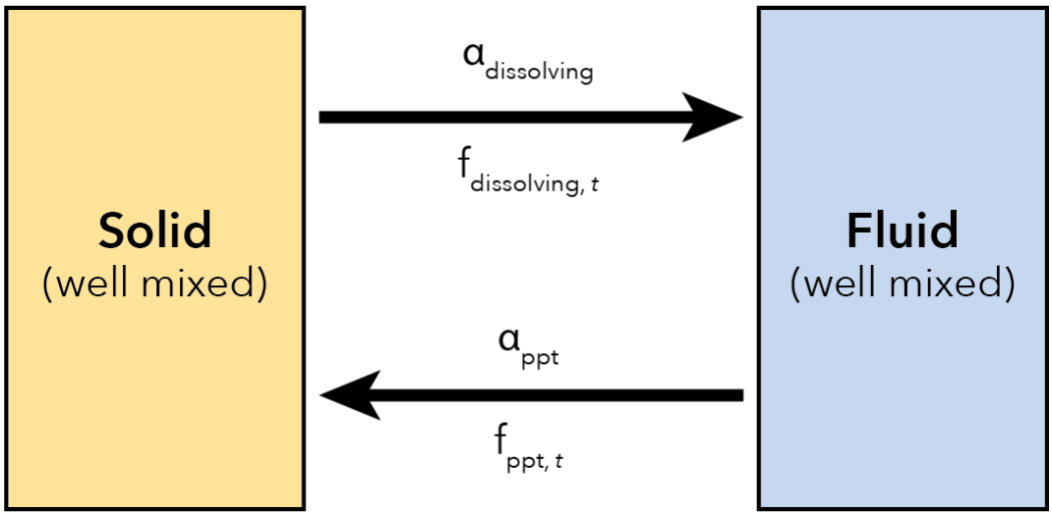

We quantify the rate of ion exchange by fitting our experimental results to a time-dependent model. We modeled the system assuming homogeneous, rather than heterogeneous, recrystallization, with the solid re-homogenized after each timestep. While a simplification, homogeneous recrystallization models can explain the uptake of ^{133}Ba during barite recrystallization at marine-like ionic strength (see Curti et al., 2010; Gorski & Fantle, 2017). Our implementation is resolved each minute, allowing dissolution and reprecipitation at each time step. Model initialization accounted for reactor-specific parameters, including initial [Ba], solution volume, and the mass of seed barite in the reactor. The rate of ion exchange was optimized to minimize the residual sum of squares between experimental and model data. Ion exchange rates were calculated to encompass the range of barite crystal diameters observed in the ocean, 0.5 to 5 µm (Yao et al., 2021), and surface area-normalized using a spherical model for grains. Surface area normalization allows comparison of rates between reactors containing differing quantities of seed barite.

The composition of barite and dissolved barium may be calculated in a reactive system by the isotopic mass balance of all reactive reservoirs, which here include the recrystallizing barite ($\delta^{138}Ba_{bulk\ solid}$), the bulk dissolved barium pool ($\delta^{138}Ba_{solution}$), and the dissolved barium being

released from the solid during recrystallization ($\delta^{138}Ba_{dissolving}$). As this model allows equilibration between the solid and fluid, it follows the homogeneous recrystallization schematic (see Gorski & Fantle, 2017) and has one minute time resolution. The model is written in δ^{138}Ba notation for clarity. Delta notation can be easily converted into ratio space (i.e. $^{138}Ba/^{136}Ba$) using the known ratio of those isotopes in the Ba isotope standard NIST SRM 3104a, with $(^{138}Ba/^{136}Ba)_{NIST\ SRM\ 3104a} = 9.12894$.

The model is as follows:

$$\delta^{138}\mathrm{Ba}_{dissolving,t} = \frac{\alpha_{dissolving} \times \delta^{138}\mathrm{Ba}_{bulk\ solid,t} + 1000 \times (1-f_{dissolving}) \times (\alpha_{dissolving}-1)}{\alpha_{dissolving}-\alpha_{dissolving} \times (1-f_{dissolving}) + (1-f_{dissolving})}, \quad \text{(S1)}$$

at time step *t* where $\alpha_{dissolving}$ is the fractionation of barium isotopes during the dissolution of barite, and

$$f_{dissolving} = \frac{mols\ Ba\ recrystallized\ @\ time=t}{total\ mols\ Ba\ in\ solid}. \quad \text{(S2)}$$

The isotopic composition of the residual solid was calculated by isotopic mass balance:

$$\delta^{138}\mathrm{Ba}_{residual\ solid,t} = \frac{f_{dissolving,t} \times \delta^{138}\mathrm{Ba}_{dissolving,t} - \delta^{138}\mathrm{Ba}_{bulk\ solid,t}}{f_{dissolving,t}-1}. \quad \text{(S3)}$$

The isotopic composition of dissolved barium ($\delta^{138}\mathrm{Ba}_{solution,t}$) was calculated by isotopic mass balance, accounting for mixture of newly dissolved barium ($\delta^{138}\mathrm{Ba}_{dissolving,t}$) during recrystallization with the final fluid from the prior time step (here called the residual fluid,

$\delta^{138}\mathrm{Ba}_{residual\ fluid,\boldsymbol{t-1}}$): (S4)

$$\delta^{138}\mathrm{Ba}_{solution,t} = f_{release,t} \times \delta^{138}\mathrm{Ba}_{dissolving,t} + (1 - f_{release,t}) \times \delta^{138}\mathrm{Ba}_{residual\ fluid,\boldsymbol{t-1}},$$

where

$$f_{release,t} = \frac{\text{mols Ba released to fluid during dissolution}}{\text{total mols Ba in fluid @ time}=t}. \quad \text{(S5)}$$

The mols of Ba released to fluid during dissolution is parameterized by the rate of recrystallization. Following this, precipitation of dissolved barium exceeding [Ba] at $\Omega_{barite} = 1$ occurs, producing new barite with an isotopic composition of

$$\delta^{138}\mathrm{Ba}_{ppt,t} = \frac{\alpha_{ppt} \times \delta^{138}\mathrm{Ba}_{solution,t} + 1000 \times (1-f_{ppt}) \times (\alpha_{ppt}-1)}{\alpha_{ppt}-\alpha_{ppt} \times (1-f_{ppt}) + (1-f_{ppt})}, \quad \text{(S6)}$$

where α_{ppt} is the fractionation of barium isotopes during the precipitation of barite and

$$f_{ppt,t} = \frac{\text{mols Ba precipitated @ time=t}}{\text{total mols Ba in fluid prior to precipitation}}. \quad \text{(S7)}$$

After the first time step, $f_{release,t} \equiv f_{ppt,t}$, as the solution remains near at $\Omega_{barite} = 1$ and only varies due to surface-mediated dissolution and re-precipitation during recrystallization. Given the findings of the precipitation-dominated experiments in this study ($\Delta^{138}\mathrm{Ba}_{barite-Ba(aq)} = -0.33$ ‰), α_{ppt} is estimated as $\alpha_{ppt} = e^{-0.33/1000} = 0.99966$.

After precipitation, the final composition of the bulk solid is calculated as

$$\delta^{138}\mathrm{Ba}_{bulk\ solid,t} = f_{re-ppt,t} \times \delta^{138}\mathrm{Ba}_{ppt,t} + (1 - f_{re-ppt,t}) \times \delta^{138}\mathrm{Ba}_{residual\ solid,t}, \quad \text{(S8)}$$

where

$$f_{re-ppt,t} = \frac{\text{mols Ba precipitated @ time=t}}{\text{total mols Ba in solid}}. \quad \text{(S9)}$$

Finally, the ending isotopic composition of dissolved barium after time step *t* is calculated by isotopic mass balance as

$$\delta^{138}\mathrm{Ba}_{residual\ fluid,t} = \frac{f_{ppt,t} \times \delta^{138}\mathrm{Ba}_{bulk\ solid,t} - \delta^{138}\mathrm{Ba}_{solution,t}}{f_{ppt,t}-1}. \quad \text{(S10)}$$

There are two main assumptions that contribute to the calculations presented here: (1) geometric surface area for barite was estimated assuming spherical barite grains and (2) the

composition of the fluid and solid are fully homogenized after each time step. In the case of (1), Zhen-Wu et al. (2016) found that $\log(k_{dissolution})$ calculated for barite across a range of experimental parameters difference consistently when calculated using the geometric surface area of barite crystals compared to the BET surface area (% difference = 10.4 ± 0.2 %, n = 30, ± 2SE). In that study, $\log(k_{dissolution})$ calculated using the geometric surface area produced slightly faster rates of exchange. Therefore, we are confident that our model provides upper estimates of the rate of ion exchange in our experimental system. Given that reactors were continuously shaken throughout all experiments, assumptions (2) is likely accurate for the fluid phases. For the solid phase, it is unlikely that a full barite crystal becomes isotopically homogenous at one minute time steps. This said, the highly solid-leveraged (high L_{barite}) nature of all experiments discussed here makes the assumption that the exchanging fraction of $BaSO_4$ at each time step has the same (^{138}Ba:^{136}Ba) as the initial solid, as amount of Ba available for exchange at the mineral surface far exceeds the amount of Ba dissolved in the fluid.

Box model of $BaSO_4$ and dissolved pore fluid Ba in Equatorial Pacific sediments

Fig. 6 [reproduced here for clarity] Box model of Ba cycling in marine sediments. The export of $BaSO_4$ to marine sediments (F_{export}), diffusion of dissolved Ba out of pore fluids into bottom water (F_{efflux}), burial of $BaSO_4$ in the sediments (F_{burial}), and dissolution of $BaSO_4$ ($F_{dissolution}$) are parameterized using prior measurements (Table 4). The flux of Ba by precipitation of $BaSO_4$ ($F_{precipitation}$) is used as the fit parameter.

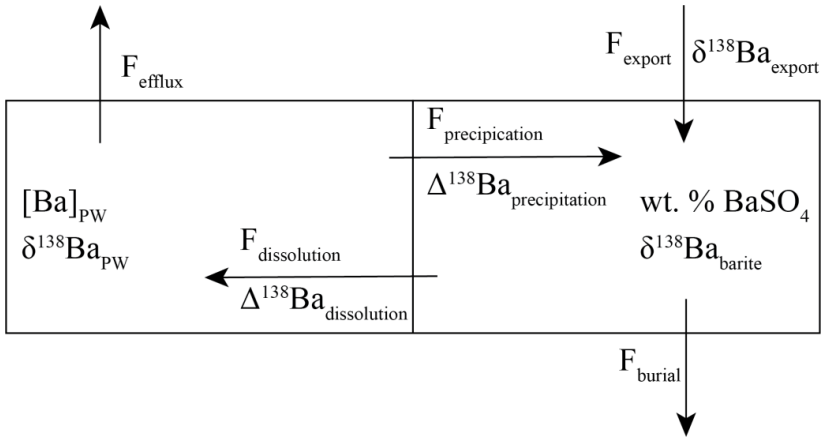

Barium in the sediments of the Equatorial Pacific were modelled using a two box model incorporating the dissolved [Ba] contained in the pore fluids and solid Ba, assumed to be contained in $BaSO_4$. Eagle et al. (2003) define the true percentage of Ba accounted for by $BaSO_4$ in the solid phase as 55 % at 4 °N and 90 % at the equator. This measurement was not made for the 3 °S site, so we are unable to provide constraints on this assumption there. The nearest measured side, 5 °S, had 30 % of solid Ba in the $BaSO_4$ fraction. Using these values and the calculated $\Delta^{138}Ba_{barite\text{-}dBa}$ for each site, there does not appear to be a relationship between the calculated magnitude of fractionation and % of solid Ba contained in $BaSO_4$ (Fig. S4). We assume pore fluids and the solid phase are at steady state. As such, while other particulate phases may influence $\delta^{138}Ba_{PW}$, the observed offset between $\delta^{138}Ba_{PW}$ and $\delta^{138}BaSO_4$ is still representative of $\Delta^{138}Ba_{barite}$.

As such, the general model equations are as follows. Parameter definitions and values are found in Table S1. The fluxes of Ba (in mols m^{-3} d^{-1}) with respect to concentration are

$$\frac{d[Ba]_{PW}}{dt} = F_{dissolution} - F_{efflux} - F_{precipitation} \quad \text{(S11)}$$

and,

$$\frac{d[BaSO_4]}{dt} \times \frac{1}{MM_{barite}} = F_{precipitation} + F_{export} - F_{dissolution} - F_{burial}. \quad \text{(S12)}$$

Where,

$$F_{dissolution} = \frac{[\mathrm{BaSO_4}]}{100} \times \rho_{sed} \times k_{dissolution} \times SSA \times (\Omega_{barite} - 1)^{n_{diss}}, \quad \text{(S13)}$$

following the formulation for mineral dissolution of Sarmiento and Gruber (2006), and

$$F_{efflux} = \frac{1}{d_{sed}} \times f_{sed-flux}, \quad \text{(S14)}$$

and,

$$F_{burial} = \frac{[\mathrm{BaSO_4}]}{100} \times \rho_{sed} \times b_{eff} \times \frac{1}{MM_{barite}} \times \frac{1}{\tau}, \quad \text{(S15)}$$

where τ is the calculated residence time of Ba in $BaSO_4$. The value of $F_{precipitation}$ is calculated based on the other fluxes. Concentration fluxes are then used to calculate isotopic values with respect to the pore fluid, where

$$\frac{d\delta^{138}\mathrm{Ba_{PW}}}{dt} = \quad \text{(S16)}$$
$$\left(\frac{F_{dissolution}}{[\mathrm{Ba}]_{\mathrm{PW}}} \times \left(\delta^{138}\mathrm{BaSO_4} - \Delta^{138}\mathrm{Ba_{barite-dBa}} - \delta^{138}\mathrm{Ba_{PW}}\right)\right)$$
$$+ \left(\frac{F_{efflux}}{[\mathrm{Ba}]_{\mathrm{PW}}} \times \delta^{138}\mathrm{Ba_{PW}}\right) - \left(\frac{F_{precipitation}}{[\mathrm{Ba}]_{\mathrm{PW}}} \times \Delta^{138}\mathrm{Ba_{barite-dBa}}\right),$$

where the dissolution and precipitation terms are defined following Gorski & Fantle (2017), where the $\Delta^{138}Ba_{barite\text{-}dBa}$ of dissolution is the calculated parameter.

Fig. S4 Relationship between the calculated magnitude of isotopic fractionation related to ion exchange ($\Delta^{138}Ba_{barite\text{-}dBa}$) and the % of solid Ba comprised of $BaSO_4$ for the study sites.

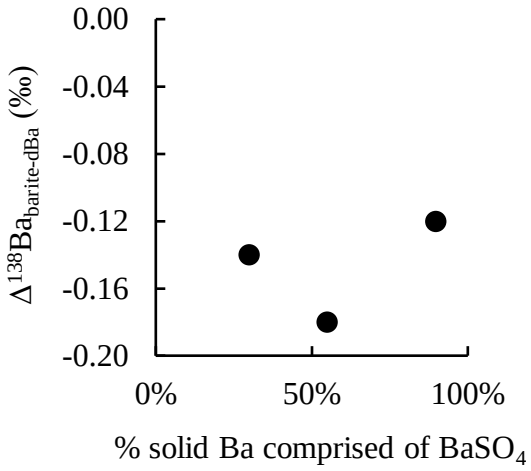

Table S1
Input parameters for the box model of Equatorial Pacific sediments

Parameter	Symbol	Value	Uncertainty	Units	Source
Molar mass of $BaSO_4$	MM_{barite}	232.39		g mol^{-1}	-
Wt. % BaSO4 in the sediments	$[BaSO_4]_{5S}$	0.05		Wt. %	(1)
	$[BaSO_4]_{Eq}$	0.26		Wt. %	(1)
	$[BaSO_4]_{4N}$	0.18		Wt. %	(1)
Isotopic composition of exported $BaSO_4$	$\delta^{138}BaSO4_{export}$	0.10	3.00E-02	‰	(2); (3)
Flux of Ba across the sediment-water interface	$f_{sed\text{-}flux}$	3.84E-07	5.48E-08	mols m^{-2} d^{-1}	(4)
Export of Ba (as $BaSO_4$) out of to the sediments	f_{export}	4.11E-07	1.92E-07	mols m^{-2} d^{-1}	(4)
Burial efficiency of $BaSO_4$	b_{eff}	0.33	3.93E-02		(4)
Sediment density	ρ_{sed}	1.70E+06	2.90E+05	g sed m^{-3}	(5)
Isotopic fractionation due to the precipitation of $BaSO_4$	$\Delta^{138}Ba_{precipitation}$	-0.32	0.03	‰	(6)
Rate of $BaSO_4$ dissolution	$k_{dissolution}$	6.86E-04	1.72E-03	mols m^{-2} d^{-1}	(7)
Order of $BaSO_4$ dissolution	n_{diss}	0.2			(7)
Geometric surface area	SSA	0.27		m^2 g^{-1}	Calculated, 5 µm diameter
Geometric surface area	SSA	2.70		m^2 g^{-1}	Calculated, 0.5 µm diameter
Saturation state of $BaSO_4$	Ω_{barite}, 5 °S	1.17			This study
	Ω_{barite}, Eq	1.32			This study
	Ω_{barite}, 4 °N	1.02			This study
Isotopic composition of the pore water, TTN013 5 °S	$\delta^{138}Ba_{PW}$	0.29	0.03	‰	This study
TTN013 Equator (11cm)		0.28	0.03	‰	This study
TTN013 4 °N		0.27	0.03	‰	This study
Pore fluid concentration	$[Ba]_{PW}$	3.5E-04	2.E-05	mols m^{-3}	This study
		3.9E-04	2.E-05	mols m^{-3}	This study
		3.1E-04	2.E-05	mols m^{-3}	This study
Isotopic composition of $BaSO_4$, TTN013 3 °S	$\delta^{138}BaSO_4$	0.1	0.04	‰	This study, 4 cm
TTN013 Equator		0.12	0.03	‰	This study, 11 cm
TTN013 4 °N		0.05	0.03	‰	This study, 2.5 cm

Sources are as follows: (1) Eagle et al. (2003), (2) Horner et al. (2017), (3) Cao et al. (2020), (4) Paytan & Kastner (1996). (5) Tenzer & Gladkikh (2014), (6) Von Allmen et al. (2010), (7) Zhen-Wu et al. (2016)

Chapter 4: Controls on particulate barium formation in the water column approaching the Polar Front

Abstract

The accumulation rate of pelagic barite ($BaSO_4$) in marine sediments is strongly correlated with the quantity of carbon exported from the euphotic zone and has been used to reconstruct paleo-carbon export over a variety of time scales. To fully utilize this paleo-proxy, controls on the formation of pelagic $BaSO_4$ in seawater, the depths at which it forms, and the spatial footprint of $BaSO_4$ formation in the ocean require further constraint. To that end, shipboard experiments assessing the role of particle size and microbial activity were carried out for waters in the upper 1,000 m of the water column over a transect entering the Polar Frontal Zone (PFZ) in the South Pacific Ocean. We find that particulate barium (pBa) formation occurs largely at depths shallower than 70 m, increases significantly in the PFZ, and requires both microbial activity and pre-existing particles >5 µm. This data resolves, at least in the study region, the question of where pBa forms in the water column. Rates of pBa formation decrease dramatically with depth, with virtually no formation at 1,000 m. Additionally, the data presented here are consistent with high-latitude cycling impacting global oceanic Ba signatures, implying that pBa in the sedimentary record is sensitive to changes in high-latitude circulation dynamics.

4.1 Introduction

The accumulation rate of pelagic barite ($BaSO_4$) in marine sediments (BaAR) is strongly correlated with the quantity of carbon exported from the euphotic zone (i.e. export production; Eagle et al., 2003; Paytan et al., 1996). The BaAR has been used to reconstruct paleo-carbon export over a variety of time scales (Schmitz, 1987; Rutsch et al., 1995; A Paytan et al., 1996; Dean et al., 1997; Nürnberg et al., 1997; Bonn et al., 1998; Bains et al., 2000; Olivarez Lyle and Lyle, 2006; Griffith et al., 2010; Erhardt et al., 2013; Ma et al., 2014; Carter et al., 2016). However, the formation of pelagic $BaSO_4$ in seawater remains insufficiently constrained, particularly with regards to the mechanisms by which pelagic $BaSO_4$ precipitates, the depths at which it forms, and the spatial extent over which precipitation occurs.

Pelagic $BaSO_4$ is observed ubiquitously in the water column, despite much of the ocean being largely undersaturated with respect to the mineral (Monnin et al., 1999; Rushdi et al., 2000; Monnin and Cividini, 2006). To overcome this thermodynamic barrier, some pre-concentration mechanism must accumulate dissolved barium in a manner which promotes $BaSO_4$ formation. While some marine organisms form $BaSO_4$ intracellularly or as a component of their tests (Gooday and Nott, 1982; Finlay et al., 1983; Bernstein and Byrne, 2004), their distribution is too limited to account for the observed occurrence of water column and sedimented $BaSO_4$ (Esser and Volpe, 2002) and their presence is unnecessary for pelagic $BaSO_4$ precipitation (Ganeshram et al., 2003). Rather, $BaSO_4$ is thought to form in association with heterotrophic oxidation of sinking organic matter (Chow & Goldberg, 1960); whereby labile Ba is liberated from decaying phytoplankton within microenvironments enclosed in sinking organic aggregates and provides the necessary Ba input needed to reach $BaSO_4$ saturation. The availability of large aggregates has been tied to $BaSO_4$ production, although little direct evidence for this relationship is available (Bishop, 1988; Stroobants et al., 1991). The connection between particulate organic matter (POM) and particulate barium (pBa) may be further mediated by bacterial production of extra polymeric substances, which are known to bind dissolved Ba (González-Muñoz et al., 2012; Martinez-Ruiz et al., 2018; 2019) and may act as an organic template mediating pelagic $BaSO_4$ formation (Deng et al., 2019; Martinez-Ruiz et al., 2021). Other mineral phases produced by marine microbes, particularly bacterially produced manganese oxides (MnOx; (Cowen and Bruland, 1985; Aoki et al., 2021), may also play a role in dissolved Ba accumulation. Although this mechanism of accumulation has

not been studied directly in the water column, MnOx are known to complex dissolved Ba (Mishra and Tiwary, 1993; Charette et al., 2005; Yokoo et al., 2021; Tani et al., 2021).

The microenvironment model is consistent with observed correlations between the peak in p[Ba] and POM regeneration in the upper mesopelagic zone (Fig. 1 shows a typical p[Ba] curve; Sternberg et al., 2008). Despite this correlation, the depth of pelagic $BaSO_4$ formation is contested, with some lines of evidence suggesting near exclusive formation in the upper 500 m (Chow & Goldberg, 1960; Dehairs et al., 1980; 1990; 1991; 1992; Bishop 1988; Legeleux & Reyss, 1996), whereas others indicate formation throughout the mesopelagic zone as deep as 2000 m (Collier & Edmond, 1984; Dymond et al., 1996; Van Beek et al., 2007; Van Beek et al., 2009; McManus et al., 2002). Clarifying the role of large aggregates, role of microbial activity, and depth of formation on $BaSO_4$ formation is required to accurately interpret the relationship between BaAR and carbon export.

To that end, we conducted a series of shipboard decay experiments to investigate the rates, ranges and dependencies of pBa formation in the South Pacific Ocean approaching the Polar Front. We used added dissolved ^{135}Ba as a tracer of new pBa formation and tested the effects of large aggregates, microbes, and water depth on pBa formation rate by filtering (5 µm cutoff), poisoning (with $HgCl_2$), and conducting experiments over the upper 1,000 m of the water column, respectively. Multi-element geochemical analyses allowed investigation of other particulate phases that might influence Ba uptake rate. Further, we estimate the particulate rain of pBa across the study region based on the observed uptake rate of Ba and find values in agreement with sediment trap studies in the region. These experiments represent the first measurements of pBa formation, associated controls, and Ba uptake rate carried out in the field.

4.2 Methods

4.2.1 Oceanographic section

Experiments and water column samples were carried out and collected along 150 °W between 44.8 and 55.3 °S during cruise RR2004 on the R/V Roger Revelle in between December 2020 and February 2021 (Fig. 2). Frontal regions were defined by characteristic salinity and temperature changes: Four major oceanographic fronts were crossed: 1) the STF occurs where

salinity at 100 m drops from 35.0 to 34.6, 2) the SAF where temperature at 400 m dips below 5 ºC and salinity at 300 m becomes fresher than 34.2, and 3) the PF where the temperature minimum rises above 200 m (Balch, 2020; Orsi et al., 1995). The sampling line began south of the Sub-tropical Front at 39.50 ºS, crossed the Sub-Antarctic Front (SAF) at 53.66 ºS, and approached the Polar Front (PF) at 55.66 ºS (for station locations and names see Table 1). We focus specifically on the Sub-Antarctic Mode Waters (SAMW), as the chemical fingerprints of this water mass propagates to the low latitudes, influencing large scale primary productivity and basin-scale chemical signatures (Sarmiento et al., 2004; Sexton and Norris, 2011; Balch et al., 2019). The SAMW lies between potential densities (σ_θ) of $26.5 < \sigma_\theta < 27.1$ kg m^{-3} (Hartin et al., 2011) and outcropped between 52.8 and 57.4 °S during our field excursion (pers. comm. Hilde Oliver, WHOI), spanning the SAF and PF.

The depths at which water was sampled for experiments were defined using real-time CTD information during casts to pinpoint the depth of the chlorophyll maximum, the region of maximum particle attenuation, and the depth of the oxygen minimum for the cast. The chlorophyll maximum depth (z_{ChL}) was defined as the subsurface peak in fluorescence, which is strongly correlated to chlorophyll abundance (Yentsch and Menzel, 1963). The depth of maximum particle attenuation ($z_{max\text{-}deg}$) was operationally defined as the depth just below z_{ChL} at which the beam transmissivity of a transmissometer had the greatest negative slope (defined visually), which is indicative of decreasing particle abundance (Ohnemus et al., 2018). Finally, the depth of the oxygen minimum for the cast ($z_{ox\text{-}min}$) was defined using the CTD mounted dissolved oxygen sensor. Because hydrographic casts were limited to the top 1,000 m, $z_{ox\text{-}min}$ was located at 1,000 m for each station.

Based on these classifications, Stations C and D fell within the outcropping of the SAMW, with the chlorophyll max depth (z_{ChL}) and depth of maximum particle degradation ($z_{max\text{-}deg}$) occurring in the SAMW and the oxygen minimum depth ($z_{ox\text{-}min}$) for each station's cast falling in the deeper Antarctic Intermediate Water mass (AAIW). The more northern Stations A and B fell outside of the outcropping region, with the z_{ChL} and $z_{max\text{-}deg}$ occurring in the surface waters above the subducted SAMW and $z_{ox\text{-}min}$ falling in the AAIW.

4.2.3 Isotope-tracer experiments

Experiments were carried out at four stations to investigate the role of depth, microbial remineralization of organic matter, availability of large aggregates, and oceanographic region on pBa formation. These parameters were assessed by 1) carrying out experiments across three relevant depths at each station, 2) performing poisoned (P) and un-poisoned (uP) trials, 3) performing filtered (F) and unfiltered (uF) trials, and 4) carrying out the full suite of experiments at 4 stations across a transect spanning 11 ° of latitude approaching the Polar Front.

The formation of new pBa was monitored using uptake dissolved ^{135}Ba, which was added as a dilute solution of $BaCl_2$ to all experiments. The ^{135}Ba-tracer was prepared by dissolving $^{135}BaCO_3$ (Oak Ridge National Laboratory) in 1 mL of 18.2 MΩ water, then addition 0.5 mL of Optima-grade HCl to convert the solid to $^{135}BaCl_2$. The solution was refluxed in a sealed PTFE vial overnight at 80 °C and dried down the following day. Following this, 18.2 MΩ water was added to bring the ^{135}Ba-tracer to a final concentration of 36.96 µg ^{135}Ba (g solution)$^{-1}$. For each set of experiments (i.e. at each depth of each station), 1.5 L of seawater was collected in acid cleaned 5 L LDPE cubitainers from the hydrographic rosette. Before addition of the ^{135}Ba-tracer, 60 mL of unamended seawater was collected to assess dissolved Ba concentrations (d[Ba]). Following this, the remaining 1,440 mL of seawater was amended with ^{135}Ba-tracer. Dissolved [Ba] in the water column was estimated [$Si(OH)_4$] data from the nearest station following the formulation of Bates et al. (2017), where

$$[Ba]_{predicted} = 0.6296*[Si(OH)_4] + 38.63, \quad (1)$$

with the addition of ^{135}Ba target to bring $\Omega_{barite} \approx 1$ The exact addition of ^{135}Ba-tracer and true Ω_{barite} for each experiment is found in Table 1.

Following the addition of the ^{135}Ba-tracer, the sample was split into two 720 mL aliquots. To assess the role of large aggregates on pBa formation, one aliquot was filtered through an acid-cleaned 5 µm polyether sulfone (PES) membrane filter, while the other 720 mL remained unfiltered. Following this, the role of microbial activity on pBa formation was tested by splitting each 720 mL aliquot into two further 360 mL aliquots, one of which was poisoned by the addition

of 72 µL of saturated $HgCl_2$ solution (Ganeshram et al., 2003). Finally, each 360 mL solution was split into five 60 mL HDPE vials. A full outline of the experimental setup is shown in Fig. 3. All 60 mL vials were then placed in an opaque plastic bag to limit exposure to photosynthetically active radiation. Subsequently, samples from z_{ChL} and $z_{max\text{-}deg}$ were transferred to a water bath regulated to the ambient surface temperature at the collection site, while samples from $z_{ox\text{-}min}$ were transferred to a 4 °C refrigerator.

At each time point, full 60 mL vials were filtered onto 25 mm, acid-cleaned 0.22 µm PES filters using an acid-cleaned HDPE syringe within a clean glove box aboard the ship. Prior to sample collection, 24 mL of 18.2 MΩ water was passed over the filter. After the sample was passed through the filter, 24 mL of 0.22 µm filtered surface seawater was passed through the sample filter to displace any remaining fluid in the interstitial space of the filter, as any remaining fluid may lead to artificially high ^{135}Ba measurements. Following this, filters were placed in individual acid-clear filter holder slides and sealed. Samples were stored at room temperature and remaining in storage for 2 months prior to analysis. Timepoints for each station are shown in Table 1. Duplicate samples were taken at the second and final time points.

Three procedural blanks were taken per station to assess any input of pBa from the filtering method. The blanks consisted of 60 mL of 0.22 µm filtered surface seawater being processed in the same manner as samples: poured from a 5 L cubitainer, filtered through a 5 µm PES, and collected on a 25 mm, 0.22 µm PES filter using an acid-cleaned syringe. Procedural blanks had an average pBa of 27 ± 13 pmol L^{-1} and an average ^{135}Ba:^{137}Ba of 0.57 ± 0.05 (±2SE, n = 11).

Analytical methods

4.2.4 Measurement of ^{135}Ba:^{137}Ba and pMe in particulates

Particulate samples were prepared for analysis by leaching filters in 12.3 mL of 0.6 M HCl at 80 °C for ≥16 h. Treatment with 0.6 M HCl has a significant benefit over more intense leaching procedures using nitric (HNO_3) or hydrofluoric (HF) acids: leaching samples in 0.6 M HCl does not dissolve the PES filter, which can contribute both Ba and organic sulfur to a sample (Planquette & Sherrell, 2012). Furthermore, the fraction of Ba (also Cd, Mn, and P) recovered by leaching

with 0.6 M HCl is equivalent to recovery using multi-acid total digestions but with considerably lower reagent-derived blank contributions (Planquette & Sherrell, 2012).

Sample leachates were analyzed for their multi-element geochemical compositions on a reverse quadrupole ICP-MS (iCAP-RQ, Thermo Fisher Scientific) at the WHOI Plasma Facility. A 100 µL aliquot was subsampled from each of the 12.3 mL sample leachates, diluted to 1000 µL with 900 µL of 2% HNO_3, and spiked with 100 µL of In (indium) solution, an internal standard added to all samples, standards, and blanks. Elemental quantification in sample solutions was achieved via comparison of blank-corrected ion beam intensities to those of a reference curve constructed from measurement of six standards with known. Analytical uncertainties from ICP-MS analysis refer to the propagated uncertainties from ion counting statistics, In normalization, and from the goodness-of-fit of the standard reference curve. Typical uncertainties were 7 % (±1 RSD; relative standard deviation). Measured concentrations were converted to experimental particulate concentrations by subtracting the procedural blank from the leachate and normalizing by the measured volume of water passed through each filter.

4.3 Results

4.3.1 Particulate barium formation across the Sub-Antarctic and Polar Frontal Zones

We report changes in p[Ba], $(^{135}Ba{:}^{137}Ba)_{particulate}$, and the uptake rate of Ba into the particulate phase for all experiments. Measured d[Ba] from adjacent trace metal rosette deployments are also reported and used to calculate the initial Ω_{barite} of each experiment and account for any influence of the initial Ω_{barite} on p[Ba], $(^{135}Ba{:}^{137}Ba)_{particulate}$, or Ba uptake rate into the particulate phase. Across the study region, p[Ba] increases in uF-uP experiments at z_{ChL} approaching the PF, from an average of 58 pmol L^{-1} at Stn A to 1,190 pmol L^{-1} at Stn D. At $z_{max\text{-}deg}$, p[Ba] also increases in the SAMW outcropping region, with the largest increase occurring in the station at the Polar Front . At $z_{ox\text{-}min}$, p[Ba] increases at Stn C but shows no increase at the PF. In comparison, the F-uP, uF-P, and F-P experiments show changes in p[Ba] that are consistently less than 75 pmol L^{-1} across the transect. Replicates showed little variability (Fig. 4). Generally, minor changes in p[Ba] occur at the oxygen minimum for each cast (1000 m) and large amounts of pBa formation only occurs in the uF-uP experiment in the SAMW outcropping region.

Raw changes of (^{135}Ba:^{137}Ba)$_{particulate}$ for all experiments are shown in Fig. 5 and provide information regarding the source of Ba to pBa formed during the experimental period. As each trial started out with a slightly different (^{135}Ba:^{137}Ba)$_{particulate}$, the initial value for each experiment is subtracted from all time points to aid visual clarity when comparing different stations and depths (Fig. 6). Increases in (^{135}Ba:^{137}Ba)$_{particulate}$ indicate the majority of Ba uptake draws from the dissolved phase, which was labelled with a ^{135}Ba isotope spike. Decreases in (^{135}Ba:^{137}Ba)$_{particulate}$ from the initial value indicate net formation of new pBa with Ba sourced from Ba originally in the particulate phase. The measurement has an uncertainty of ± 0.1 in (^{135}Ba:^{137}Ba)$_{particulate}$ space. The greatest increase in (^{135}Ba:^{137}Ba)$_{particulate}$ occurred in the uF-uP experiments at z_{ChL}. Coincident with the increase in p[Ba], (^{135}Ba:^{137}Ba)$_{particulate}$ increased significantly in the SAMW outcropping region. There was one exception at Stn C, where (^{135}Ba:^{137}Ba)$_{particulate}$ decreased at $z_{ox\text{-}min}$, indicating new pBa formation from Ba sources with natural Ba isotope ratios. Although little pBa formed in F-P, F-uP, and uF-P experiments, it is productive to outline variations in (^{135}Ba:^{137}Ba)$_{particulate}$ to determine if the source of Ba to pBa changes. Similar to uF-uP experiments, there is a clear depth structure which impacts what source of Ba enters pBa. At z_{ChL} and $z_{max\text{-}deg}$, (^{135}Ba:^{137}Ba)$_{particulate}$ generally increases due to uptake from the dissolved pool, while (^{135}Ba:^{137}Ba)$_{particulate}$ at $z_{ox\text{-}min}$ tends to remain unchanged or decrease, indicating uptake of Ba from sources that were initially not dissolved.

When interpreting changes in (^{135}Ba:^{137}Ba)$_{particulate}$, it is important to remember that changes in the ratio do not reflect the magnitude of pBa formed, only the source of Ba to the newly forming particulate. This is because measured changes in (^{135}Ba:^{137}Ba)$_{particulate}$ represent the uptake of new Ba relative to the amount of pre-existing pBa (i.e., an uptake of 10 atoms of ^{135}Ba in a system with pBa = 100 atoms will produce the same change in (^{135}Ba:^{137}Ba)$_{particulate}$ as the uptake of 1 atom of ^{135}Ba where pBa = 10 atoms). Therefore, we also calculate the uptake rate of Ba into the particulate phase based on accumulation of ^{135}Ba following the formulation of Cox et al. (2014), where

$$\mathrm{Ba}_{total}\ \text{Uptake Rate}\ (\text{nmol L}^{-1}\text{d}^{-1}) =$$

$$\frac{^{135}\mathrm{Ba}_{sample}(\text{nmol L}^{-1}\text{d}^{-1}) - {}^{135}\mathrm{Ba}_{preformed}(\text{nmol L}^{-1}\text{d}^{-1})}{[^{135}\mathrm{Ba}]_{spike}(\text{nmol L}^{-1}) + [^{135}\mathrm{Ba}]_{dissolved}(\text{nmol L}^{-1})} \times [\mathrm{Ba}]_{dissolved}(\text{nmol L}^{-1})\,. \qquad (2)$$

In this formulation, $^{135}Ba_{sample}$ is the ^{135}Ba in the particulate phase measured using ICP-MS analysis of the filter, normalized to the volume of seawater and one day of incubation. Preexisting $^{135}Ba_{sample}$ was accounted for by subtraction of $^{135}Ba_{preformed}$, which represents the value of the particulate blank. It is assumed that the particulate blank is in steady state (that is, it represents the Ba already in the particulate fraction and any possible natural uptake that could occur is negligible). Dividng the particulate ^{135}Ba by the total dissolved ^{135}Ba yields the fraction of ^{135}Ba that has moved from the dissolved pool into the particulate pool per day. The total dissolved ^{135}Ba is comprised of the dissolved ^{135}Ba

Uptake rates are shown in Fig. 7. In F-P, F-uP, and uF-P experiments the uptake rate of Ba varied by one order of magnitude across the transect, with rates ranging between 0.00 and 1.88 nmols L^{-1} d^{-1}. There is no latitudinal trend in these experiments and the highest uptake rates tended to be seen in at the oxygen minimum for each cast. In uF-uP experiments, maximum Ba uptake rate increased by two orders of magnitude, from 0.00 to 20.22 nmols L^{-1} d^{-1}. A strong latitudinal trend was observed, with uptake rates at z_{ChL} increasing progressively toward the Polar Front. At Stns A and B, outside of the SAMW outcropping region, Ba uptake rate was highest at $z_{ox\text{-}min}$. Crossing into the SAMW outcropping region, Stns C and D had the highest Ba uptake rates at z_{ChL}.

We evaluate the role of Ω_{barite} on the changes described above. Additions of ^{135}Ba isotope spike were determined based on the $[Si(OH)_4]$ data from the nearest station. Because the nearest $[Si(OH)_4]$ available was up to 1° of latitude away from the experimental sites, experiments possessed variable initial Ω_{barite}. To assess the initial Ω_{barite}, d[Ba] was measured in the water column from adjacent stations from water collected using the trace metal sampling system (Table 1). Based on d[Ba] measured in the water column and the known amounts of ^{135}Ba spike added to each experiment, initial Ω_{barite} fell between 0.9 and 1.5 (Table 1). We assess the impact of initial Ω_{barite} on the maximum p[Ba], $(^{135}Ba{:}^{137}Ba)_{particulate}$, or Ba uptake rate into the particulate in each experiment using a Student's t-test with a significance criteria of $\alpha = 0.05$. There is no significant correlation between initial Ω_{barite} and any of the three variables: maximum p[Ba] ($p = 0.40$), maximum $(^{135}Ba{:}^{137}Ba)_{particulate}$ ($p = 0.96$), and Ba uptake rate ($p = 0.19$), indicating that the variation in initial Ω_{barite} did not significantly influence the results of those three variables.

4.3.2 Changes in lithogenic particulates

The concentration of lithogenic particles in the incubations was assessed by measuring p[Y] (yttrium, a Rare Earth Element). This element was chosen over more traditional lithogenic tracers (e.g., aluminum, titanium) since Y possesses a low filter blank, which is advantageous given the low concentrations of lithogenic particles in the South Pacific and small experimental volumes. Moreover, Y is a robust tracer of lithogenic input, and is strongly correlated with Al and Ti in the North Atlantic (Ohnemus and Lam, 2015). Across the experimental transect, particulate yttrium (pY) varies by 0.5 pmol L^{-1} (Fig. 8), representing a relatively small change compared to basin-scale variations on the magnitude of 8 pmol L^{-1} observed elsewhere (Kuss et al., 2001).

4.3.3 Changes in organic particulates

The formation of pBa in the water column has been linked to the availability and degradation of organic matter, which acts to pre-concentrate dissolved Ba and allow POM-associated microenvironments to reach $BaSO_4$ saturation (Martinez-Ruiz et al., 2018, 2021). Therefore, elements associated with organic matter are used to examine the quantity and remineralization of POM present in the experiments. Because of the small volume of experiments relative to detection limits and filters blanks, the most common tracer of POM that can be measured by ICP-MS, particulate phosphorous (pP), could not be measured in the experiments. Instead, we use particulate cadmium (pCd) to interrogate POM, as it is known to show a strong correlation with pP and enters cells through non-specific uptake (Ho et al., 2003; Horner et al., 2013; Ohnemus and Lam, 2015). Therefore, the initial amount of POM in each experiment was assessed by measuring p[Cd] at the start of each experiment.

Measured values of initial p[Cd] range between 0 and 58 pmol L^{-1} and agree well with prior measurements of p[Cd] in the Southern Ocean (Cloete et al., 2021). At z_{ChL} and $z_{max\text{-}deg}$, initial p[Cd] increases toward the Polar Front in uF-uP experiments, with an increase from 0.8 to 58 pmol L^{-1} between Stns A and D at z_{ChL} and from 13 to 18 pmol L^{-1} at $z_{max\text{-}deg}$ (Fig. 9).

4.3.4 Changes in particulate manganese

Particulate manganese (pMn) was measured in all experimental samples because of the strong ability of manganese oxides (MnO_x) to complex dissolved metal cations, including Ba^{2+} (Tani et al., 2021; Yokoo et al., 2021). While iron oxides have the same ability to complex dissolved Ba^{2+}, the particulate iron data is not available for these experiments because of the water collection method. Therefore, we discuss p[Mn] as an analog for the abundance of particulate oxides in the water column generally, as MnO_x accounts for 70% of pelagic pMn (Lam et al., 2015). Across the transect, p[Mn] varied between 4.2 and 202.6 pmol L^{-1} (Fig. 10), within the range of values observed elsewhere in the Southern Ocean (Bowie et al., 2009). The lowest values occur at z_{ChL}, as expected because of the photoreduction of pMn in sunlit surface waters, while the highest p[Mn] occurred at $z_{ox\text{-}min}$ (Sunda and Huntsman, 1994). There was no systematic variation between the experimental conditions, indicating the p[Mn] was not affected by filtering to 5 µm or the addition of $HgCl_2$. There are no strong latitudinal trends approaching the Polar Front.

4.4 Discussion

Controls on pBa formation were assessed using manipulation experiments. The combined presence of particulates > 5µm and microbial activity increase pBa formation, as seen in uF-uP experiments (Fig. 4). Near the Polar Front at Stn D, changes in $(^{135}Ba{:}^{137}Ba)_{particulate}$ in F-P experiments indicate that some amount of pBa forms when there are only small particles (< 5 µm) and no microbial activity, although the amount of new pBa formed represented only a 4 % increase over pre-existing pBa (Fig. 6). Both F-uP and uF-P experiments produced similar results to F-P experiments, with p[Ba] representing 5 % and 4 % of the pBa formed in uF-uP experiments. Given the similarity in F-P, F-uP, and uF-P trials, it is apparent that both particulates > 5 µm and microbial activity are important for pBa formation. We assess the latitudinal and depth dependencies across the transect to determine where pBa formation occurs spatially in the ocean. Next, a multi-element analysis incorporating trends in p[Cd] and p[Mn] allows a closer look at possible controls on pBa formation.

Spatial footprint of pBa formation across the transect

4.4.1 Insights into mechanisms of pBa formation and associated latitudinal trends

Strong latitudinal trends were observed for the formation of pBa across the transect. Experiments carried out further from the Polar Front at Stns A and B had much smaller difference amongst experimental conditions, with little pBa forming across all conditions. At these stations, between 57 % and 100 % of p[Ba] in uF-uP experiments was also observed under F-P, F-uP, and uF-P experimental conditions (Fig. 4). Approaching the Polar Front, the magnitude of p[Ba] and rate of Ba uptake in uF-uP experiments became increasingly different from those of F-P, F-uP, and uF-P experiments (Fig. 4 & 7). Generally, the increase in Ba Uptake Rate observed from Stn A to D agrees well with observations of increasing p[Ba] across the SAMW outcropping region between 46.8 °S to 53.7 °S (Cardinal et al., 2001). This latitudinal trend suggests that other factors, in addition to large particles and microbial activity, are important for significant pBa production, and that such conditions are only encountered approaching the Polar Front at the time of sampling.

Latitudinal controls on pBa formation were first assessed through the relationship of pBa with POM. We investigate correlations between Ba uptake rate and initial p[Cd] (as a proxy for POM) to interrogate the importance of the quantity of substrate organic matter on pBa formation. The relationship between initial p[Cd] and Ba uptake rate in uF-uP experiments is shown in Fig. 11a, other experimental conditions are not shown as there was minimal pBa formation. The relationship between initial p[Cd] and Ba uptake rate varies significantly between stations. At Stn A, B, and C, no strong relationship exists. In contrast, Stn D has a positive relationship between initial p[Cd] and Ba uptake rate. Notably, Stn D had p[Cd] that were an order of magnitude larger than p[Cd] at Stns B and C, and two times that see at Stn A. As such, the positive relationship observed at Stn D may arise due to a higher degree of organic complexation of Ba by extra polymeric substances, which have been suggested as a significant concentration mechanism which allows the accumulation of Ba into microenvironments (Martinez-Ruiz et al., 2018; 2021). The association between phosphorous-rich EPS and the abundance of pBa has been observed in the South Atlantic and South Indian Ocean basins in the upper 1000 m of the water column (Martinez-Ruiz et al., 2021). Furthermore, recent work has shown that amorphous Ba-P nanoparticles act as a precursor phase and undergo rapid transformation to crystalline $BaSO_4$ upon contact with sulfate

under abiotic conditions (Ruiz-Agudo et al., 2021). The presence of Ba-P nanoparticles has also been observed in natural samples (Martinez-Ruiz et al., 2019). While assessing the role of these specific particles is outside the scope of this study, it is likely that a similar mechanism operates in the South Pacific Ocean.

The lack of correlation between initial p[Cd] and Ba uptake rate at Stns A and C and negative correlation at Stn B may arise because of the vastly different range over which p[Cd] varies with depth at each station. At Stn D, initial p[Cd] varies by two orders of magnitude from an average value of 0.6 pmol L^{-1} at $z_{ox\text{-}min}$ to 58 pmol L^{-1} at z_{ChL}. In comparison, all other stations vary less, generally ranging between ~0.7 and 20 pmol L^{-1}. The variable relationship between p[Cd] and Ba uptake rate across the transect indicates that the relationship between POM and Ba uptake rate is not clear and other factors may influence the removal of dissolved Ba into the particulate phase or that the relationship is not linear.

Particulate manganese (pMn) was used to assess the role of MnO_x on pBa formation, as MnO_x can complex dissolved Ba^{2+} (Tani et al., 2021; Yokoo et al., in press) and pelagic pMn is typically comprised of mainly MnO_x (70%; Lam et al., 2015). As with pCd, the relationship between pMn and Ba uptake rate can give a sense for the control of pMn mediated Ba complexation on pBa formation in these experiments. The relationship between initial p[Mn] and Ba uptake rate is shown in Fig. 11b. A clear relationship between initial p[Mn] is not evident, indicating that MnO_x are not complexing significant portions of Ba into the particulate phase.

4.4.2 Depth of pBa formation

Previous studies have suggested two main arguments for the depth of pBa formation in the pelagic water column: that pBa forms almost exclusively in the upper 500 m (Chow & Goldberg, 1960; Dehairs et al., 1980; 1990; 1991; 1992; Bishop 1988; Legeleux & Reyss, 1996) or that pBa forms throughout the mesopelagic zone as deep as 2000 m (Van Beek et al., 2007; Van Beek et al., 2009). Most arguments for shallow $BaSO_4$ production are based on observed accumulation of pBa in the upper water column at depths associated with the most intense remineralization of organic matter (Sternberg et al., 2008). Activity ratios of $^{228}Ra/^{226}Ra$, measured in sinking and suspended particles from the Mediterranean Sea have been interpreted to indicate formation of pBa as deep as 2,000 m (van Beek et al., 2007; 2009). Experimental data collected in this study

can help illuminate which of these formation schemes occurs across the transect in the Southern Ocean.

Comparing the uptake rate of dissolved Ba into pBa in uF-uP experiments at each depth indicates that the majority of pBa formation occurs at z_{ChL} (Figs. 5 & 6). At Stn A, the greatest uptake of Ba occurred at $z_{ox\text{-}min}$ at a magnitude of 0.22 nmol L^{-1} d^{-1} in the uF-P experiment. This uptake rate occurred over the first 30 h of the experimental period and was coincident with decrease in $(^{135}Ba{:}^{137}Ba)_{particulate}$ to 0.11, indicating that the Ba taken into the particulate phase was mostly not from the ^{135}Ba-labelled dissolved pool. This may indicate uptake of Ba released from organic matter or other phases known to adsorb Ba, including iron and manganese oxides (Baldermann et al., 2020; Martinez-Ruiz et al., 2019). At all other stations, the greatest uptake rate of Ba occurred at z_{ChL} with a larger magnitude than any rate observed at Stn A, with values of 0.28, 1.23, and 7.45 nmols L^{-1} d^{-1} at Stns B , C , and D , respectively. Similar increases in the uptake rate of Ba were observed at $z_{max\text{-}deg}$ and $z_{ox\text{-}min}$, although Ba uptake rates at depth had magnitudes that were only 10 % of the surface value. Based on these results, it is evident that while pBa forms throughout the upper 1000 m of water column in the Pacific Sector of the Southern Ocean, the majority of pBa forms above 70 m, where biological productivity, and presumably organic matter recycling, is high.

4.4.3 Implications for regional Ba budgets

The theoretical pBa rain rate may be calculated from experimental Ba uptake rates by integrating over depth and accounting for pBa remineralization. Rates measured at z_{ChL} and $z_{max\text{-}deg}$ were applied to 50 m of water column surrounding their respective depths, with the uptake rate at $z_{ox\text{-}min}$ accounting for the remainder of the uptake. Values were integrated over the top 600 m of the water column to allow comparison with sediment trap data from the Southern Ocean, although no data exist for $BaSO_4$ rain rate in the Pacific sector of the Southern Ocean (Jacquet et al., 2007). A mesopelagic export efficiency (f_{export}) of pBa of 0.03 was applied based off the remineralization of pBa measured under a phytoplankton bloom in the Southern Ocean (0-600 m; Dehairs et al., 1997). As such, the drawdown of Ba into the particulate phase was used to approximate the pBa rain rate, where

$$\text{Ba rain rate } (\mu\text{mol m}^{-2}\ \text{d}^{-1}) = \Sigma\ z_i * (\text{Ba Uptake Rate}) * f_{export}. \quad (3)$$

Following this formulation, the pBa rain rate was estimated as 1.1 μmol m^{-2} d^{-1} at Stn A and 16.3 μmol m^{-2} d^{-1} at Stn D. The rates at Stn A are similar to those of pBa accumulation measured in sediment traps deployed in the Sub-Antarctic Zone and Sub-Antarctic Front (0.86 and 1.32 μmol m^{-2} d^{-1}, respectively), but those at Stn D are one order of magnitude higher than those measured in the PFZ (1.06 μmol m^{-2} d^{-1}; Jacquet et al., 2007). This mismatch may reflect temporal variability, such as seasonality, in pBa production or f_{export}, or may indicate that pBa formation rates calculated using Eq. (3) are not directly comparable with pBa fluxes determined from sediment traps. The observed latitudinal trends in the Ba rain rate across the frontal region speak to an open controversy regarding the controls on Ba cycling in the ocean.

The cycling of $BaSO_4$ in the water column, overlaid with global circulation dynamics, largely accounts for the oceanic distribution of d[Ba] (Horner et al., 2015; Bates et al., 2017; Horner & Crockford, 2021). Two conceptualizations exist for how this interplay leads to the observed d[Ba] distribution in the ocean. Of the two, the more classical paradigm posits that the distribution of d[Ba], as well as other moieties affected by significant particulate carriers (d[Si] and alkalinity), arises from similarities in the remineralization length scale of the major particulate carrier phases (barite, diatom opal, and calcium carbonate, respectively; Broecker and Peng T-H, 1982). Under this localized model, vertical profiles of these properties are maintained through formation of the particulate phase in the surface, which then survives to greater depths before succumbing to dissolution, in comparison to labile P and N, which are largely recycled in the surface ocean. While this view is appealing because of its simplicity, studies of high-latitude Si and alkalinity cycling paint a more complex picture. Specifically, subsequent studies suggested that Si (Sarmiento et al., 2004) and alkalinity (Krumhardt et al., 2020) are more intensely drawn down than nitrate or phosphate in the high-latitude Southern Ocean, particularly in the Polar Front Zone (PFZ; between the PF and SAF). Since the PFZ is a significant region for intermediate and mode water formation, waters forming in the PFZ will be strongly depleted in preformed Si and alkalinity. These depletions are subsequently carried into the low latitudes, where they give rise to the apparent deeper regeneration profiles for Si and alkalinity. Horner et al. (2015) recently proposed an analogous mechanism for Ba, whereby d[Ba] is drawn down by pBa formation in the PFZ, leading to Ba-depleted intermediate and mode waters. Barium isotope data from the North

and South Atlantic are consistent with high latitude processes producing the major features of d[Ba] distributions made (Horner et al., 2015; Bates et al., 2017). The latitudinal trends observed in Ba rain rate described here offer the first direct evidence for high-latitude control of global Ba cycling. Increases in the Ba rain rate both inside of the PFZ suggest that the intermediate and mode waters forming in the PFZ are depleted in d[Ba] due to the removal of pBa, in agreement with the high-latitude cycling model proposed by Sarmiento et al. (2004).

4.5 Conclusions

The findings that particulate barium formation occurs largely at depths shallower than 70 m, increases significantly in the PFZ, and requires both active microbial communities and POM >5 μm have two major implications for interpreting the formation, global distribution, and chemical composition of pBa in the sedimentary record. First, the data resolve, at least in the study region, the question of where pBa forms in the water column. Rates of pBa formation decrease dramatically with depth, with virtually no formation at 1,000 m. The depth of formation, in combination with the need for both microbial activity and large aggregates, is consistent with the microenvironment-mediated model in which heterotrophic oxidation of sinking organic matter promotes pBa formation (Chow & Goldberg, 1960). The $BaSO_4$ fraction of pBa has been used extensively as a record of sulfur (Kusakabe and Robinson, 1977; Paytan et al., 1998, 2004), strontium (Reesman, 1968; Paytan et al., 2002), and barium (Horner et al., 2017; Bridgestock et al., 2018; Bridgestock et al., 2019; Crockford et al., 2019) isotopes, as the composition of $BaSO_4$ reflects the formation fluid. As such, our data indicate that newly formed pelagic $BaSO_4$ records the isotopic composition of these elements from the surface ocean.

Secondly, the data presented here are consistent with the high-latitude cycling model for global Ba, implying that pBa in the sedimentary record is sensitive to changes in high-latitude circulation dynamics. Therefore, we suggest that the distribution of sedimented pBa may offer insight into Earth history events shaping the hydrographic regime of the PFZ. Sediment records spanning the Eocene-Oligocene Transition (EOT) suggest that dramatic shifts in BaAR occurred and may be related to changes in the geometry of the PFZ due to the opening of the Drake Passage and the Tasman Gate (Moore et al., 2014). Generally, high-latitude circulation, in combination with increased pBa formation with larger standing stocks of POM, agrees well with models describing

the joint control of biological productivity and circulation on observed d[Ba] (Horner & Crockford, 2021). These processes may be separated by their relative length scales, as biological productivity may change on relatively short timescales compared to global ocean circulation.

The results of this study do not resolve the open question as to the specific controls on pBa formation. To that end, we suggest future experimental work using similar designs with larger volumes of water, to allow accurate analysis of p[P], p[Al], p[Ti], and other useful tracers of organic and lithogenic components. In addition, experimental work testing the specific fractions of POM, particularly components of EPS (Martinez-Ruiz et al., 2018; 2021), would allow more specific classification of the controls leading to increased pBa formation.

Acknowledgements

Thanks to the Woods Hole Oceanographic Institution – Ocean Ventures Fund for funding grants to J.T.M. which allowed much of this work to be carried out. Salary support for J.T.M was provided by NSF OCE-2023456 to T.J.H. Special thanks to the crew of the R/V Roger Revelle on cruise RR2004 for getting us down into the waters of the Polar Frontal Zone with only minor delays for icebergs, and to the Scripps Institute for Oceanography for coordinating cruise preparation in the time of COVID-19.

Figures and Tables

Table 1

Experimental sites and water depths. The saturation state (Ω_{barite}) is defined as $\Omega_{barite} = [Ba][SO_4]/k_{sp,barite}$.

Station	Station ID	Lat	Long	Depth feature	Depth (m)	$[Ba]_{in\ situ}$ (nmol L^{-1})	±2SE	$[^{135}Ba]$ addition (nmol L^{-1})	Ω_{barite}
RR2004 -098	A	-44.865	-149.999	z_{ChL}	30	70	5	120	1.53
				$z_{max\text{-}deg}$	47	51	4	115	1.44
				$z_{ox\text{-}min}$	1000	72	5	78	1.34
RR2004 -039	B	-48.332	-150	z_{ChL}	50	41	3	123	0.99
				$z_{max\text{-}deg}$	60	41	3	115	0.94
				$z_{ox\text{-}min}$	1000	57	4	84	1.12
RR2004 -083	C	-54.163	-142.551	z_{ChL}	60	55	4	98	1.23
				$z_{max\text{-}deg}$	80	51	4	97	1.29
				$z_{ox\text{-}min}$	1000	95	7	23	1.06
RR2004 -056	D	-55.332	-150	z_{ChL}	50	73	5	116	1.57
				$z_{max\text{-}deg}$	75	64	4	101	1.49
				$z_{ox\text{-}min}$	1000	83	6	22	0.96

Fig. 1 A representative profile of p[Ba] in the water column taken from the GEOTRACES Intermediate Data Product 2017 v2, GP-16 transect at Station 36B .

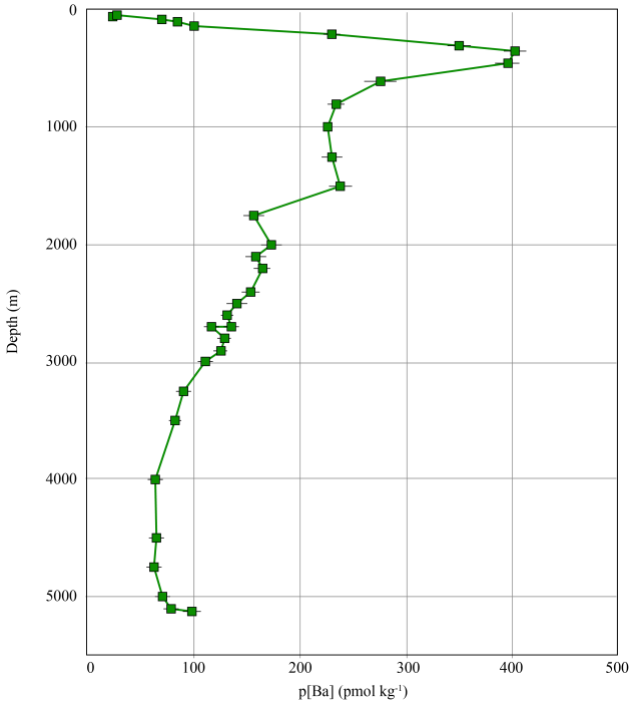

Fig. 2 Map of stations at which pBa formation experiments were carried out. Frontal regions are modified from Talley (2013), with the Sub-Tropical Front (STF), Sub-Antarctic Front (SAF), and Polar Front (PF) shown.

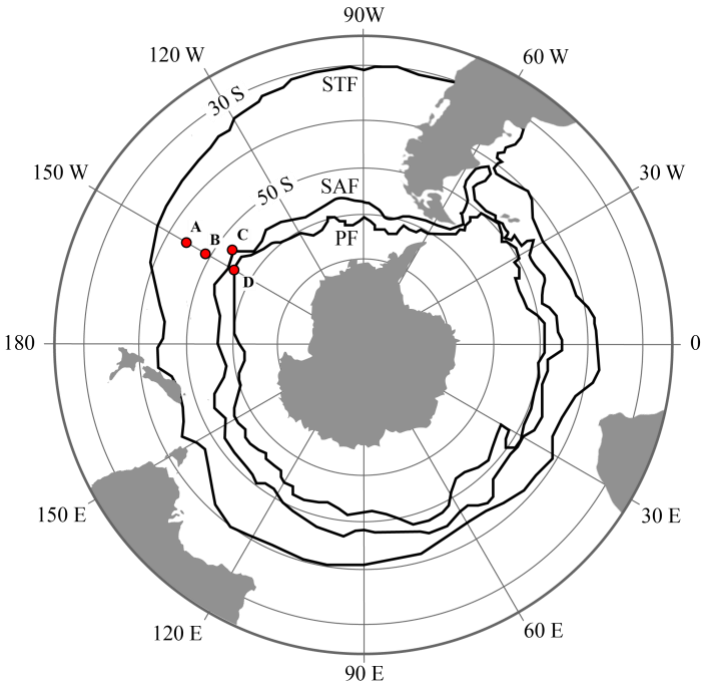

Fig. 3 Schematic of the experimental setup carried out at each depth in the water column.

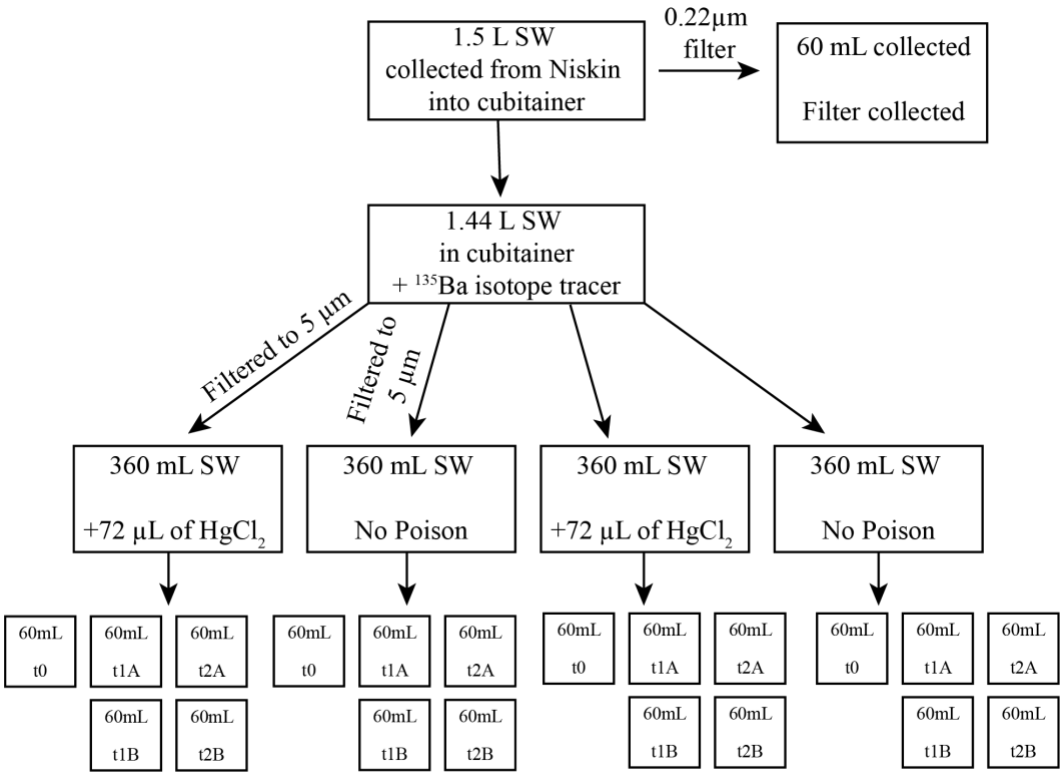

Fig. 4 Particulate barium concentration over the duration of each experiment. Shading indicates depth, with the lightest of each color indicating the z_{ChL} and the darkest color indicating the $z_{ox\text{-}min}$.

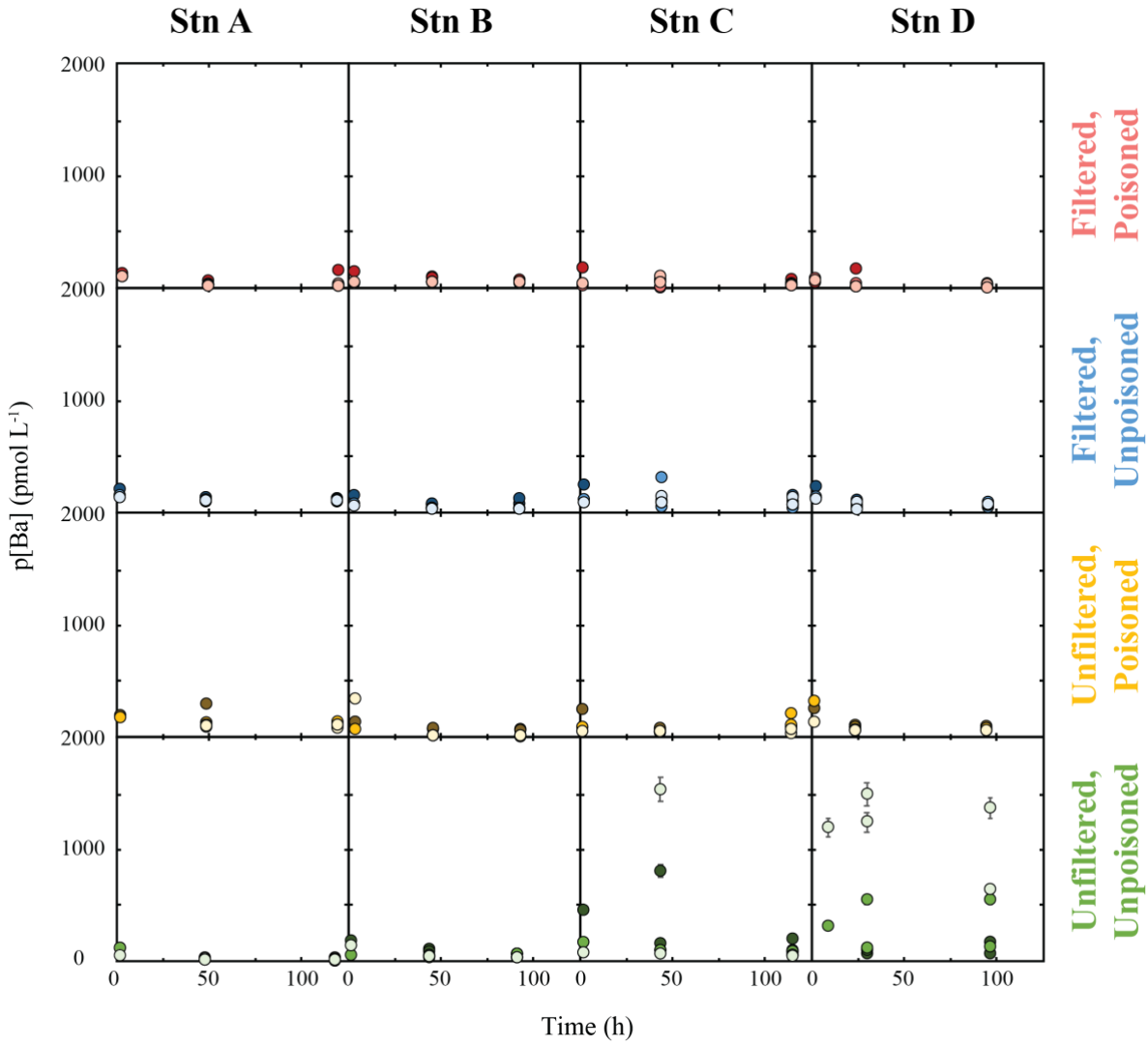

Fig. 5 Variations in $(^{135}Ba:^{137}Ba)_{particulate}$ for each experiment. Error bars represent the variation between replications at a time point. As the fluid was labelling with ^{135}Ba, formation of new pBa from the dissolved pool is indicated by increases in $(^{135}Ba:^{137}Ba)_{particulate}$ from the initial value, while decreases in $(^{135}Ba:^{137}Ba)_{particulate}$ from the initial value indicate formation of pBa using a non-dissolved source of Ba. Shading indicates depth, with the lightest of each color indicating the z_{ChL} and the darkest color indicating the $z_{ox\text{-}min}$.

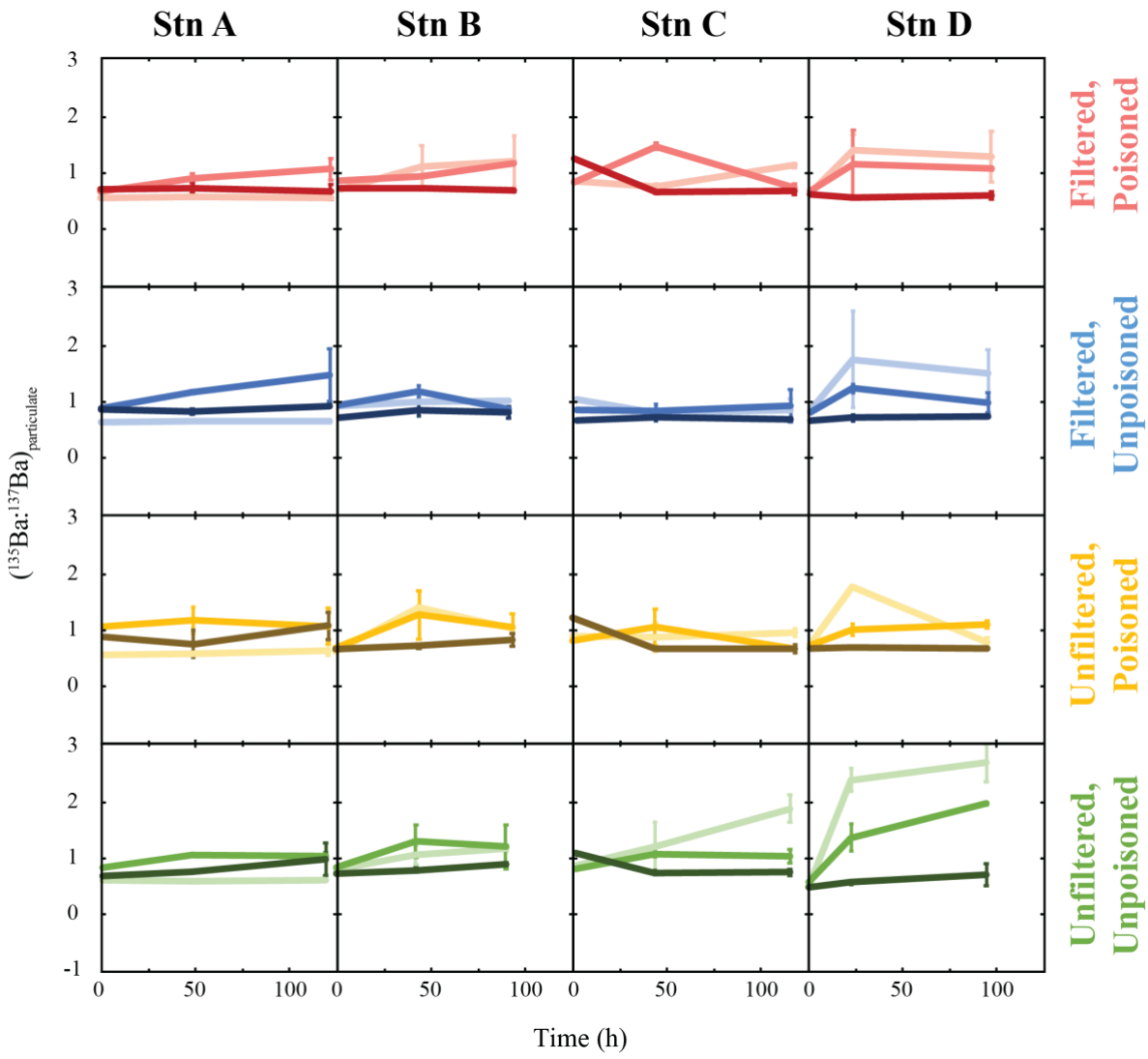

Fig. 6 Variations in $(^{135}Ba:^{137}Ba)_{particulate}$ for each experiment with the initial $(^{135}Ba:^{137}Ba)_{particulate}$ value subtracted. As such, positive values indicate formation of new pBa from the dissolved pool, while negative values indicate formation of pBa using a non-dissolved source of Ba. The grey bar represents the uncertainty of the $(^{135}Ba:^{137}Ba)_{particulate}$ measurement. Shading indicates depth, with the lightest of each color indicating the z_{ChL} and the darkest color indicating the $z_{ox\text{-}min}$.

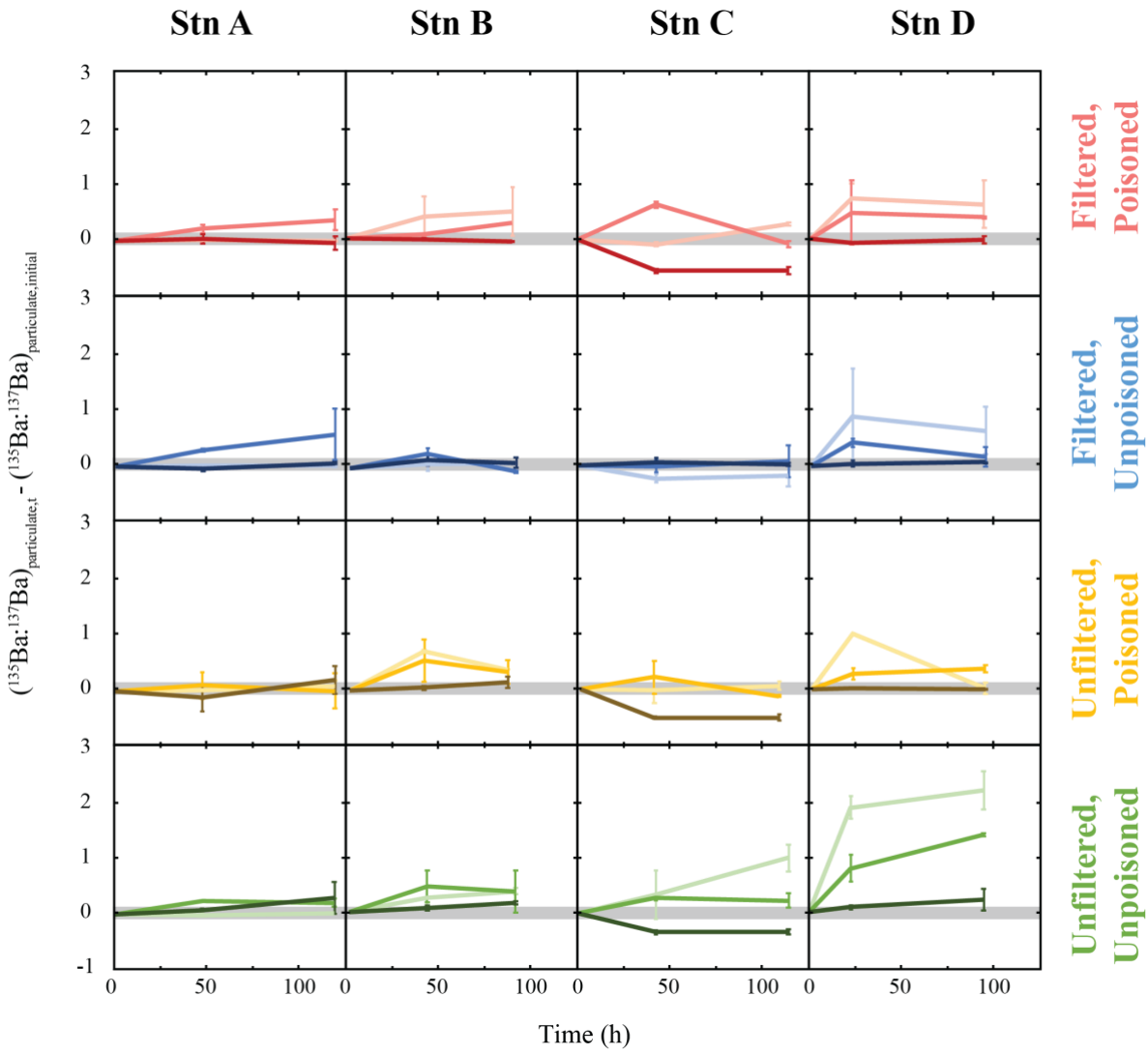

Fig. 7 Ba Uptake Rate for each experiment. Shading indicates depth, with the lightest of each color indicating the z_{ChL} and the darkest color indicating the $z_{ox\text{-}min}$.

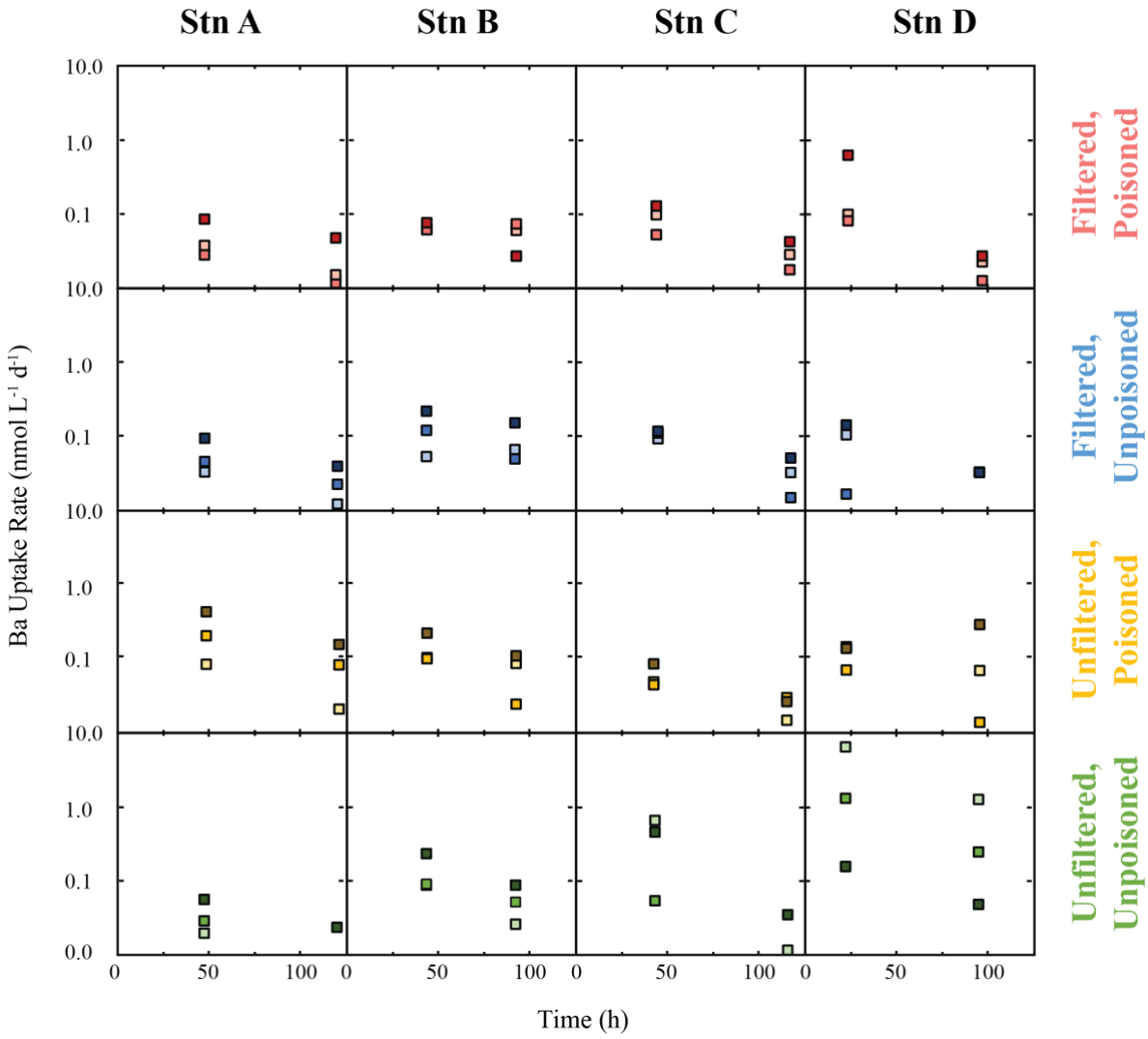

Fig. 8 Particulate yttrium (Y), a tracer of lithogenic inputs, across the transect. Particulate Y was invariant amongst experimental conditions. Here, the average p[Y] for each station is plotted.

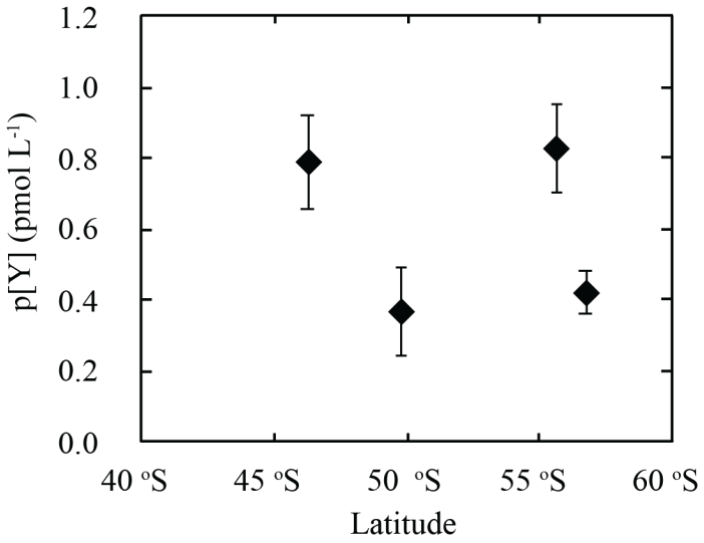

Fig. 9 Initial p[Cd] in each experiment, which is correlated with the amount of particulate organic matter in the water column. Shading indicates depth, with the lightest of each color indicating the z_{ChL} and the darkest color indicating the $z_{ox\text{-}min.}$

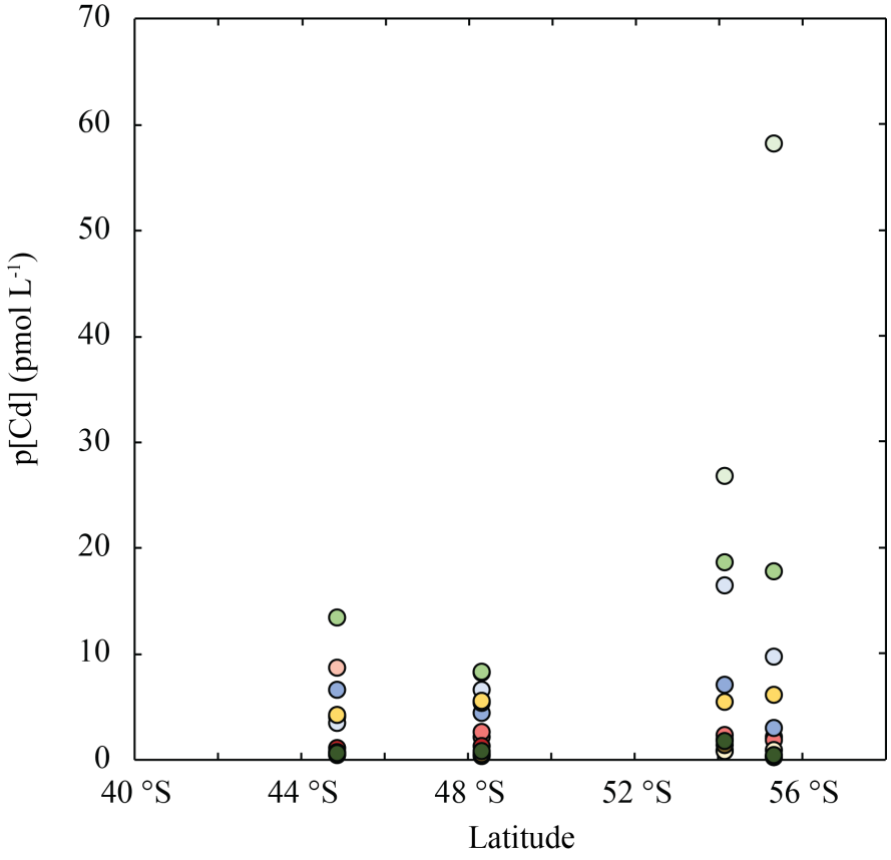

Fig. 10 Particulate manganese, a tracer of manganese oxides. Shading indicates depth, with the lightest of each color indicating the z_{ChL} and the darkest color indicating the $z_{ox\text{-}min}$.

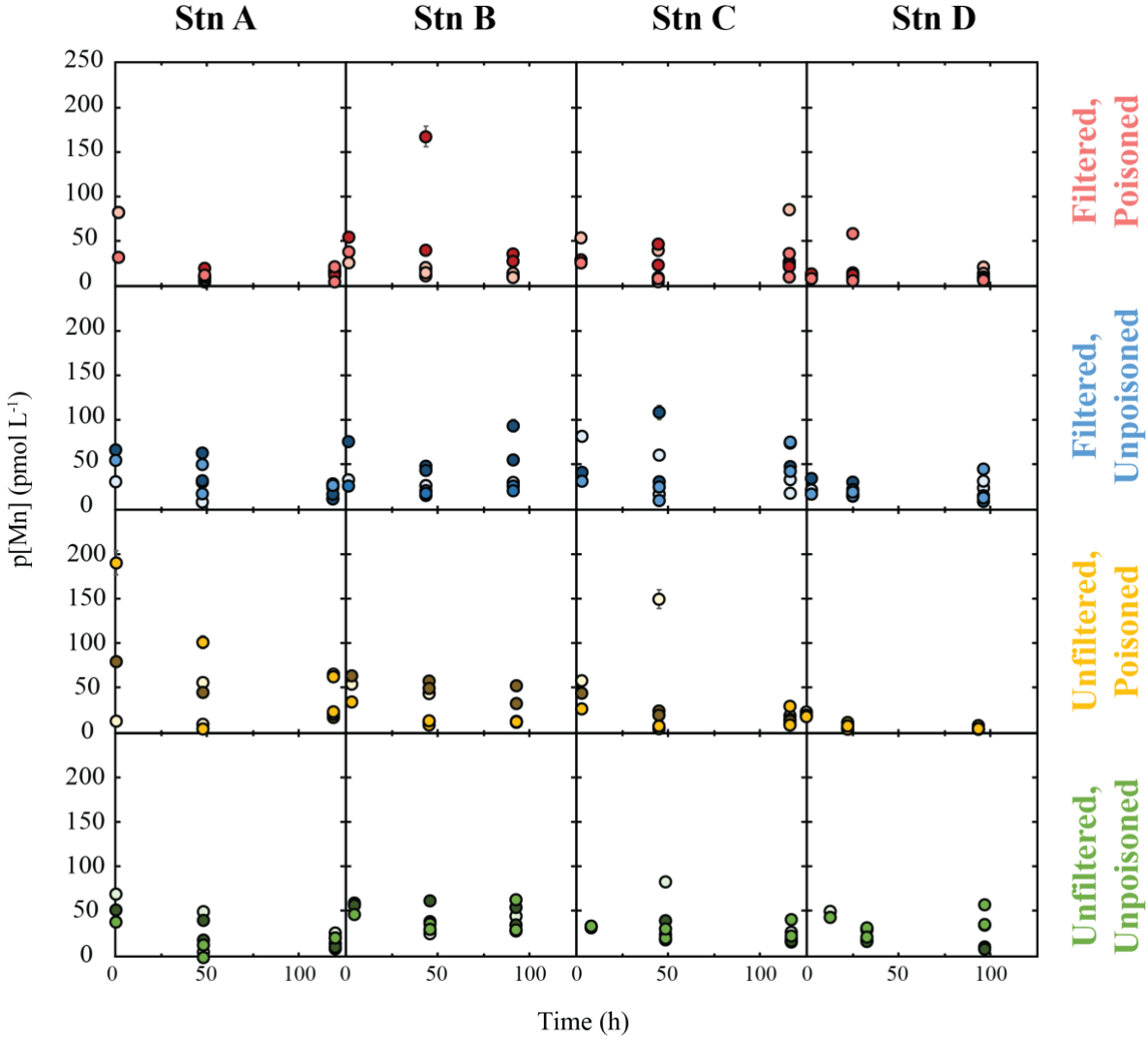

Fig. 11 Initial (a) p[Cd] and (b) p[Mn] plotted against Ba uptake rate calculated at the first time point. Stations are shown left to right: A, B, C, D. Shading indicates depth, with the lightest of each color indicating the z_{ChL} and the darkest color indicating the $z_{ox\text{-}min}$.

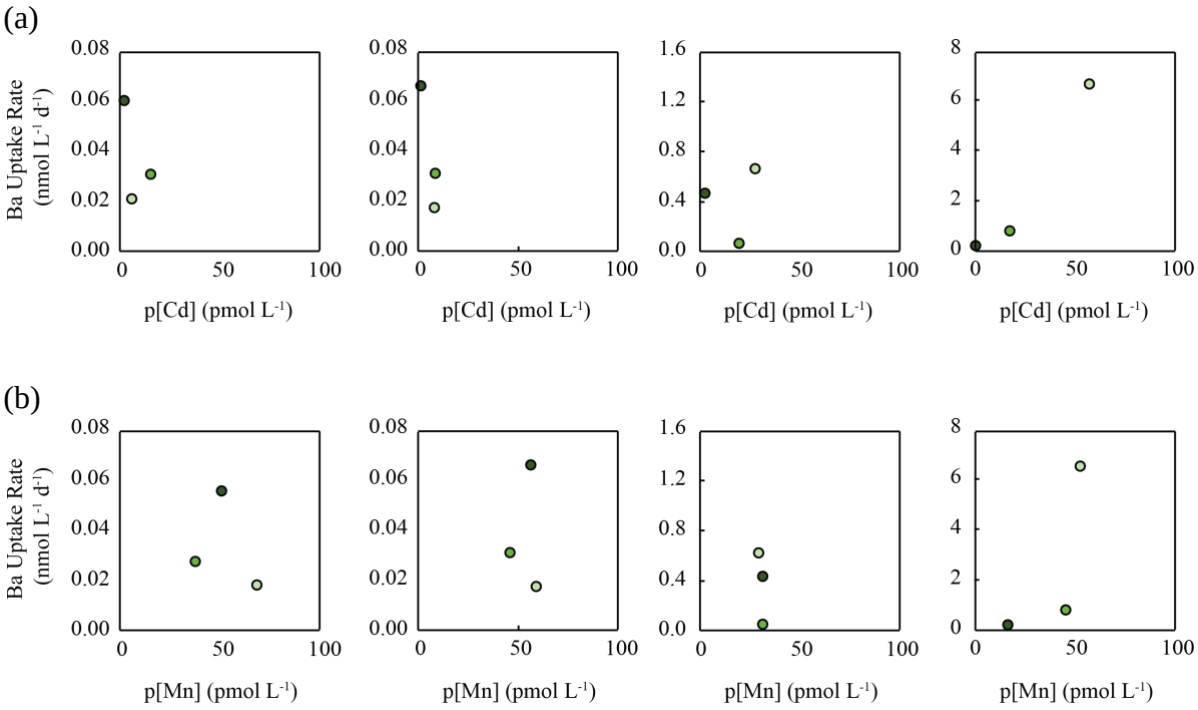

Chapter 5: Conclusions and future outlooks

This thesis provides new constrains on processes impacting the isotopic signature and distribution of barium in the ocean to improve future climate reconstructions using related Ba, based paleoproxies. I characterize the previously unconstrained process of ion exchange between Ba and $BaSO_4$ in marine settings through a combination of laboratory experiments, evaluation of environmental records, and modelling (Ch. 2 – 3). Following this, I clarify the depth and spatial distribution of particulate barium formation in the South Pacific Ocean and expand the understanding of the role of large aggregates and microbial activity on this process (Ch. 4).

In Chapter 2, the rate and magnitude of Ba isotope fractionation associated with ion exchange between Ba in artificial seawater and synthetic $BaSO_4$ were characterized using laboratory experiments. The rate of ion exchange falls between 4 and 37 pmol m^{-2} s^{-1} and is consistent with previous studies (Curti et al., 2010; Torapava et al., 2014; Brandt et al., 2015; Heberling et al., 2018). This rate represents the convergence of the forward (precipitation) and back (dissolution) reactions, which operate at equal and opposite magnitudes at chemical equilibrium (Zhen-Wu et al., 2016; Heberling et al., 2018; Vital et al., 2020). The combined effects of $BaSO_4$ dissolution ($\Delta^{138}Ba_{barite\text{-}dBa}$ = +0.22 ± 0.05‰) and precipitation (-0.32 ‰; Von Allmen et al., 2010), leads to an ion-exchange mediated the observed $\Delta^{138}Ba_{barite–Ba(aq)}$ = -0.10 ± 0.05 ‰. These findings suggest the isotopic composition of Ba in geologic $BaSO_4$ records may not be fixed following their original precipitation, and may reflect some resetting during deposition and burial. The degree to which the primary isotopic signature is overprinted in $BaSO_4$ will depend on the magnitude of L_{barite}, the degree to which these phases are out of isotopic equilibrium, the reactivity of environmental $BaSO_4$, and the supply of new dissolved Ba to pore fluids. Similarly, as the isotopic composition of the fluid phase is strongly influenced by interactions with coexisting $BaSO_4$ over relatively short time periods, it seems unlikely that flowing pore fluids preserve pristine records. Accounting for the impact of ion exchange is critical when reconstructing changes in oceanic carbon export using Ba isotope based paleoproxies.

Chapter 3 expands on the impacts of ion exchange to investigate the role of this process in pore fluids and sedimented $BaSO_4$ in the Equatorial Pacific. This chapter provided another independent constraint on the rate of ion exchange and the magnitude of associated isotopic fractionation. Environmental data indicated rates of ion exchange between 0.03 and 0.57 pmol

m^{-2} s^{-1} between pore fluids and co-located $BaSO_4$, indicating that environmental factors decrease the rate at which the process occurs. The magnitude of isotopic fractionation related to dissolution was found to be of a similar value to the findings of Chapter 2, with $\Delta^{138}Ba_{barite\text{-}dBa}$ = +0.15 ‰. The resultant observed $\Delta^{138}Ba_{barite\text{-}dBa}$ between pore fluids and $BaSO_4$, when accounting for the magnitude of precipitation-related fractionation as defined by Von Allmen et al. (2010), was -0.17 ‰. As such, care should be taken to account for ion-exchange-mediated isotopic fractionation impacting $\delta^{138}BaSO_4$ recorded in the geologic record, as post-depositional changes may occur. We provide constraints on site selection which mitigate the impact of ion exchange and represent sediment records where the primary signature of $\delta^{138}BaSO_4$ is likely to be preserved. For site with a similar degree of isotopic disequilibrium between pore fluids and sedimented $BaSO_4$, L_{barite} > 0.78 satisfy this criteria, though we note that it is unlikely that sites with flowing natural fluids preserve unaltered records of the origin of these fluids, as such flow through significantly decreases L_{barite}. When interpreting $\delta BaSO_4$ in sediments with poor constraints on L_{barite} and fluid flow, variations of < 0.17 ‰ should be interpreted with caution as they fall within the range of variation allowable solely by ion exchange.

In Chapter 4, the high-level controls on and depth of formation, as well as the spatial distribution of particulate barium (pBa) formation are investigated to discriminate between the two prevailing oceanic cycling models proposed for Ba. We find that pBa formation requires both microbial activity and pre-existing particles >5 µm. These consistent with the microenvironment model of formation (Chow & Goldberg, 1960), although they do not resolve the open question as the specific controls on pBa formation. Particulate barium was found to form at depths shallower than 70 m and increases significantly in the Polar Frontal Zone (PFZ). and The data resolve, at least in the South Pacific Ocean, the question of where pBa forms in the water column: rates of pBa formation decrease dramatically with depth, with virtually no formation at 1,000 m. The increase in pBa formation across the PFZ is consistent with the high-latitude cycling model, implying that changes in pBa in the sedimentary record may provide insights into changes in high-latitude circulation dynamics.

Overall, this thesis highlights the importance of investigating the formation of $BaSO_4$ and processes effecting $\delta^{138}BaSO_4$ during deposition and burial. These parameters are critical for accurately interpreting paleoproxies related to the accumulation rate of $BaSO_4$ in the sediments and the isotopic signature of Ba imparted in the sedimented mineral. Future work investigating the

impact of ion exchange on other elements recorded in $BaSO_4$, particularly the chemically similar strontium and radium, will act to further clarify the extent of ion-exchange-mediated alteration of $BaSO_4$ in the marine sediment record.

References

von Allmen K., Böttcher M. E., Samankassou E. and Nägler T. F. (2010) Barium isotope fractionation in the global barium cycle: First evidence from barium minerals and precipitation experiments. *Chemical Geology* **277**, 70–77.

Aoki M., Miyashita Y., Tran P. T., Okuno Y., Watari T. and Yamaguchi T. (2021) Enrichment of marine manganese-oxidizing microorganisms using polycaprolactone as a solid organic substrate. *Biotechnology Letters* **43**, 813–823.

Arnarson T. S. and Keil R. G. (2001) Organic-mineral interactions in marine sediments studied using density fractionation and X-ray photoelectron spectroscopy. *Organic Geochemistry* **32**, 1401–1415.

Avrahamov N., Sivan O., Yechieli Y. and Lazar B. (2013) Carbon Isotope Exchange During Calcite Interaction With Brine: Implications for 14 C Dating of Hypersaline Groundwater . *Radiocarbon* **55**, 81–101.

Bains S., Norris R. D., Corfueld R. M. and Faul K. L. (2000) Termination of global warmth at the Palaeocene/Eocene boundary through productivity feedback. *Nature* **407**, 171–174.

Balch W. M., Bowler B. C., Drapeau D. T., Lubelczyk L. C., Lyczkowski E., Mitchell C. and Wyeth A. (2019) Coccolithophore distributions of the North and South Atlantic Ocean. *Deep-Sea Research Part I: Oceanographic Research Papers* **151**.

Baldermann A., Fleischhacker Y., Schmidthaler S., Wester K., Nachtnebel M. and Eichinger S. (2020) Removal of barium from solution by natural and iron(III) oxide-modified allophane, beidellite and zeolite adsorbents. *Materials* **13**.

Bates S. L., Hendry K. R., Pryer H. v., Kinsley C. W., Pyle K. M., Woodward E. M. S. and Horner T. J. (2017) Barium isotopes reveal role of ocean circulation on barium cycling in the Atlantic. *Geochimica et Cosmochimica Acta* **204**, 286–299.

van Beek P., François R., Conte M., Reyss J. L., Souhaut M. and Charette M. (2007) 228Ra/226Ra and 226Ra/Ba ratios to track barite formation and transport in the water column. *Geochimica et Cosmochimica Acta* **71**, 71–86.

van Beek P., Sternberg E., Reyss J. L., Souhaut M., Robin E. and Jeandel C. (2009) 228Ra/226Ra and 226Ra/Ba ratios in the Western Mediterranean Sea: Barite formation and transport in the water column. *Geochimica et Cosmochimica Acta* **73**, 4720–4737.

Bernstein R. E. and Byrne R. H. (2004) Acantharians and marine barite. *Marine Chemistry* **86**, 45–50.

Bishop J. K. B. (1988) The barite-opal-organic carbon association in oceanic particulate matter. *Nature* **332**, 341–343.

Blake R. E., Surkov A. v., Böttcher M. E., Ferdelman T. G. and Jørgensen B. B. (2006) Oxygen isotope composition of dissolved sulfate in deep-sea sediments: Eastern equatorial Pacific Ocean. *Proceedings of the Ocean Drilling Program: Scientific Results* **201**.

Bonn W. J., Gingele F. X., Grobe H., Mackensen A., Ffitterer D. K. and Alfred " (1998) Palaeoproductivity at the Antarctic continental margin: opal and barium records for the last 400 ka. *Palaeogeography, Palaeoclimatology, Palaeoecology* **139**, 211.

Bosbach D., Böttle M. and Metz Karlsruher V. (2010) *Experimental study on Ra2+ uptake by barite (BaSO4).*, Stockholm, Sweden.

Böttcher M. E., Neubert N., von Allmen K., Samankassou E. and Nägler T. F. (2018) Barium isotope fractionation during the experimental transformation of aragonite to witherite and of gypsum to barite, and the effect of ion (de)solvation. *Isotopes in Environmental and Health Studies* **54**, 324–335.

Bowie A. R., Lannuzel D., Remenyi T. A., Wagener T., Lam P. J., Boyd P. W., Guieu C., Townsend A. T. and Trull T. W. (2009) Biogeochemical iron budgets of the Southern Ocean south of Australia: Decoupling of iron and nutrient cycles in the subantarctic zone by the summertime supply. *Global Biogeochemical Cycles* **23**.

Bracco J. N., Lee S. S., Stubbs J. E., Eng P. J., Heberling F., Fenter P. and Stack A. G. (2017) Hydration Structure of the Barite (001)-Water Interface: Comparison of X-ray Reflectivity with Molecular Dynamics Simulations. *Journal of Physical Chemistry C* **121**, 12236–12248.

Brandt F., Curti E., Klinkenberg M., Rozov K. and Bosbach D. (2015) Replacement of barite by a (Ba,Ra)SO4 solid solution at close-to-equilibrium conditions: A combined experimental and theoretical study. *Geochimica et Cosmochimica Acta* **155**, 1–15.

Breit G. N., Simmons E. C. and Goldhaber M. B. (1985) Dissolution of barite for the analysis of strontium isotopes andother chemical and isotopic variations using aqueous sodium carbonate. *Chemical Geology* **52**, 333–336.

Bridgestock L., Hsieh Y. te, Porcelli D. and Henderson G. M. (2019) Increased export production during recovery from the Paleocene–Eocene thermal maximum constrained by sedimentary Ba isotopes. *Earth and Planetary Science Letters* **510**, 53–63.

Bridgestock L., Hsieh Y. te, Porcelli D., Homoky W. B., Bryan A. and Henderson G. M. (2018) Controls on the barium isotope compositions of marine sediments. *Earth and Planetary Science Letters* **481**, 101–110.

Bridgestock L., Nathan J., Paver R., Hsieh Y. te, Porcelli D., Tanzil J., Holdship P., Carrasco G., Annammala K. V., Swarzenski P. W. and Henderson G. M. (2021) Estuarine processes modify the isotope composition of dissolved riverine barium fluxes to the ocean. *Chemical Geology* **579**.

Broecker W. S. and Peng T-H (1982) *Tracers in the sea*., Lamont-Doherty Geological Observatory, Columbi University, Palisades, NY.

Buesseler K. O., Lamborg C. H., Boyd P. W., Lam P. J., Trull T. W., Bidigare R. R., Bishop J. K. B., Casciotti K. L., Dehairs F., Elskens M., Honda M., Karl D. M., Siegel D. A., Silver M. W., Steinberg D. K., Valdes J., Mooy B. van and Wilson S. (2007) Revisiting Carbon Flux Through the Ocean's Twilight Zone Downloaded from. *Science (1979)* **316**, 567–570.

Cao Z., Li Y., Rao X., Yu Y., Hathorne E. C., Siebert C., Dai M. and Frank M. (2020) Constraining barium isotope fractionation in the upper water column of the South China Sea. *Geochimica et Cosmochimica Acta* **288**, 120–137.

Cardinal D., Dehairs F., Cattaldo T. and André L. (2001) Geochemistry of suspended particles in the Subantarctic and Polar Frontal Zones south of Australia: Constraints on export and advection processes. *Journal of Geophysical Research: Oceans* **106**, 31637–31656.

Carter S. C., Griffith E. M. and Penman D. E. (2016) Peak intervals of equatorial Pacific export production during the middle Miocene climate transition. *Geology* **44**, 923–926.

Carter S. C., Paytan A. and Griffith E. M. (2020) Toward an improved understanding of the marine barium cycle and the application of marine barite as a paleoproductivity proxy. *Minerals* **10**.

Chan L. H., Drummond D., Edmondt J. M. and Grant~ B. (1977) On the barium data from the Atlantic GEOSECS Expedition. *Deep Sea Research* **24**, 613–649.

Chanda P., Gorski C. A., Oakes R. L. and Fantle M. S. (2019) Low temperature stable mineral recrystallization of foraminiferal tests and implications for the fidelity of geochemical proxies. *Earth and Planetary Science Letters* **506**, 428–440.

Charbonnier Q., Moynier F. and Bouchez J. (2018) Barium isotope cosmochemistry and geochemistry. *Science Bulletin* **63**, 385–394.

Charette M. A., Sholkovitz E. R. and Hansel C. M. (2005) Trace element cycling in a subterranean estuary: Part 1. Geochemistry of the permeable sediments. *Geochimica et Cosmochimica Acta* **69**, 2095–2109.

Chow T. J. and Goldberg E. D. (1960) On the marine geochemistry of barium. *Geochimica et Cosmochimica Acta* **20**, 192–198.

Church T. M. and Bernat M. (1972) Thorium and uranium in marine barite. *Earth and Planetary Science Letters* **14**, 139–144.

Church T. M. and Wolgemuth K. (1972) Marine barite saturation. *Earth and Planetary Science Letters* **15**, 35–44.

Cloete R., Loock J. C., van Horsten N. R., Fietz S., Mtshali T. N., Planquette H. and Roychoudhury A. N. (2021) Winter Biogeochemical Cycling of Dissolved and Particulate Cadmium in the Indian Sector of the Southern Ocean (GEOTRACES GIpr07 Transect). *Front Mar Sci* **8**.

Collier R. and Edmond J. (1984) The Trace Element Geochemistry of Marine Biogenic Particulate Matter. *Progress in Oceanography* **13**, 113–199.

Cowen J. P. and Bruland K. W. (1985) Metal deposits associated with bacteria: implications for Fe and Mn marine biogeochemistry. *Deep Sea Research* **32**, 253–272.

Cox A. D., Noble A. E. and Saito M. A. (2014) Cadmium enriched stable isotope uptake and addition experiments with natural phytoplankton assemblages in the Costa Rica Upwelling Dome. *Marine Chemistry* **166**, 70–81.

Crockford P. W., Kunzmann M., Bekker A., Hayles J., Bao H., Halverson G. P., Peng Y., Bui T. H., Cox G. M., Gibson T. M., Wörndle S., Rainbird R., Lepland A., Swanson-Hysell N. L., Master S., Sreenivas B., Kuznetsov A., Krupenik V. and Wing B. A. (2019) Claypool continued: Extending the isotopic record of sedimentary sulfate. *Chemical Geology* **513**, 200–225.

Curti E., Fujiwara K., Iijima K., Tits J., Cuesta C., Kitamura A., Glaus M. A. and Müller W. (2010) Radium uptake during barite recrystallization at 23±2°C as a function of solution composition: An experimental 133Ba and 226Ra tracer study. *Geochimica et Cosmochimica Acta* **74**, 3553–3570.

Curti E., Kulik D. A. and Tits J. (2005) Solid solutions of trace Eu(III) in calcite: Thermodynamic evaluation of experimental data over a wide range of pH and pCO2. *Geochimica et Cosmochimica Acta* **69**, 1721–1737.

Cutter G., Casciotti K., Croot P., Geibert W., Heimbürger L.-E., Lohan M., Planquette H. and van de Flierdt T. (2017) *Sampling and Sample-handling Protocols for GEOTRACES Cruises. Version 3, August 2017.*, Toulouse, France.

Dean W. E., Gardner J. v. and Piper D. Z. (1997) Inorganic geochemical indicators of glacial-interglacial changes in productivity and anoxia on the California continental margin. *Geochimica et Cosmochimica Acta* **61**, 4507–4518.

Dehairs F., Baeyens W. and Goeyens L. (1992) Accumulation of Suspended Barite at Mesopelagic Depths and Export Production in the Southern Ocean. *Science (1979)* **258**, 1332–1335.

Dehairs F., Chesselet R. and Jedwab J. (1980) Discrete suspended particles of barite and the barium cycle in the open ocean. *Earth and Planetary Science Letters* **49**, 528–550.

Dehairs F., Shopova D., Ober S., Veth C. and Goeyens L. (1997) Particulate barium stocks and oxygen consumption in the Southern Ocean mesopelagic water column during spring and early summer: relationship with export production. *Deep-Sea Research* **44**, 497–516.

Dehairs F., Stroobants N. and Goeyens L. (1991) Suspended barite as a tracer of biological activity in the Southern Ocean. *Marine Chemistry* **35**, 399–410.

Deng N., Stack A. G., Weber J., Cao B., de Yoreo J. J. and Hu Y. (2019) Organic–mineral interfacial chemistry drives heterogeneous nucleation of Sr-rich (Bax, Sr1−x)SO4 from undersaturated solution. *Proc Natl Acad Sci U S A* **116**, 13221–13226.

Druhan J. L., Steefel C. I., Williams K. H. and DePaolo D. J. (2013) Calcium isotope fractionation in groundwater: Molecular scale processes influencing field scale behavior. *Geochimica et Cosmochimica Acta* **119**, 93–116.

Dymond J. and Collier R. (1996) Particulate barium fluxes and their relationships to biological productivity. *Deep-Sea Research II* **43**, 1283–1308.

Dymond J., Lyle M. and York N. (1992) Barium in deep-sea sediment: A geochemical proxy for paleoproductivity. *Paleoceanography* **7**, 163–181.

Eagle M., Paytan A., Arrigo K. R., van Dijken G. and Murray R. W. (2003) A comparison between excess barium and barite as indicators of carbon export. *Paleoceanography* **18**.

Erhardt A. M., Pälike H. and Paytan A. (2013) High-resolution record of export production in the eastern equatorial Pacific across the Eocene-Oligocene transition and relationships to global climatic records. *Paleoceanography* **28**, 130–142.

Esser B. K. and Volpe A. M. (2002) At-sea high-resolution chemical mapping: extreme barium depletion in North Pacific surface water. *Marine Chemistry* **79**, 67–79.

Falkowski P. G., Barber R. T. and Smetacek V. (1998) Biogeochemical Controls and Feedbacks on Ocean Primary Production. *Science (1979)* **281**, 200–206.

Fantle M. S. and DePaolo D. J. (2007) Ca isotopes in carbonate sediment and pore fluid from ODP Site 807A: The Ca2+(aq)-calcite equilibrium fractionation factor and calcite recrystallization rates in Pleistocene sediments. *Geochimica et Cosmochimica Acta* **71**, 2524–2546.

Finlay B. 3, Hetherington N. B. and Davison W. (1983) Active biological participation in lacustrine barium chemistry. *Geochimica et Cosmochimica Acta* **47**, 325–1329.

Ganeshram R. S., François R., Commeau J. and Brown-Leger S. L. (2003) An experimental investigation of barite formation in seawater. *Geochimica et Cosmochimica Acta* **67**, 2599–2605.

Geyman B. M., Ptacek J. L., LaVigne M. and Horner T. J. (2019) Barium in deep-sea bamboo corals: Phase associations, barium stable isotopes, & prospects for paleoceanography. *Earth and Planetary Science Letters* **525**.

Gingele F. X., Zabel M., Kasten S., Bonn W. J. and Nürnberg C. C. (1999) Biogenic Barium as a Proxy for Paleoproductivity: Methods and Limitations of Application. In *Use of Proxies in Paleoceanography* Springer Berlin Heidelberg. pp. 345–364.

Gonzalez-Muñoz M. T., Martinez-Ruiz F., Morcillo F., Martin-Ramos J. D. and Paytan A. (2012) Precipitation of barite by marine bacteria: A possible mechanism for marine barite formation. *Geology* **40**, 675–678.

Gooday A. J. and Nott J. A. (1982) Intracellular Barite Crystals in Two Xenophyophores, Aschemonella Ramuliformis and GalatheamminaSp. (Protozoa: Rhizopoda) With

Comments on the Taxonomy of A. Ramuliformis. *Journal of the Marine Biological Association of the United Kingdom* **62**, 595–605.

Gorski C. A. and Fantle M. S. (2017) Stable mineral recrystallization in low temperature aqueous systems: A critical review. *Geochimica et Cosmochimica Acta* **198**, 439–465.

Gou L. F., Jin Z., Galy A., Gong Y. Z., Nan X. Y., Jin C., Wang X. D., Bouchez J., Cai H. M., Chen J. bin, Yu H. M. and Huang F. (2020) Seasonal riverine barium isotopic variation in the middle Yellow River: Sources and fractionation. *Earth and Planetary Science Letters* **531**.

Griffith E., Calhoun M., Thomas E., Averyt K., Erhardt A., Bralower T., Lyle M., Olivarez-Lyle A. and Paytan A. (2010) Export productivity and carbonate accumulation in the Pacific Basin at the transition from a greenhouse to icehouse climate (late Eocene to early Oligocene). *Paleoceanography* **25**.

Griffith E. M. and Paytan A. (2012) Barite in the ocean - occurrence, geochemistry and palaeoceanographic applications. *Sedimentology* **59**, 1817–1835.

Griffith E. M., Paytan A., Wortmann U. G., Eisenhauer A. and Scher H. D. (2018) Combining metal and nonmetal isotopic measurements in barite to identify mode of formation. *Chemical Geology* **500**, 148–158.

Harouaka K., Gorski C. A. and Fantle M. S. (2019) Quantifying Ca exchange in gypsum using a 45Ca tracer: Implications for interpreting Ca isotopic effects in experimental and natural systems. *Geochimica et Cosmochimica Acta* **259**, 371–390.

Hartin C. A., Fine R. A., Sloyan B. M., Talley L. D., Chereskin T. K. and Happell J. (2011) Formation rates of Subantarctic mode water and Antarctic intermediate water within the South Pacific. *Deep-Sea Research Part I: Oceanographic Research Papers* **58**, 524–534.

Heberling F., Metz V., Böttle M., Curti E. and Geckeis H. (2018) Barite recrystallization in the presence of 226Ra and 133Ba. *Geochimica et Cosmochimica Acta* **232**, 124–139.

Hemsing F., Hsieh Y. te, Bridgestock L., Spooner P. T., Robinson L. F., Frank N. and Henderson G. M. (2018) Barium isotopes in cold-water corals. *Earth and Planetary Science Letters* **491**, 183–192.

Ho T. Y., Quigg A., Finkel Z. v., Milligan A. J., Wyman K., Falkowski P. G. and Morel F. M. M. (2003) The elemental composition of some marine phytoplankton. *Journal of Phycology* **39**, 1145–1159.

Hodgskiss M. S. W., Crockford P. W., Peng Y., Wing B. A. and Horner T. J. (2019) A productivity collapse to end Earth's Great Oxidation. *Proc Natl Acad Sci U S A* **116**, 17207–17212.

Horner T. J. and Crockford P. W. (2021) Barium isotopes in barite: drivers, dependencies, and distributions through space and time Geochemical Tracers in Earth System Science. In *Geochemical Tracers in Earth System Science* pp. 1–29.

Horner T. J., Kinsley C. W. and Nielsen S. G. (2015) Barium-isotopic fractionation in seawater mediated by barite cycling and oceanic circulation. *Earth and Planetary Science Letters* **430**, 511–522.

Horner T. J., Lee R. B. Y., Henderson G. M. and Rickaby R. E. M. (2013) Nonspecific uptake and homeostasis drive the oceanic cadmium cycle. *Proc Natl Acad Sci U S A* **110**, 2500–2505.

Horner T. J., Pryer H. v., Nielsen S. G., Crockford P. W., Gauglitz J. M., Wing B. A. and Ricketts R. D. (2017) Pelagic barite precipitation at micromolar ambient sulfate. *Nature Communications* **8**.

Hosoda M., Kelleher K., Murray M., McGinnity P., Hanley O., Wong J. and Currivan L. (2016) Measurement of 222Rn flux, 222Rn emanation, and 226,228Ra concentration from injection well pipe scale. *Radiation Envrionment and Medecine* **5**, 22–28.

Hsieh Y. te, Bridgestock L., Scheuermann P. P., Seyfried W. E. and Henderson G. M. (2021) Barium isotopes in mid-ocean ridge hydrothermal vent fluids: A source of isotopically heavy Ba to the ocean. *Geochimica et Cosmochimica Acta* **292**, 348–363.

Hsieh Y. te and Henderson G. M. (2017) Barium stable isotopes in the global ocean: Tracer of Ba inputs and utilization. *Earth and Planetary Science Letters* **473**, 269–278.

Hu Y., Luo M., Liang Q., Chen L., Feng D., Yang S., Liang J. and Chen D. (2019) Pore fluid compositions and inferred fluid flow patterns at the Haima cold seeps of the South China Sea. *Marine and Petroleum Geology* **103**, 29–40.

Jacquet S. H. M., Dehairs F., Dumont I., Becquevort S., Cavagna A. J. and Cardinal D. (2011) Twilight zone organic carbon remineralization in the Polar Front Zone and Subantarctic Zone south of Tasmania. *Deep-Sea Research Part II: Topical Studies in Oceanography* **58**, 2222–2234.

Jacquet S. H. M., Dehairs F., Elskens M., Savoye N. and Cardinal D. (2007) Barium cycling along WOCE SR3 line in the Southern Ocean. *Marine Chemistry* **106**, 33–45.

Jacquet S. H. M., Dehairs F., Savoye N., Obernosterer I., Christaki U., Monnin C. and Cardinal D. (2008) Mesopelagic organic carbon remineralization in the Kerguelen Plateau region tracked by biogenic particulate Ba. *Deep-Sea Research Part II: Topical Studies in Oceanography* **55**, 868–879.

Kang J., Bracco J. N., Rimstidt J. D., Zhu G. H., Huang F. and Zhu C. (2022) Ba attachment and detachment fluxes to and from barite surfaces in 137Ba-enriched solutions with variable [Ba2+]/[SO42−] ratios near solubility equilibrium. *Geochimica et Cosmochimica Acta* **317**, 180–200.

Kiczka M., Wiederhold J. G., Frommer J., Kraemer S. M., Bourdon B. and Kretzschmar R. (2010) Iron isotope fractionation during proton- and ligand-promoted dissolution of primary phyllosilicates. *Geochimica et Cosmochimica Acta* **74**, 3112–3128.

Klinkenberg M., Brandt F., Breuer U. and Bosbach D. (2014) Uptake of Ra during the recrystallization of barite: A microscopic and time of flight-secondary ion mass spectrometry study. *Environmental Science and Technology* **48**, 6620–6627.

Krumhardt K. M., Long M. C., Lindsay K. and Levy M. N. (2020) Southern Ocean Calcification Controls the Global Distribution of Alkalinity. *Global Biogeochemical Cycles* **34**.

Kusakabe M. and Robinson B. W. (1977) Oxygen and sulfur isotope equilibria in the BaSO4HSO4−H2O system from 110 to 350°C and applications Cite this paper Related papers. *Geochimica et Cosmochimica Acta* **41**, 1033–1040.

Kuss J., Schönberg C.-D. G. and Kremling K. (2001) Rare earth elements in suspended particulate material of North Atlantic surface waters. *Geochimica et Cosmochimica Acta* **65**, 187–199.

de Laeter J. R., Böhlke J. K., de Bievre P., Hidaka H., Peiser H. S., Rosman K. J. R. and Taylor P. D. P. (2003) Atomoic Weights of the Elements (IUPAC Review). *Pure and Applied Chemistry* **75**, 683–800.

Lam P. J., Ohnemus D. C. and Auro M. E. (2015) Size-fractionated major particle composition and concentrations from the US GEOTRACES North Atlantic Zonal Transect. *Deep-Sea Research Part II: Topical Studies in Oceanography* **116**, 303–320.

Legeleux F. and Reyss J.-L. (1996) 228Ra/226Ra activity ratio in oceanic settling particles: implications regarding the use of barium as a proxy for paleoproductivity reconstruction. *Deep-Sea Research* **43**, 1857–1863.

Lestini L., Beaucaire C., Vercouter T. and Descostes M. (2013) Radium Uptake by Recrystallized Gypsum: An Incorporation Study. *Procedia Earth and Planetary Science* **7**, 479–482.

Li W., Kwon K. D., Li S. and Beard B. L. (2017) Potassium isotope fractionation between K-salts and saturated aqueous solutions at room temperature: Laboratory experiments and theoretical calculations. *Geochimica et Cosmochimica Acta* **214**, 1–13.

Ma Z., Gray E., Thomas E., Murphy B., Zachos J. and Paytan A. (2014) Carbon sequestration during the Palaeocene-Eocene Thermal Maximum by an efficient biological pump. *Nature Geoscience* **7**, 382–388.

Martinez-Ruiz F., Jroundi F., Paytan A., Guerra-Tschuschke I., del Mar Abad M. and González-Muñoz M. T. (2018) Barium bioaccumulation by bacterial biofilms and implications for Ba cycling and use of Ba proxies. *Nature Communications*.

Martinez-Ruiz F., Paytan A., Gonzalez-Muñoz M. T., Jroundi F., Abad M. M., Lam P. J., Bishop J. K. B., Horner T. J., Morton P. L. and Kastner M. (2019) Barite formation in the ocean: Origin of amorphous and crystalline precipitates. *Chemical Geology* **511**, 441–451.

Martinez-Ruiz F., Paytan A., Gonzalez-Muñoz M. T., Jroundi F., Abad M. M., Lam P. J., Horner T. J. and Kastner M. (2020) Barite Precipitation on Suspended Organic Matter in the Mesopelagic Zone. *Frontiers in Earth Science* **8**.

Martinez-Ruiz F., Paytan A., González-Muñoz M. T., Jroundi F., del Mar Abad M., Lam P. J., Horner T. J. and Kastner M. (2021) The role of P-rich precursors in barite formation in the ocean. In *American Geophysical Union Fall Meeting* AGU, New Orleans.

Mavromatis V., van Zuilen K., Purgstaller B., Baldermann A., Nägler T. F. and Dietzel M. (2016) Barium isotope fractionation during witherite (BaCO3) dissolution, precipitation and at equilibrium. *Geochimica et Cosmochimica Acta* **190**, 72–84.

Mayer L. M. (1999) Extent of coverage of mineral surfaces by organic matter in marine sediments. *Geochimica et Cosmochimica Acta* **63**, 207–215.

McManus J., Berelson W. M., Klinkhammer G. P., Johnson K. S., Coale K. H., Anderson R. F., Kumar N., Burdige D. J., Hammond D. E., Brumsack H. J., Mccorkle D. C. and Rushdi A.

(1998) Geochemistry of barium in marine sediments: Implications for its use as a paleoproxy. *Geochmica et Cosmochimica Acta* **62**, 3453–3473.

McManus J., Dymond J., Dunbar R. B. and Collier R. W. (2002) Particulate barium fluxes in the Ross Sea. *Marine Geology* **184**, 1–15.

Mishra S. P. and Tiwary D. (1993) Effiecient removal of Ba(II) from aqueous solutions by hyrous manganese oxide. *Journal of Radioanalytical and Nuclear Chemistry, Articles* **170**, 133–141.

Monnin C. and Cividini D. (2006) The saturation state of the world's ocean with respect to (Ba,Sr)SO4 solid solutions. *Geochimica et Cosmochimica Acta* **70**, 3290–3298.

Monnin C., Jeandel C., Cattaldo T., Dehairs F. and Francé F. (1999) The marine barite saturation state of the world's oceans. *Marine Chemistry* **65**, 253–261.

Moore J. C., Wade B. S., Westerhold T., Erhardt A. M., Coxall H. K., Baldauf J. and Wagner M. (2014) Equatorial Pacific productivity changes near the Eocene-Oligocene boundary. *Paleoceanography* **29**, 825–844.

Mozeto A., Roback R., Earman S., Mozeto,' A. A., Fritz P. and Reardon' E. J. (1984) Experimental observations on carbon isotope exchange in carbonate-water systems. *Geochimica et Cosmochimica Acta* **48**, 495–504.

Murray J. W. and Grundmanis V. (1980) Oxygen Consumption in Pelagic Marine Sediments. *Science (1979)* **209**, 1527–1530.

Murray R. W., Leinen • M, Murray D. W., Mix A. C. and Knowlton C. W. (1995) *Terrigenous Fe input and biogenic sedimentation in the glacial and interglacial equatorial Pacific Ocean.*,

Nürnberg C. C., Bohrmann G., Schlüter M. and Frank M. (1997) Barium accumulation in the Atlantic sector of the Southern Ocean: Results from 190,000-year records. *Paleoceanography* **12**, 594–603.

Oelkers E. H., Berninger U. N., Pérez-Fernàndez A., Chmeleff J. and Mavromatis V. (2018) The temporal evolution of magnesium isotope fractionation during hydromagnesite dissolution, precipitation, and at equilibrium. *Geochimica et Cosmochimica Acta* **226**, 36–49.

Oelkers E. H., Pogge von Strandmann P. A. E. and Mavromatis V. (2019) The rapid resetting of the Ca isotopic signatures of calcite at ambient temperature during its congruent dissolution, precipitation, and at equilibrium. *Chemical Geology* **512**, 1–10.

Oelkers E. H. and Schott J. (2001) An experimental study of enstatite dissolution rates as a function of pH, temperature, and aqueous Mg and Si concentration, and the mechanism of pyroxene/pyroxenoid dissolution. *Geochimica et Cosmochimica Acta* **65**, 1219–1231.

Ohnemus D. C. and Lam P. J. (2015) Cycling of lithogenic marine particles in the US GEOTRACES North Atlantic transect. *Deep-Sea Research Part II: Topical Studies in Oceanography* **116**, 283–302.

Ohnemus D. C., Lam P. J. and Twining B. S. (2018) Optical observation of particles and responses to particle composition in the GEOTRACES GP16 section. *Marine Chemistry* **201**, 124–136.

Olivarez Lyle A. and Lyle M. W. (2006) Missing organic carbon in Eocene marine sediments: Is metabolism the biological feedback that maintains end-member climates? *Paleoceanography* **21**.

Orsi A. H., Whitworth Iii T. and Nowlin W. D. (1995) On the meridional extent and fronts of the Antarctic Circumpolar Current. *Deep-Sea Research I* **42**, 64–673.

Palandri J. L. and Kharaka Y. K. (2004) *A compilation of rate parameters of water-mineral interaction kinetics for application to geochemical modeling*., Menlo Park, CA.

Parkhurst D. and Appelo C. (2013) *Description of input and examples for PHREEQC version 3: a computer program for speciation, batch-reaction, one-dimensional transport, and inverse geochemical calculations* ., Denver, CO .

Paytan A. and Griffith E. M. (2007) Marine barite: Recorder of variations in ocean export productivity. *Deep-Sea Research Part II: Topical Studies in Oceanography* **54**, 687–705.

Paytan A. and Kastner M. (1996) Benthic Ba fluxes in the central Equatorial Pacific, implications for the oceanic Ba cycle. *Earth and Planetary Science Letters* **142**, 439–450.

Paytan A., Kastner M., Campbell D. and Thiemens M. H. (1998) Sulfur Isotopic Composition of Cenozoic Seawater Sulfate Related papers. *Science (1979)* **282**, 1459–1462.

Paytan A, Kastner M. and Chavez F. P. (1996) Glacial to Interglacial Fluctuations in Productivity in the Equatorial Pacific as Indicated by Marine Barite. *Science (1979)* **22**, 1355–1357.

Paytan A., Kastner M., Martin E. E., Macdougall J. D. and Herbert T. (1993) Marine barite as a recorder of strontium isotopes. *Nature* **366**, 445–449.

Paytan A., Martinez-Ruiz F., Eagle M., Ivy A. and Wankel S. D. (2004) Using sulfur isotopes to elucidate the origin of barite associated with high organic matter accumulation events in marine sediments. *Special Paper of the Geological Society of America* **379**, 151–160.

Paytan A., Mearon S., Cobb K. and Kastner M. (2002) Origin of marine barite deposits: Sr and S isotope characterization. *Geology* **30**, 747–750.

Paytan A., Moore W. S. and Kastner M. (1996) Sedimentation rate as determined by 226Ra activity in marine barite. *Geochimica et Cosmochimica Acta* **60**, 4313–4319.

Pearce C. R., Saldi G. D., Schott J. and Oelkers E. H. (2012) Isotopic fractionation during congruent dissolution, precipitation and at equilibrium: Evidence from Mg isotopes. *Geochimica et Cosmochimica Acta* **92**, 170–183.

Rea B. A., Dayis J. A. and Waychunas G. A. (1994) Studies of the reactivity of ferrihydrite surface by iron isotopic exchange and Mössbauer spectroscropy. *Clays and Clay Minerals* **42**, 23–34.

Reesman R. H. (1968) The Rb-Sr analyses of some sulfide mineralization. *Earth and Planetary Science Letters* **5**, 23–26.

Rooze J., Peterson L., Peterson R. N. and Meile C. (2020) Porewater flow patterns in surficial cold seep sediments inferred from conservative tracer profiles and early diagenetic modeling. *Chemical Geology* **536**.

Ruiz-Agudo C., Ibáñez-Velasco A. and Ruiz-Agudo E. (2021) The role of amorphous P-bearing precursors on barite formation. *Geochemical Perspectives Letters*, 32–36.

Rushdi A. I., Mcmanus J. and Collier R. W. (2000) Marine barite and celestite saturation in seawater. *Marine Chemistry* **69**, 19–31.

Rutsch H.-J., Mangini A., Bonani G., Dittrich-Hannen B., Kubik ' P. W., Suter M. and Segl M. (1995) 10Be and Ba concentrations in West African sediments trace productivity in the past. *Earth and Planetary Science Letters* **133**, 129–143.

Sabine C. L., Feely R. A., Gruber N., Key R. M., Lee K., Bullister J. L., Wanninkhof R., Wong C. S., Wallace D. W. R., Tilbrook B., Millero F. J., Peng T.-H., Kozyr A., Ono T. and Rios A. F. (2004) The Oceanic Sink for Anthropogenic CO 2. *Science (1979)* **305**, 367–371.

Sarmiento J. L. and Gruber N. (2006) *Ocean Biogeochemical Dynamics*., Princeton University Press.

Sarmiento J. L., Gruber N., Brzezinski M. A. and Dunne J. P. (2004) High-latitude controls of thermoclinenutrients and low latitudebiological productivity. *Nature* **427**, 56–60.

Sauer S., Hong W. L., Yao H., Lepland A., Klug M., Eichinger F., Himmler T., Crémière A., Panieri G., Schubert C. J. and Knies J. (2021) Methane transport and sources in an Arctic deep-water cold seep offshore NW Svalbard (Vestnesa Ridge, 79°N). *Deep-Sea Research Part I: Oceanographic Research Papers* **167**.

Schmitz B. (1987) The Northward wandering of the Indian Current. *Paleoceanography* **2**, 63–77.

Schott J. and Oelkers E. H. (1995) Dissolution and crystallization rates of silicate minerals as a function of chemical affinity. *Pure & Applied Chemistry* **67**, 903–910.

Schott J., Pokrovsky O. S. and Oelkers E. H. (2009) The link between mineral dissolution/precipitation kinetics and solution chemistry. *Reviews in Mineralogy and Geochemistry* **70**, 207–258.

Sexton P. F. and Norris R. D. (2011) High latitude regulation of low latitude thermocline ventilation and planktic foraminifer populations across glacial-interglacial cycles. *Earth and Planetary Science Letters* **311**, 69–81.

Siebert Christopher, Ègler Thomas F Na, Kramers Jan D, Siebert C, Ègler T F Na and Kramers J D (2001) Determination of molybdenum isotope fractionation by double-spike multicollector inductively coupled plasma mass spectrometry. *Geochemistry Geophysics Geosystems* **2**.

Sigman D. M., Hain M. P. and Haug G. H. (2010) The polar ocean and glacial cycles in atmospheric CO2 concentration. *Nature* **466**, 47–55.

Smith W. and Chanley M. (1975) *Culture of Marine Invertebrate Animals*., Springer US.

Snelgrove S. H. and Forster C. B. (1996) Impact of seafloor sediment permability and thickness on off-axis hydrothermal circulation: Juan de Fuca Ridge eastern flank. *Journal of Geophysical Research B: Solid Earth* **101**, 2915–2925.

Steefel C. I., Druhan J. L. and Maher K. (2014) Modeling Coupled Chemical and Isotopic Equilibration Rates. *Procedia Earth and Planetary Science* **10**, 208–217.

Sternberg E., Jeandel C., Robin E. and Souhaut M. (2008) Seasonal cycle of suspended barite in the mediterranean sea. *Geochimica et Cosmochimica Acta* **72**, 4020–4034.

Sternberg E., Tang D., Ho T. Y., Jeandel C. and Morel F. M. M. (2005) Barium uptake and adsorption in diatoms. *Geochimica et Cosmochimica Acta* **69**, 2745–2752.

Stroobants N., Dehairs F., Goeyens L., Vanderheijden N. and van Grieken R. (1991) Barite formation in the Southern Ocean water column. *Marine Chemistry* **35**, 411–421.

Sunda W. G. and Huntsman S. A. (1994) Photoreduction of manganese oxides in seawater. *Marine Chemistry* **46**, 133–152.

Talley L. D. (2013) Closure of the global overturning circulation through the Indian, Pacific, and southern oceans. *Oceanography* **26**, 80–97.

Tani Y., Kakinuma S., Chang J., Tanaka K. and Miyata N. (2021) Preferential elimination of Ba2+ through irreversible biogenic manganese oxide sequestration. *Minerals* **11**, 1–13.

Tian L. L., Zeng Z., Nan X. Y., Yu H. M. and Huang F. (2019) Determining Ba isotopes of barite using the Na2CO3 exchange reaction and double-spike method by MC-ICP-MS. *Journal of Analytical Atomic Spectrometry* **34**, 1459–1467.

Torapava N., Ramebäck H., Curti E., Lagerkvist P. and Ekberg C. (2014) Recrystallization of 223Ra with barium sulfate. *Journal of Radioanalytical and Nuclear Chemistry* **301**, 545–553.

Torres Marta E, Bohrmann G. and Suess E. (1996) Authigenic barites and fluxes of barium associated with fluid seeps in the Peru subduction zone. *Earth and Planetary Science Letters* **144**, 469–481.

Torres M E, Brumsack H., Bohrmann G. and Emeis K. (1996) Barite fronts in continental margin sediments: A new look at barium remobilization in the zone of sulfate reduction and formation of heavy barites in diagenetic fronts. *Chemical Geology* **127**, 125–139.

Turchyn A. v. and Schrag D. P. (2006) Cenozoic evolution of the sulfur cycle: Insight from oxygen isotopes in marine sulfate. *Earth and Planetary Science Letters* **241**, 763–779.

Turchyn A. v and Schrag D. P. (2004) Turchyn & Schragg (2004). *Science (1979)* **303**, 2004–2007.

Vinograd V. L., Brandt F., Rozov K., Klinkenberg M., Refson K., Winkler B. and Bosbach D. (2013) Solid-aqueous equilibrium in the BaSO4-RaSO4-H2O system: First-principles calculations and a thermodynamic assessment. *Geochimica et Cosmochimica Acta* **122**, 398–417.

Vital M., Daval D., Morvan G., Martinez D. E. and Heap M. J. (2020) Barite Growth Rates as a Function of Crystallographic Orientation, Temperature, and Solution Saturation State. *Crystal Growth and Design* **20**, 3663–3672.

Weber J. (2017) Fundamental Insights into the Radium Uptake into Barite by Atom Probe Tomography and Electron Microscopy. .

Wetzel F., de Souza G. F. and Reynolds B. C. (2014) What controls silicon isotope fractionation during dissolution of diatom opal? *Geochimica et Cosmochimica Acta* **131**, 128–137.

Wiederhold J. G., Kraemer S. M., Teutsch N., Borer P. M., Halliday A. N. and Kretzschmar R. (2006) Iron isotope fractionation during proton-promoted, ligand-controlled, and reductive dissolution of goethite. *Environmental Science and Technology* **40**, 3787–3793.

Yao W., Griffith E. and Paytan A. (2021) *Pelagic Barite: Pelagic Barite: Tracer of Ocean Productivity and a Recorder of Isotopic Compositions of Seawater S, O, Sr, Ca and Ba*., Cambridge University Press.

Yentsch C. S. and Menzel D. W. (1963) A method for the determination of phytoplankton chlorophyll and phaeophytin by fluorescence*. *Deep-Sea Reseach* **10**, 221–231.

Yokoo H., Oki T., Uehara M., Winarni I. D., Yamaji K., Fukuyama K., Ohara Y., Ohnuki T., Hochella Jr M. F. and Utsunomiya S. (2021) Geochemistry of barium ions associated with biogenic manganese oxide nanoparticles generated by a fungus strain: Implications for radium sequestration in uranium mill tailings. *Gondwana Research*.

Young C. L. and Ingall E. D. (2010) Marine dissolved organic phosphorus composition: Insights from samples recovered using combined electrodialysis/reverse osmosis. *Aquatic Geochemistry* **16**, 563–574.

Zhen-Wu B. Y., Dideriksen K., Olsson J., Raahauge P. J., Stipp S. L. S. and Oelkers E. H. (2016) Experimental determination of barite dissolution and precipitation rates as a function of temperature and aqueous fluid composition. *Geochimica et Cosmochimica Acta* **194**, 193–210.